ADVANCES IN ATOMIC, MOLECULAR, AND OPTICAL PHYSICS, VOL. 49

APPLICATIONS OF OPTICAL CAVITIES IN MODERN ATOMIC, MOLECULAR, AND OPTICAL PHYSICS

JUN YE[1,*] *and THERESA W. LYNN*[2]

[1]*JILA, National Institute of Standards and Technology and University of Colorado, Boulder, Colorado 80309-0440*

[2]*Norman Bridge Laboratory of Physics, Room 12-33, California Institute of Technology, Pasadena, California 91125*

*E-mail: ye@jila.colorado.edu

Copyright © 2003 Elsevier Science (USA)
All rights reserved
ISBN 0-12-0038498/ISSN 1049-250X/03 $35.00

[21.7.2003–8:32pm] [1–84] [Page No. 1] FIRST PROOFS {Books}4101-Bederson/Pageproofs/3d/4101-Bederson-001.3d (Bederson) Paper: 4101-Bederson-001 Keyword

I. Introduction

For many contemporary physics experiments, the use of an optical cavity has become a powerful tool for enhancement in detection sensitivities, nonlinear interactions, and quantum dynamics. Indeed, an optical cavity allows one to extend the interaction length between matter and field, to build up the optical power, to impose a well-defined mode structure on the electromagnetic field, to enable extreme nonlinear optics, and to study manifestly quantum mechanical behavior associated with the modified

vacuum structure and/or the large field associated with a single photon confined to a small volume. Experimental activities that have benefited from the use of optical cavities appear in such diverse areas as ultra-sensitive detection for classical laser spectroscopy, nonlinear optical devices, optical frequency metrology and precision measurement, and cavity quantum electrodynamics (cavity QED). Of course the most important application of optical cavities is in laser physics itself. However, in this article we will concentrate on the various applications of external optical cavities (independent from lasers) that take advantage of the common physical properties associated with resonator physics.

One of the important themes in laser spectroscopy is to utilize an extended interaction length between matter and field inside a high finesse cavity for an increased detection sensitivity. Two key ingredients are needed to achieve the highest sensitivity possible in detection of atomic and molecular absorptions: enhancement of the absorption signal and elimination of technical noise. While the absorption signal is enhanced by an optical cavity, it is important also to take measures to avoid technical noise: the sharp resonances of the cavity can introduce additional noise through frequency-to-amplitude noise conversion. Cavity vibration and drifts can also contribute noise beyond the fundamental, quantum-noise limit. In this article (Sections IV and V), we will discuss the application of various modulation techniques combined with suitable experimental configurations that let one benefit from the signal enhancement aspect of a cavity, at the same time suppressing the technical noise in the detection process. Such achievement has enabled studies of molecular vibration dynamics of weak transitions.

Another important theme is the application of optical frequency metrology for precision measurements. Section VI addresses the role of optical cavities in this context. Certainly the use of an optical cavity for laser frequency stabilization is critical for the development of super-stable optical local oscillators. The extreme quality factor (10^{15}) associated with some "forbidden" optical transitions in cold and trapped samples of atoms and ions demands a similar or even higher quality factor on the optical probe source to take full advantage of the system coherence. Although the advent of femtosecond-laser-based optical frequency combs has to a certain degree reduced the utility of cavity-based frequency reference systems, stable optical cavities continue to provide important services in laser laboratories; either the cavity modes themselves provide optical frequency markers or a cavity helps enhance optical to microwave frequency coupling via an intracavity modulator. And one the most important applications of optical cavities is still for laser frequency stabilization, with the scope now extended to cover ultrafast lasers as well. In fact, cavity-based ultra-sensitive detection

[21.7.2003–8:32pm] [1–84] [Page No. 3] FIRST PROOFS {Books}4101-Bederson/Pageproofs/3d/4101-Bederson-001.3d (Bederson) Paper: 4101-Bederson-001 Keyword

of atomic/molecular absorptions represents an important approach to produce accurate and precise frequency references throughout the visible and near-infrared wavelength regions. We also note that some of the most demanding work in precision measurement is now associated with cavity-enhanced Michelson interferemetry to search for gravitational waves.

A third theme that will be covered in this article (Section VII) is the exploration of quantum dynamics associated with the enhanced interaction between atoms and cavity field; where the structure of the cavity enables a large field amplitude associated with single intracavity photons, the system dynamics can become manifestly quantum and nonlinear. A high cavity finesse suppresses the dissipation rate associated with photon decay while a well-defined spatial mode of the cavity output field (associated with cavity decay) permits recovery of information about the intracavity dynamics with high quantum efficiency. Although cavities in the optical domain have not significantly influenced the atomic radiative properties in a direct manner, the enhanced coherent interactions between them present an ideal platform to study open quantum systems.

Before addressing these topics in detail, we begin with some broad comments and historical context in the remainder of this introduction. Section II is devoted to description and characterization of the optical cavities themselves, while Section III gives some simple physical arguments for the cavity enhancement effect that is crucial for applications ranging from classical spectroscopy to cavity QED.

A. Signal Enhancement and Optical Field Buildup Inside Cavity

Improving sensitivity for spectroscopy on an atomic or molecular sample by placing it inside an optical resonator is a well-known technique and is most commonly explained in terms of the multipass effect. In fact, it was realized in the early days of laser development that a laser cavity was useful for absorption enhancement [1], owing to the multipass effect and the delicate balance between the laser gain and intracavity absorption [2,3]. However, in most recent implementations, it is often preferable to separate the absorber from the laser, in order to extend the experimental flexibility and to characterize better working parameters. Kastler first suggested that a Fabry-Perot cavity be employed for the sensitivity of its transmission to small variations in absorption within the cavity [4]. The external cavity approach has since been applied to record both linear and high-resolution nonlinear molecular spectra [5–7]. In particular, enhancement cavities in the form cavity ring down spectroscopy [8,9] have been extensively applied in the field physical chemistry to study molecular dynamic and reaction kinetics.

While we defer a detailed discussion of cavity enhancement effects to Section III, here we make a quick note of the advantages associated with an optical resonator. The well-known multipass effect leads to an enhancement of the effective absorption length by a factor of $2F/\pi$, where F is the cavity finesse. Additionally, the intracavity optical power is built up relative to the input power via constructive interference, which allows for the study of nonlinear interactions even with low-power laser sources. An often taken-for-granted benefit in practice is that although the intracavity interaction is powered by a high field amplitude, the cavity reduces the output power to a reasonable level acceptable for subsequent photo-detectors. Alternatively, high intracavity power can be extracted using high-speed optical switching devices; this forms the basis of a cavity-based optical amplifier to be discussed in Section VI.D. Additionally, the geometrical self-cleaning and mode matching of the optical waves inside a cavity is important both for eliminating pointing-direction related noise and for obtaining narrow, unshifted resonance lines [10]. Finally, a stable cavity can be used to stabilize a laser's frequency by locking the laser to a cavity resonance, thereby reducing the detection noise in any measurement involving the laser.

B. Issues Related to Technical and Fundamental Noise

Direct absorption measurements often suffer from intensity noise on the laser. Noise amplitudes typically rises toward the low-frequency region of the intensity spectrum where many important signals reside; this problem has motivated development of modulation schemes, such as frequency-modulation spectroscopy, to encode and recover signals in frequency intervals with minimal technical noise. The use of an optical cavity, while effective in enhancing a signal, can also introduce some extra technical noise. For example, when the relative frequency fluctuation between the laser and the cavity resonance is of the same order as the cavity linewidth, frequency noise will be converted to amplitude noise in the detected signal if a naïve, direct absorption approach is adopted. Because this noise conversion is inversely proportional to the cavity linewidth, the same enhancement factor that has improved the signal size can play an equal—but deleterious—role. Thus, while it is important to reduce noise amplitudes in the first place, it is usually equally imperative to employ some clever signal recovery techniques that minimize the influence of noise on the detection result. For any absorption spectroscopy, the fundamental detection limit is reached when the minimum signal amplitude equals to the noise level associated with the discrete nature of a photon flux, which has a Poisson distribution for an ordinary laser output without technical noise. Such performance can be

achieved when the technical noise is minimized by a differential measurement. For a true differential measurement, quick comparisons of on-resonance and off-resonance information are required; that is, some sort of modulation technique should be employed. When combined with an effective modulation technique, the resonant cavity scheme approaches its full potential for signal enhancement without added noise.

When cavity finesse is sufficiently high, then in order to limit the intracavity power to some useful level below system saturation, the power level associated with the cavity input and transmission will usually be maintained low. Detection of these small transmission signals with high signal-to-noise (S/N) is therefore a technical challenge. Although photon counting has been an effective approach to detect low light levels and construct useful photon statistics, it is not suitable for coherent detections if the field phase is the desired quantity to measure. As discussed in Ref. [11], a balanced heterodyne detection would allow a full construction of the quantum susceptibility of intracavity absorbers. Optical heterodyne detection with the aid of a large optical local oscillator field is also an effective and necessary approach to overcome serious electronic noise limitations.

C. Change of Boundary Conditions—Quantum Effect

Optical elements present boundary conditions that alter the free-space quantization structure of the electromagnetic field. This modified electromagnetic mode structure in turn affects the interactions of an atomic dipole with light, including decay into the now-altered vacuum. Diverse observations have demonstrated changes in atomic radiative processes caused by the presence of a boundary; for example, boundary-induced atomic level shifts form the basis of the Casimir effect and numerous other phenomena. For a review of these effects and their development into the field of cavity QED, see for example Ref. [12].

The boundary conditions imposed by an optical cavity create a set of electromagnetic field modes confined between the cavity mirrors. These resonant cavity modes are well-defined in frequency and in spatial structure. The modes of an optical cavity typically subtend a small fraction of 4π in solid angle, and thus do not significantly suppress free-space atomic spontaneous emission. However, the presence of the cavity introduces a new rate, the rate of coherent exchange of excitation between atom and cavity field. Through this coherent coupling the atom and cavity decay linewidths do in fact alter one another, at first perturbatively and then strongly as the coherent coupling becomes large relative to both decays. Finally, when the physical size of a cavity is reduced until the cavity mode volume is near

the atomic "radiative" volume, a whole new set of quantum dynamics associated with the full quantum susceptibility can be explored within the setting of cavity quantum electrodynamics [11,13].

D. Applications of Sensitive Detection, Field Enhancement, and Cavity QED

Sensitive, cavity-enhanced detection schemes have found many different applications, including the characterization of dielectric stacks [14]; measurement of ultraslow reflector velocities [15]; atmospheric sensing [16,17]; detection of trace gaseous species [18]; absolute determination of absorption band strengths and species concentration [19]; analysis of combustion and plasma dynamics [20,21]; study of chemical kinetics and molecular dynamics [22,23]; tests of fundamental physical postulates such as quantum spin statistics [24–26], gravitational wave detections [27,28], thermal noise detection and control [29], and magnetically induced vacuum birefringence [30,31]; improvements in laser stabilization and optical frequency metrology [32–34]; novel schemes for laser cooling [35]; and research into quantum dynamics and quantum information [36–38], nonlinear optics [39], and quantum measurement limit [40–42]. The extension of these methods to study surfaces and condensed matter [43] and their potential applications as medical instruments only make the field more exciting [44,45].

II. Mode Structure and Relevant Characteristics of Fabry–Perot Cavities

In this section we briefly lay out the properties of an optical cavity that will be relevant to all the scientific applications discussed in this article. Since Fabry-Perot cavities are by far the most widely used optical cavities to date and in the immediate future, we concentrate on them specifically in our treatment. More exotic cavity geometries and fabrication methods are touched upon only very briefly, in Section VII.G. While this section lays the groundwork for further discussions, presentations in some later sections revisit the issues of precise measurement of cavity mode spacings, mirror coating properties, and subtleties of cavity mode structure.

A. Mode Structure and Basic Definitions

Figure 1 shows a Fabry-Perot optical resonator created by aligning two highly reflective mirrors at separation d measured along the cavity axis.

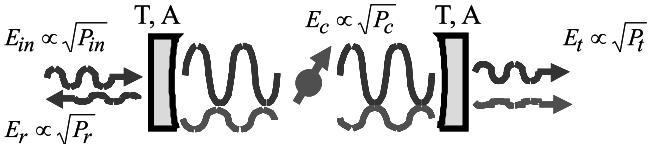

$$(\alpha d)_{enhanced} = \left(\frac{g_0^2}{\gamma}\cdot\tau_{cavity}\right) \approx (\alpha d)\cdot\frac{2F}{\pi} \qquad F: \text{cavity finesse}$$

FIG. 1. Notation for the fields in and out of an optical cavity. The standing-wave field built-up inside the cavity is shown, along with the radiation field from the prepared atomic dipole.

Modes of the cavity possess a standing-wave structure along the axis, so the cavity supports a set of longitudinal modes separated in frequency by a *free spectral range* (FSR) of $c/2d$ where c is the speed of light. (Mirror coatings cause the FSR to deviate very slightly from this simple formula, as will be discussed in Section VI.) At each longitudinal mode the cavity supports a complete set of transverse modes of different transverse spatial profiles. The TEM_{00} mode has a cylindrically symmetric Gaussian profile, characterized by a beam waist w_0.

If the two mirrors are assumed to be identical, the cavity is characterized by the per-mirror power transmission T and loss A. The total empty cavity loss is $L_{\text{cav}} = 2(T + A)$. The cavity finesse ($F$) is given by

$$F = \frac{2\pi}{L_{\text{cav}}} = \frac{\pi}{T + A}. \tag{1}$$

The finesse can also be expressed as the ratio of free spectral range to cavity linewidth. It is closely related to another commonly used quantity, the resonator quality factor Q, which is the ratio of the resonant optical frequency to the cavity decay linewidth. The use of finesse is attractive as it depends only on the mirror properties and not on the cavity dimension. When the cavity length changes, both the *FSR* and linewidth of the cavity vary as the inverse of the cavity length, and hence the finesse remains a constant. Q and F are related by the ratio of the optical frequency to the *FSR*; the latter lies normally in the RF/microwave frequency domain.

B. Realization of High-Finesse Cavities

High-finesse cavities are typically constructed from superpolished substrates coated with a "stack" (40–50 or so alternating layers) of dielectric materials

so that coating layers have alternating high and low index of refraction. The layer thickness sets the center wavelength of the coating. These coating techniques are capable of producing mirror transmission T at or below 10^{-6} (1 ppm). However, current technology has yet to push mirror loss A below one to a few ppm. Thus cavity finesses in the range of 10^5 to 10^6 constitute the current state of the art for high-reflectivity, low-loss mirrors and coatings. Mirror absorption/scatter losses set a limit on F and are furthermore a hindrance to signal extraction when nonlinear interactions are present. For example, they are a critical limiting factor in the loss rate for present cavity QED systems—for the very short cavities used in these experiments, loss rates associated with A are usually similar in size to the atomic spontaneous emission rates. To build robust quantum computing/communications devices from cavity QED components, it is necessary to improve the ratio of mirror transmission (useful information) to mirror losses (loss of coherence).

Different cavity lengths are desirable for each application of optical cavity technology. The smallest cavity mode volumes are demanded by cavity QED applications, which currently use cavities with transverse mode waists as small as $w_0 \sim 10$ μm and cavity lengths $d \sim 10\,\mu$m or slightly shorter. At these lengths it is important to consider that the standing-wave light field inside a cavity penetrates into the mirror coatings, giving a larger mode-volume than would be otherwise expected from the physical distance between the mirror surfaces. When the micro-cavities are pushed to shorter lengths in the quest for greater interaction strengths, the leakage field into the mirror coatings will have a non-negligible effect on the cavity mode structure.

III. Cavity Enhancement: A Simple Physics Picture

In this section we will discuss the basic physics associated with the cavity enhancement effect. We will derive some useful equations from different perspectives and show that, as with many other subjects, the cavity-enhancement principle manifests itself in different and yet eventually equivalent forms. It is useful to explore these different aspects as each highlights distinct practical consequences and can lead to effective experimental techniques.

A. Enhanced Optical Radiation and Interaction Length

We start our discussion of cavity-enhancement by directly looking into the cavity properties. The basic understanding can be developed by placing

the absorbing atoms or molecules in an optical cavity and then comparing the absorption level to the intrinsic loss of the cavity. Thus low-loss mirrors (and consequently high-finesse cavities) help to enhance the signal contrast. Beginning with the empty-cavity case, we denote the optical input power as P_{in}, the cavity-reflected power as P_{r}, and the cavity-transmitted power as P_{t} (see Fig. 1). The resonant cavity reflection efficiency, transmission efficiency, and intracavity build-up power, P_{c}, can be expressed, respectively, as

$$\begin{aligned} \frac{P_{\text{r}}}{P_{\text{in}}} &= \left(\frac{A}{T+A}\right)^2, \\ \frac{P_{\text{t}}}{P_{\text{in}}} &= \left(\frac{T}{T+A}\right)^2, \quad \text{and} \\ \frac{P_{\text{c}}}{P_{\text{in}}} &= T\left(\frac{1}{T+A}\right)^2. \end{aligned} \tag{2}$$

These equations can be easily derived following any modern optics textbook [46].

Consider a cavity of roundtrip length $2d$, filled with a weakly absorbing gas sample with an absorption coefficient of α per unit length. (By weakly absorbing we mean the cavity round trip fractional power loss can be written as $1-\exp(-2\alpha d) \approx 2\alpha d$. We will also use the assumption that $\alpha d \ll T, A$). In a direct absorption measurement with a sample cell of length d, the output power is; $P_{\text{out}} = P_{\text{in}} \cdot \text{e}^{-\alpha d} \sim P_{\text{in}}\ (1-\alpha d)$. Therefore, the absorption signal is $(P_{\text{in}} \cdot \alpha d)$, with contrast $\delta P_{\text{out}}/P_{\text{out}} = -\alpha d$. When the sample is placed inside a cavity, the transmitted power is modified according to Eq. (2),

$$\frac{P_{\text{t}}}{P_{\text{in}}} = \left(\frac{T}{T+A+\alpha d}\right)^2 \approx \left(\frac{T}{T+A}\right)^2 \left(1-2\frac{\alpha d}{T+A}\right). \tag{3}$$

The detected signal contrast in the cavity transmission is therefore enhanced to

$$\frac{\delta P_{\text{t}}}{P_{\text{t}}} = -2\frac{\alpha d}{T+A} = -\frac{2F}{\pi} \cdot (\alpha d). \tag{4}$$

In practice, the anticipated sample absorption may actually be of the same order or larger than the mirror transmission coefficients. In this case input and output mirror parameters should be individually selected to maximize the resonant cavity transmission under the ''impedance-matching''

boundary conditions in the presence of intracavity gas absorption. It is also worth noting that, although the cavity finesse is determined by the sum of the mirror transmission T and loss A and neither quantity appears explicitly in Eq. (4), it is optimal for T to be dominant over A, because this increases the absolute size of the absorption signal [cf. Eq. (3)]. The ratio of T to A is even more important for studying nonlinear dynamics; for cavity QED experiments, for example, T represents an accessible communication channel for information flow from the cavity to the outside world while A represents irreversible loss of coherence.

B. Enhanced Radiation (Absorption) of Atomic/Molecular Dipole Moments Inside Cavity

Perhaps cavity enhancement can be most simply understood from the cartoon picture shown in Fig. 2. Suppose a single atom is present within the mode volume of a resonant light field propagating through a length d. The total absorption coefficient (αd) can be interpreted as arising from an atomic transition rate R multiplied by the interaction time, d/c. From this intuitive picture, we can immediately understand that if a cavity is placed around the atom with the intracavity photon lifetime resonantly increased to $\tau_{\text{cavity}} = (2F/\pi) \cdot d/c$, the absorption coefficient becomes $(\alpha d)_{\text{enhanced}} = R \cdot \tau_{\text{cavity}} = (2F/\pi)(\alpha d)$.

To explore other factors determining the strength of interaction, we take another look at the microscopic origins of the absorption coefficient (αd) itself. Denoting the atomic dipole moment μ and the transition wavelength λ angular frequency $\omega = \Pi c\lambda$, with c being the speed of light), we have the atomic decay rate $\gamma \propto \mu^2/\lambda^3$ via the Fermi golden rule. For a cavity mode of cross-sectional area a, the coupling between the atom and the electric field of a single photon is $g_0 \propto \mu \cdot \sqrt{\omega/(a \cdot d)}$. Here the factor within the square root arises from the energy density for a single photon within the designated

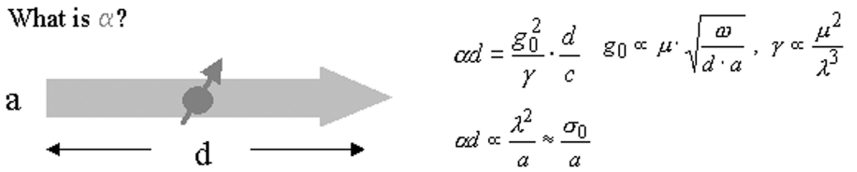

FIG. 2. An intuitive picture of atomic absorption: μ is the atomic dipole moment, λ the transition wavelength, Γ the spontaneous decay rate, g_0 the coherent coupling between the atomic dipole and the light field quantized within the volume of ($a \cdot d$), and σ_0 represents the resonant atomic absorption cross-section.

mode volume. The transition rate R above is then given by $g_0^2(1/\gamma)$. Therefore $\alpha d \propto \left(g_0^2/\gamma\right) \cdot d/c \approx \lambda^2/a \approx \sigma_0/a$, with σ being the resonant absorption cross-section of the atom. Cavity enhancement of the interaction lifetime adds a factor of $2F/\pi$ as above, so the absorption scales as the cavity finesse over the cross-sectional area of the mode.

C. Constructive Interference of Atomic/Molecular Radiation

It is clear from Eq. (2) that the intracavity circulating power can be much larger than the input power. This power buildup is essential to have an appreciable level of saturation for nonlinear spectroscopy involving very weak transitions. The strong light field phase-coherently drives the atomic or molecular dipole moments. The radiation from these prepared dipole moments is the signal to be detected. However, the strong background of the unabsorbed incoming light sets the detection noise level, the shot-noise level in the ideal case (cf. Section IV). With the build-up cavity approach, this potentially large noise contribution from the intracavity field is reduced after the sample has been prepared and before the final detection. When the cavity is tuned onto a molecular line, the major part of the molecular signal will leak out of the cavity to reach a detector, while a similar, or smaller, portion of the input power will be transmitted by the cavity and reach the same detector to set the shot-noise limit. The large intracavity buildup power, however, will remain trapped inside, where it prepares the phase-coherent molecular dipole moment of an enhanced magnitude. This result, although explained here from yet another perspective, is the same cavity enhancement effect discussed in the previous paragraphs.

To mathematically clarify the preceding discussion, we note that the intracavity field E_c is related to the input field E_{in} by $E_c = E_{in} \cdot \sqrt{T}/(T + A)$ (cf. Fig. 1). The radiation field of the prepared dipole moment can be written as $E_{atom} = -E_c \cdot (\alpha d/2)$, where the minus sign accounts for the negative interference between the sample radiation and the original field that leads to absorption. The integrated intracavity (single-pass) absorption signal is (αd) and the factor of $1/2$ reflects the fact that we are now dealing with the field amplitude. When the cavity is tuned to the atomic resonance, this atomic signal will be resonantly enhanced by constructive interference, by a factor of $2/(T + A)$. Here the factor of 2 accounts for the bi-directional effect in the cavity. Finally the field leaking out of the cavity is attenuated by $\sqrt{T}$ before reaching the photodetector. The final field can thus be expressed as

$$E_{\text{atom,output}} = -\sqrt{T} \cdot E_c \left(\frac{\alpha d}{2}\right) \cdot \left(\frac{2}{T + A}\right) = -\frac{T}{T + A} E_{in} \cdot \left(\frac{\alpha d}{2}\right) \cdot \left(\frac{2F}{\pi}\right) \quad (5)$$

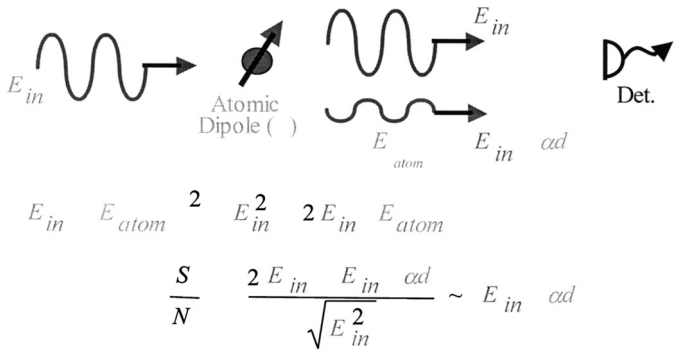

FIG. 3. Principle of optical (homodyne) heterodyne detection of an absorption signal, showing the destructive interference between the incident and the radiating fields. Derivation of a simple shot noise limited S/N ratio is shown.

When this quantity is small compared to the transmitted local oscillator field, $E_{\text{in}} \cdot T/(T + A)$, the change in output power due to the atom is proportional to their cross-term, and thus the signal enhancement factor is again $(2F/\pi)$. This will be explained in a more detailed manner in Section IV.B, in the context of discussions about heterodyne detection (Fig. 3). In Section IV.E we will also show how the same cavity enhancement factor manifests itself in the detected phase shift of an output field from the cavity.

From a practical point of view, using a cavity is also attractive when the laser source has a relatively large amplitude noise. Indeed, when a buildup cavity is used, the subsequent photodetector does not have to receive a large intensity. One takes advantage of a large intracavity field to enhance the signal of interest, allowing for a high S/N for detection outside the cavity as the transmitted powers is low enough that shot noise could dominate over technical noise. This effect is similar to the result of polarization spectroscopy [47] or interference filtering.

D. Field Quantization—Influence of the Cavity Physical Size and Strong Coupling Regime in Cavity QED

Although our discussion so far has focused mainly on the semiclassical aspect of the light-matter interaction, it is nonetheless interesting to make a quick note on the connection between this classical picture of cavity-enhanced spectroscopy and optical cavity-based quantum electrodynamics (QED). When the cavity volume ($\sim \pi w_0^2 d/4$) is comparable to the critical radiation volume of a single atom, namely $V_{\text{critical}} = \lambda^2 \cdot c/\gamma$, the atom-cavity interaction needs to be treated in a fully quantum picture.

Crucial to the realization of manifestly quantum effects in cavity QED is *strong coupling*, a condition in which the coherent coupling between atom and cavity field dominates dissipative rates in the system. For a two-level atom optimally coupled to a cavity mode, the dipole-field coupling is given by the Jaynes-Cummings interaction Hamiltonian [48]

$$\hat{H}_{\text{int}} = \hbar g_0(\hat{\sigma}^+\hat{a} + \hat{\sigma}\hat{a}^+), \tag{6}$$

where $(\hat{\sigma}^+, \hat{\sigma})$ are atomic dipole raising and lowering operators, $(\hat{a}, \hat{a}^+)$ are field annihilations and creation operators for the cavity mode, and g_0 is one half of the single-photon Rabi frequency. This rate describes the exchange of excitation between the atomic dipole $\vec{\mu}$ and the electric field $\vec{E}$ built up by a single photon of frequency ω residing in the mode volume V_m of the optical cavity:

$$g_0 = \vec{\mu} \cdot \vec{E} = \mu\sqrt{\frac{\hbar\omega}{2\varepsilon_0 V_m}}. \tag{7}$$

Thus g_0 is a rate of coherent evolution that must be compared with the dissipative rates for the system. These, in turn, are the atomic spontaneous emission rate $\gamma_\perp$ and the cavity field decay rate κ. While the regime of $(\kappa, \gamma_\perp) \gg g_0$ is described by the classical treatments developed above, we will see in Section VII that a quantum theory is necessary to account for physics at $g_0 \gg (\kappa, \gamma_\perp)$, in the strong coupling regime [49–51].

Though atom-cavity behavior in the strong coupling limit must be calculated in an inherently quantum treatment, the onset of this regime can be estimated from quantities well known from classical spectroscopy. In the optical bistability and cavity QED literature [52,53], there is an atomic co-operativity parameter defined as $Ng_0^2/2\kappa\gamma$, where N is the number of atoms. This quantity signifies the level of modification of the empty cavity properties by the presence of atoms. Calculation reveals that the co-operativity parameter is nothing but the now familiar $(2F/\pi)\alpha d$, the enhanced intracavity absorption signal. This understanding leads to a natural definition of the critical atom number: $N_0 = 2\kappa\gamma/g_0^2$, which signifies the level of influence by a single atom on the cavity dynamics. Similarly, the critical photon number can be defined as $m_0 = \gamma^2/2g_0^2$, which is basically the number of intracavity photons required to saturate an atom, and is directly related to the aforementioned ratio of cavity mode volume to atomic radiative volume. More extensive discussions in Section VII will further

clarify the physical meanings of these quantities and their significance related to the latest generation of optical cavity QED experiments.

IV. Weak Absorption Measured by Field-Phase (Frequency-Domain)

In parallel with signal enhancement, the issues of detection noise and how to reach the fundamental noise limit are equally critical to the implementation of sensitive spectroscopy. In this section, we will concentrate our discussions in the frequency domain on the relevant issues related to signal extraction and noise suppression.

The ultimate detection sensitivity is achieved when we are able to observe each absorption event individually, and when the noise is limited by the uncertainty of an event occurrence. This is referred to as the shot-noise limit. The shot noise is associated with the discrete nature of the interaction between matter and the photon stream. The shot noise is fundamental in that it reflects the quantum nature of light from ordinary thermal sources and lasers far above threshold, sources that carry Poissonian statistics. Radiation fields can also be "squeezed" to have sub-Poissonian levels of fluctuation, providing an anomalously low fluctuation level for the photocurrent (i.e., sub-shot noise).

The signal exiting the cavity can also be measured using phase sensitive detection methods, i.e., in frequency-domain applications. The phase of the light, along with the cavity resonance structure, is perturbed by the molecular radiation, which leads to additional phase shifts. The objective of this section is to discuss phase-sensitive optical-heterodyne spectroscopy, using an enhancement-cavity, as a tool for signal acquisition. The advantage of this approach lies in the characteristic property of frequency modulation (FM) spectroscopy: the simultaneous and continuous observation and subtraction of the signal and background optical phases.

A. Fundamental Detection Limits in Classical Spectroscopy

As noted in Section III, the physical origin of the absorption process can be understood as destructive interference between the incident radiation and the electric field generated by the coherently driven dipole moments of the sample. Therefore, direct absorption can be viewed as a homodyne detection between two interfering fields that have the same frequency. Maximum sensitivity occurs when the probe field has no amplitude noise beyond its intrinsic quantum fluctuations. Given a detection bandwidth of B and the

average photocurrent i_{dc}, the associated shot-noise current is given by $i_n = \sqrt{2ei_{dc}B}$, where e is the electron charge. Taking the photodetector responsivity as η (dimensions of electrical current per unit power incident on the detector) and P_0 as the incident radiation power, then $i_{dc} = \eta P_0$ and the absorption signal $i_{sig} = (\alpha d)\eta P_0$. The shot noise will set the fundamental sensitivity limit for straight absorption spectroscopy. When the S/N ratio is one, i.e., when the molecular absorption is equivalent to the shot noise in the measurement bandwidth, we obtain a minimum detectable absorption of

$$(\alpha d)_{min} = \sqrt{\frac{2eB}{\eta P_0}}. \tag{8}$$

This direct absorption sensitivity is capable of detecting an integrated absorption of 2×10^{-8} for a 1 s averaging time for $P_0 = 1$ mW and a reasonable η (≈ 0.8 A/W).

Needless to say, this number seems optimistic when compared to experience. In practice, noise of various technical origins usually dominates in the low frequency ranges, and actual laser systems display vastly more noise than the shot noise limit. This extra technical noise may originate in inadequately smoothed power-supply potentials, laboratory vibrations that randomly dither the laser's alignment and mode structure, electromagnetic pickup from high-frequency or high-current devices, or unwanted optical feedbacks. In order to avoid excessive low-frequency noise of technical origins, one can use modulation techniques, either on the laser amplitude or frequency, to encode and then detect the absorption at a higher frequency and within a narrower bandwidth. Of course amplitude modulation of the laser will result in an enhanced S/N only if the signal response is nonlinear. Otherwise one just has a high S/N way to see that the laser's power is unsteady. Reduced-background detection techniques (such as polarization and interference spectroscopy) are also often employed to suppress excessive noise.

B. Introduction to Optical Heterodyne Detection

Before we delve into the details of modulation techniques, it is useful to first discuss the principle of optical heterodyne detection. The reason is that modulation detection can often be understood as a heterodyne interaction between one optical field (the carrier) and another (a modulation sideband). The optical power will generally have a time-dependent term if the applied laser field is the sum from two sources, i.e., $[E_1(t) + E_2(t)]^2$. For simplicity

we have neglected important interference details by assuming the two contributing fields to be mutually mode-matched. With $E_1(t) = E_1 \cos(\omega_1 t)$ and similarly for E_2 and ω_2, when the difference of the two applied frequencies is within the detector's response bandwidth, we expect a detected photocurrent of the form $i(t) = \left(i_1 + 2\sqrt{i_1 i_2}\sin(\omega_1 - \omega_2)t + i_2\right)$. We refer to the cross-term at the difference frequency as the heterodyne response. If we had chosen to think of the field E_2 as somehow different, such as a weak field produced by an atomic/molecular sample, one can see one of the advantages of the heterodyne approach; the scale of the beat current can be increased by increasing the amplitude of E_1, which is referred to as the "local oscillator" (LO) field. It is important that the S/N is not degraded by use of a larger LO power, as discussed below.

Any real photodetector will have some output noise, even in total darkness. If we attempt direct detection of a weak signal, the incident power will need to be sufficiently high to overcome the detector's intrinsic noise. Consider the heterodyne case: now the signal-bearing light power is represented by the cross-term between the local oscillator field and the weak signal field, i.e., $i_{\text{sig}} \propto E_1 E_2$. On the other hand, because $E_1 \gg E_2$, the shot noise of the total photocurrent will be dominated by the LO power, i.e., $i_{\text{n}} \propto \sqrt{E_1^2} = E_1$. It is only this noise term that needs to be adequately large to mask the detector noise. So by merely using a stronger LO field, we can overcome the appreciable noise produced by the amplifier circuit that converts the photocurrent into an output voltage. Ideally then, the S/N of the heterodyne detection depends only on the amplitude of the signal beam (E_2) and the LO amplitude is cancelled out in the final S/N ratio (see Fig. 3).

Of course, this LO power can carry laser intensity noise to the detector as well. Any non-fundamental noise imposed on this intensity will be directly converted into unwelcome detection noise. But typically this noise, called "technical noise" to identify its origin, is concentrated at lower frequencies and arises from noise processes with "1/f" frequency dependence. So an important step toward achieving low-noise performance is to place the information-carrying heterodyne signal at a frequency sufficiently high that a negligible level of technical noise is carried by the LO field. This is the usual motivation for using some form of modulation-based signal recovery approach.

Optical heterodyne detection also plays a critically important role in retrieving the full quantum information related to vanishingly small optical power exiting from a cavity QED system operating in the strong coupling regime where the critical photon number is below one. A broad detection bandwidth is desired for a full recovery of quantum dynamics associated with atom–cavity interactions. In this case a balanced heterodyne detection is usually adopted to cancel out the noise associated with the LO.

C. Motivation and Concept of Modulation: Signal Encoding and Extraction

From a time-domain point-of-view, signal detection schemes employing modulation (AC) methods permit comparison of two cases in quick succession. With suitable modulation schemes, these states can represent on-resonance and off-resonance cases, sampled in rapid succession. By simultaneously obtaining and subtracting these two pieces of information, one provides a signal channel with no output unless there is a resonance. The modulation approach therefore allows efficient extraction of weak signals from a noisy background. Lorentzian signal recovery with modulation methods has been well documented [54,55]. In this type of modulation spectroscopy, the modulation frequency is often chosen to be relatively low to avoid distortions of the spectral profile by the auxiliary resonances associated with modulation-induced spectral sidebands. However, this choice of low-frequency operation usually limits the achievable S/N, because of the excess noise of the laser source at low frequencies. To recover the optimum signal size, large (comparable to the absorption resonance width) modulation amplitudes can be employed. In this case, however, the intrinsic line shape is masked by the signal acquisition process.

On the other hand, using modulation frequencies much greater than the width of the spectral feature under study, frequency-modulation (FM) spectroscopy has become one of the most powerful techniques available for sensitive and high-speed detection of weak absorption signals [56–58]. In principle, FM spectroscopy offers detection sensitivity close to that of Eq. (6) by operating at high frequencies where the amplitude noise of the laser source approaches shot noise. A reasonable modulation index is still needed to recover an adequate signal. However, the linewidth broadenings and line shape distortions associated with low-frequency modulation processes are not present in high-frequency FM spectroscopy. Instead, one obtains added spectral features. When scanning through an absorption resonance, each component of the FM spectrum, which consists of a central carrier and weaker sidebands, interacts with a spectral feature, thereby preserving the resolution of the laser. The high bandwidth, or equivalently speaking, a high Nyquist sampling frequency, associated with the high-frequency modulation enables rapid signal recovery.

When received by a square-law photodiode, a pure frequency-modulated spectrum will display no photocurrent at the modulation frequency. This is because the two heterodyne beat signals between the carrier and either sideband are equal in magnitude but opposite in phase. Hence the net result is a perfect cancellation. However, the presence of an absorption feature is revealed as an attenuation and phase shift of one or several of the FM

[21.7.2003–8:32pm] [1–84] [Page No. 18] FIRST PROOFS {Books}4101-Bederson/Pageproofs/3d/4101-Bederson-001.3d (Bederson) Paper: 4101-Bederson-001 Keyword

components. The perfect FM balance is therefore upset, and the resultant optical signal has an amplitude-modulated component. The photocurrent signal can then be phase-sensitively detected using standard radio frequency techniques, yielding an absorption or dispersion line shape, depending upon the detection phase. The redistribution by deliberate FM modulation of some of the carrier power into FM sidebands causes only a slight penalty in the recovered signal size. When the modulation index β is on the order of unity or less, the FM spectrum can be approximated by a carrier [$\approx J_0(\beta)$] and two first order sidebands [$\approx J_1(\beta)$]. (Here J_i is the ith order Bessel function.) If only the carrier is tuned to interact with a narrow sub-Doppler resonance, then the detection process is intrinsically dispersion-sensitive. Assuming the total probe power is still P_0, the detected shot noise current is given by $\sqrt{2eB\eta P_0(J_0^2 + 2J_1^2)} \approx \sqrt{2eB\eta P_0}$. The signal current arising from the heterodyne beat between the carrier and the sidebands becomes $\sqrt{2}\eta P_0 J_0 J_1 \cdot \phi$, where ϕ is the associated resonance phase shift. The relative magnitudes of dispersion and absorption ($\phi = \Delta n \cdot \omega d/c$ and $\Delta n = \alpha \cdot \lambda/4\pi$, where Δn is the resonance-inflicted change of refractive index) set the scale of the equivalent minimum detectable absorption at the shot-noise limit:

$$(\alpha d)_{\min} = \sqrt{\frac{2eB}{\eta P_0}} \frac{\sqrt{2}}{J_0(\beta) J_1(\beta)}. \tag{9}$$

The modulation-dependent function $J_0(\beta)\, J_1(\beta)$ has its maximum value of 0.34 at $\beta \approx 1.1$. Compared to Eq. (8) for the ideal case of homodyne detection, FM heterodyne detection suffers a factor of ~ 4 loss in sensitivity for fixed total optical power. This is a small price to pay for completely avoiding the laser's technical noise. The S/N loss arises in part because of the power reduction resulting from conversion of some of the main carrier to sidebands and in part from the down-conversion of shot-noise from two additional spectral windows by the two sidebands. Carefully executed FM detection can often nearly reach the sensitivity limit set in Eq. (9).

D. Combining Cavity Enhancement with Modulation: Introduction to Cavity-Enhanced FM Spectroscopy

In this and the next sections, we will describe two techniques that combine the cavity enhancement approach with modulation techniques to reach the shot-noise limit. These techniques improve the detection sensitivity by a factor of $2F/\pi$, without the potentially additional noise factors associated with the use of an enhancement cavity. The two approaches are seemingly

quite different, with the first one related to the frequency modulation spectroscopy discussed above, while the second one related to a time-domain picture in the context of cavity field ring-down. In cavity-enhanced FM spectroscopy [59], the on-resonance and off-resonance information is compared at a radio frequency rate. This technique can be applied to both linear and nonlinear (sub-Doppler resolution) spectroscopy. In AC ring-down spectroscopy [60], two slightly different ring-down time constants are compared, one associated with an empty cavity and the other with additional intracavity loss. Typically the comparison rate is in the audio frequency range. The technique is suitable for linear absorption measurements. The differential measurement approach of both techniques allows them to achieve near shot-noise limited absorption sensitivity. As will be evident in the following discussions, the two approaches are intimately related, through the common features of cavity signal enhancement and technical noise rejection toward the shot-noise limit.

As one considers how to probe an external cavity signal with FM techniques, the first approach that comes to mind is to lock the laser frequency to a cavity resonance and then modulate that cavity mode around the desired molecular resonance while monitoring the cavity transmission. This approach represents a simple lock-in derivative line shape recovery process. In order for this method to be successful, it is important to have a tight frequency lock loop between the laser and the cavity because any laser frequency noise relative to the cavity will be converted to amplitude noise. To implement this scheme, a piezoelectric transducer (PZT) is mounted on one of the cavity mirrors. This assembly is used to modulate the cavity length, and the laser tracks the modulation. The modulation frequency is usually limited to the audio range due to mechanical resonances and roll-off in the frequency response of the PZT and mirror assembly. Depending upon the laser's amplitude noise spectral distribution, the attainable modulation frequency may be too low to reach shot-noise limited detection. Using a solid-state Nd:YAG laser locked to a high-finesse ($F = 100{,}000$) cavity (corresponding to a ≈ 1 mHz relative linewidth), a cavity dither at 500 Hz, and lock-in detection, an absorption detection sensitivity of 3×10^{-11} (6.4×10^{-13}/cm) has been measured at 1 s averaging [61].

To benefit from the full noise-reduction advantages of FM spectroscopy, one needs to introduce a high-frequency phase-modulation of the probe field, usually much larger than the resonance linewidth under study. In addition to the laser-cavity locking issue, another obstacle remains; namely, the cavity bandwidth limit. Specifically, FM sidebands at a high frequency are needed to eliminate low-frequency laser amplitude noise, but at the same time the cavity must respond to the sidebands in exactly the same manner as

[21.7.2003–8:32pm] [1–84] [Page No. 20] FIRST PROOFS {Books}4101-Bederson/Pageproofs/3d/4101-Bederson-001.3d (Bederson) Paper: 4101-Bederson-001 Keyword

it responds to the carrier. This will reduce the frequency-to-amplitude noise conversion process. This goal can be realized by frequency modulating the input laser beam at exactly the free-spectral range of the cavity. We then detect and demodulate the cavity-transmitted light at the modulation frequency. Any small residual frequency variations of the laser will still lead to some amplitude fluctuations and phase shifts of the transmitted carrier, but these will also lead to exactly the same amplitude fluctuations and phase shifts of the sidebands, which are transmitted on nearby cavity axial orders. So the transmitted light still accurately represents an FM spectral triplet, with minimal AM conversion caused by the relative laser/cavity frequency jitter. Thus the noise level can approach the intrinsic AM noise level of the laser at the *FSR* frequency.

E. Operation Sensitivity of NICE-OHMS

Figure 4 shows the case where the central component is used to detect the intracavity molecular resonance, illustrating how the sub-Doppler molecular dispersion causes an unbalance of the laser FM spectrum by a phase shift on the carrier component. Initially, all the FM components coincide with their respective cavity modes. When the central cavity mode is tuned over an atomic/molecular resonance, the mode frequency will be pulled by

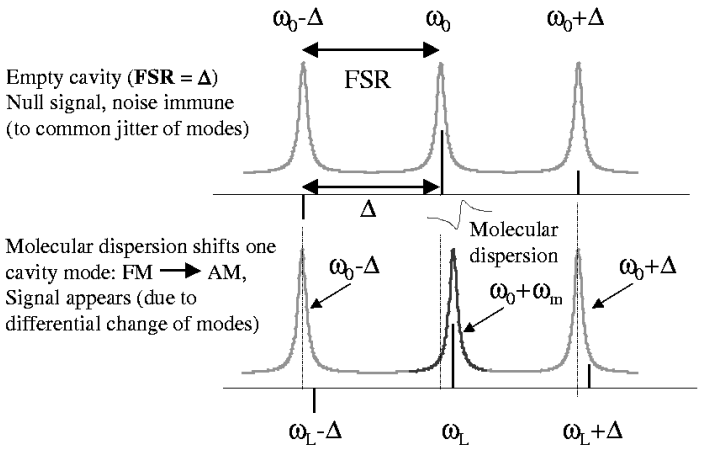

FIG. 4. The optical spectrum and the detection principle for NICE-OHMS: ω_L denotes the laser frequency and Δ is the phase-modulation frequency that matches the cavity FSR. The empty cavity resonance modes are denoted by ω_0 and $\omega_0 \pm \Delta$. The original FM symmetry is upset when the molecular dispersion shifts the cavity resonance (ω_0) by ω_m.

the additional phase shift attributable to the intracavity dispersion. After the phase sensitive demodulation, the detector viewing the transmitted light will generate a dispersion signal in the RF beat. We refer to this technique as (laser frequency-) noise-immune, cavity-enhanced, optical-heterodyne molecular spectroscopy (NICE-OHMS) [34,59,61,62]. This modulation and detection scheme makes it possible to use a high-finesse cavity without introducing additional noise.

To estimate the sensitivity associated with NICE-OHMS, we notice that the cavity-enhancement effect applies only to the signal; no additional noise source has been introduced. Therefore the noise-equivalent absorption signal is that of Eq. (9) for ordinary FM spectroscopy, divided by the cavity enhancement factor ($2F/\pi$). The power in the denominator should be that of the cavity transmitted light, P_t.

This argument can be supplemented with a more rigorous proof. Suppose the molecular dispersion changes the intracavity refractive index by Δn, with the shift of cavity resonance given by ($\Delta n \cdot \omega_0$). Light going through the cavity will thus acquire an extra phase shift of $\phi = \arctan(\Delta n \cdot \omega_0/\gamma)$, where γ is the cavity HWHM (measured in radians). Following the previous treatment and under the assumption of a small ϕ, we derive

$$\phi \approx \Delta n \cdot \omega_0/\gamma = \frac{\lambda}{4\pi}\alpha\frac{\omega_0}{\gamma} = \frac{c}{2\gamma}\frac{\alpha d}{d} = \frac{FSR}{\gamma}\cdot(\alpha d) = \frac{2F}{\pi}\left(\frac{\alpha d}{2}\right). \qquad (10)$$

The signal amplitude is $\sqrt{2}\eta P_t J_0 J_1 \cdot \phi$ and the shot noise limit is $\sqrt{2eB\eta P_t}$. The minimum detectable absorption at $S/N = 1$ is thus,

$$(\alpha d)_{\min} = \frac{\pi}{2F}\sqrt{\frac{2eB}{\eta P_t}}\frac{\sqrt{2}}{J_0(\beta)J_1(\beta)}. \qquad (11)$$

A numerical example follows. Suppose the modulation index, β, is 0.5, and the photodiode responsivity, η, is 0.85 A/W. Also, take the optical power, P_t, to be 5 mW and the detection bandwidth, B, to be $1/2\pi$ Hz, which corresponds to a 1 s time constant. Then, for a single-pass cell, the noise-equivalent integrated absorption, $(\alpha d)_{\min}$, is 2.2×10^{-8}. Under the same conditions, a cavity with a finesse of 100,000 improves the sensitivity to 3.5×10^{-13}. As discussed below, a noise-equivalent sensitivity of 5.2×10^{-13} of an integrated absorption at 1 s averaging has been achieved. This corresponds to an absorption of 1×10^{-14}/cm for a cavity length of 50 cm [61].

F. Implementing a NICE-OHMS Experiment: Signal Line Shape, Size, and Sensitivity

An experimental schematic is shown in Fig. 5. Two electro-optic phase modulators are used to impose two sets of FM sidebands on the laser beam. Modulation at a low frequency, δ, is detected in the cavity-reflected signal and is used to produce a servo error for locking the laser to the cavity. Sidebands at a higher modulation frequency, Δ are set to match the cavity's free-spectral range (*FSR*) and are used to probe the intracavity molecular resonance. This signal is detected in transmission, with adequate optical isolation between the cavity and the photodiode. To study the resonance signal line shape and width, precise scanning capability is important. A frequency-offset locking loop is implemented to permit laser frequency sweeps at an RF resolution. During the scan, the cavity *FSR* changes slightly. To maintain the noise-immune property, the sideband frequency should track this changing *FSR*.

As shown in Fig. 4, the laser spectrum has three major components: the carrier at ω_L and two phase-modulation sidebands at $\omega_L \pm \Delta$. Each of these three components has its own two sidebands located at $\pm\delta$ away from itself, namely at $\omega_L \pm \delta$ $\omega_L + \Delta \pm \delta$ and $\omega_L - \Delta \pm \delta$ which are not shown in Fig. 4. The three corresponding cavity resonant peaks are denoted as ω_0 and $\omega_0 \pm FSR$, with $FSR = \Delta$. The beam reflected from the cavity carries all these frequency components and is detected by a photodetector. Demodulation at frequency δ produces the servo error signal used to lock the laser frequency to the narrow-linewidth cavity. Because of the additional modulation, this locking error signal now has three contributions. These are

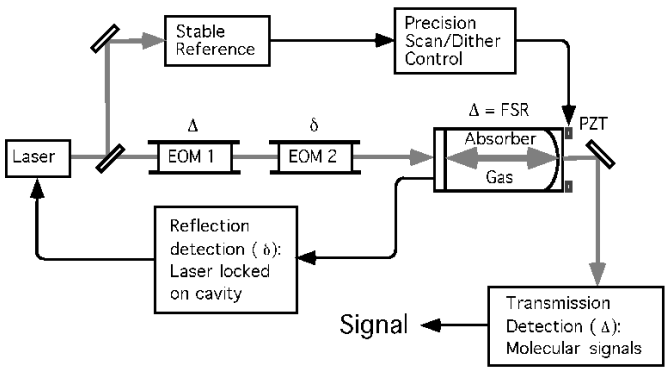

FIG. 5. General schematic of the NICE-OHMS spectrometer, showing the major components of the laser/cavity locking, detection of the transmitted FM triplets, and the precision tuning control.

the two sideband resonances of strength $J_1(\beta)^2$ near $\omega_0 \pm \Delta$, and the carrier contribution $J_0(\beta)^2$ near ω_0. Together, these additively define the lock point. When none of the laser frequency components is affected by a resonance of the intracavity molecules, the servo error signal keeps the carrier, ω_L, and its two sidebands, $\omega_L \pm \Delta$, on the cavity resonance, ω_0 and $\omega_0 \pm \Delta$. Thus, the transmitted beam has the original, perfectly balanced FM spectrum because the carrier (ω_L) and the sidebands ($\omega_L \pm \Delta$) experience the same phase shifts and amplitude attenuations. However, when a molecular resonance affects any of these three components, the interaction converts part of the FM into AM, which is then detected by the photodetector viewing the transmitted light.

For example, as shown in Fig. 4, when a molecular resonance is near the cavity resonance ω_0 the carrier will experience a modified intracavity refractive index, which has been changed by Δn because of the molecular absorption. As a result, ω_0 is shifted by $\omega_m = -\omega_0\ \Delta n$. If we neglect for the moment the servo contributions from the two sidebands, then the carrier ω_L could be kept at the new cavity resonance center ($\omega_0 + \omega_m$). On the other hand, the sidebands, after being shifted to the new positions $\omega_L \pm \Delta + \omega_m$, will no longer line up with cavity resonances. The resulting phase shifts then lead to an AM signal recovered by the detector viewing the transmitted light. In practice, the two sidebands also make limited contributions to the overall laser-cavity locking error signal and they will partially offset the contribution provided by the carrier. The net result is that the laser frequency will be shifted back by its servo in the amount of $x = 2\omega_m\ J_1(\beta)^2$, where x is derived from the requirement that $x\,J_0(\beta)^2 - 2(\omega_m - x)J_1(\beta)^2 = 0$. Here we have used the approximation that $J_0(\beta)^2 + 2\ J_1(\beta)^2 = 1$, valid for the interesting range $\beta \leq 1$. However, this shift of locking point causes little effect on the signal detection because it is very small (< 100 Hz) compared with the cavity linewidth, which is typically a few tens of kHz.

Taking into account the nonlinear molecular phase shift ϕ and the additional phase shift ϕ_x due to the small change in the locking offset, we can express the field of the cavity-transmitted light in the following form,

$$E_t(t) = E_t(0)[J_0 \exp[-i(\omega t - \phi_x)] + J_1 \exp[-i((\omega + \Delta)t + \phi - \phi_x)] - J_1 \exp[-i((\omega - \Delta)t + \phi - \phi_x)]] \quad (12)$$

We can see that the locking offset phase shift ($\exp[-i\phi_x]$) is a common factor for all three contributions and can be factored out. The signal current at the modulation frequency Δ can be readily derived as

$$i_s \propto J_0(\beta)J_1(\beta)\sin(\phi)\sin(\Delta t) \approx J_0(\beta)J_1(\beta)\phi\sin(\Delta t). \quad (13)$$

The signal has a pure dispersion line shape and is independent of the laser/cavity locking point. An important aspect of this line shape is that it contains only the odd-symmetric response $\sim \phi \sin(\Delta t)$, and so the line shape and the apparent line center position are independent of any less than optimal setting of the RF detection phase at Δ.

To reject further noise and minimize baseline drift, a small dither can be applied on the cavity resonance (with the modulation amplitude matching the width of molecular resonance) at a low audio frequency. This allows a lock-in detector to process the demodulated RF signal from the output of the double-balanced mixer that is driven at frequency Δ. Hence, the line shape from the RF channel, resulting from modulation detection of an isolated dispersion resonance, approximates the derivative of a dispersion profile [55]. Indeed, a theoretical line shape fits the experimental data rather well, as shown in the bottom curve of Fig. 6.

As explained earlier, another way to detect the intracavity signal is by simply dithering the cavity resonance onto which the laser frequency is locked. Lock-in detection is applied to the transmitted light. We refer to this low-frequency operation as DC detection, to differentiate it from the high-frequency RF approach of NICE-OHMS. The line shape

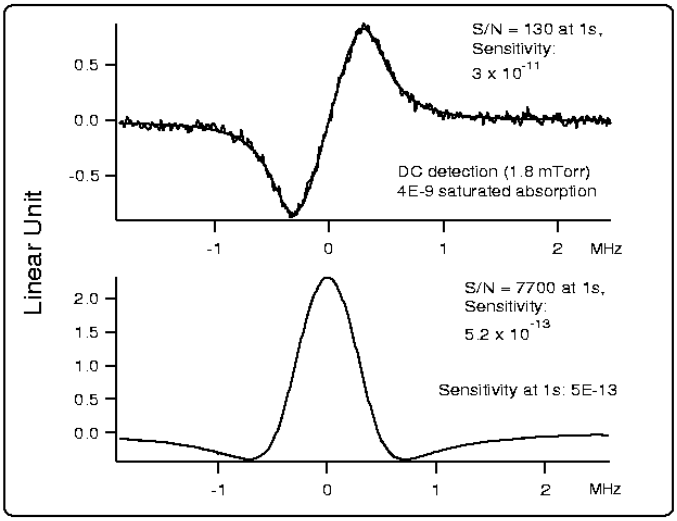

FIG. 6. Sensitivity measurement of the NICE-OHMS technique. The upper graph shows the size of the saturated absorption signal while the lower graph shows the corresponding S/N obtained via NICE-OHMS detection. The noise equivalent detection sensitivities (normalized to 1s time constant) are 3×10^{-11} for cavity dither detection and 5.2×10^{-13} for NICE-OHMS.

measured by DC detection follows the original Wahlquist formula for a modulation-broadened, derivative line shape [54,55]. Figure 6 shows the experimental sensitivity achieved using 1.8 mTorr of gaseous C_2HD. The transition under study is the $(\nu_2 + 3\nu_3)$ P(5) overtone line of C_2HD. The cavity finesse here is 100,000 and the intracavity power ≈ 300 W, giving a saturation parameter of ≈ 1.75 and a saturation peak contrast of 13.2%. The single-pass (46.9-cm-long cavity) linear absorption is about 3×10^{-8}. Therefore the absolute level of saturated absorption by the intracavity molecules is 4×10^{-9}. This is verified by the DC detection of the cavity transmission, shown in the top graph of the figure. With the laser locked to the cavity with a relative linewidth of $\approx$1 mHz, the simple cavity-dither and lock-in detection of the transmission yields a S/N (amplitude/rms noise) of 130 at 1 s averaging. This corresponds to a detection sensitivity of 3×10^{-11} at 1 s. The corresponding S/N from NICE-OHMS detection is 7700 with a 1 s time constant, as shown in the bottom graph of the figure. This translates into a noise-equivalent detection sensitivity of 5.2×10^{-13} at 1 s averaging, $\approx$1.5 times worse than the calculated shot-noise limit. The NICE-OHMS result is about sixty times better than the straightforward dither detection, because of its higher modulation frequency and its insensitivity to the laser frequency noise relative to the cavity. We emphasize that the gain in sensitivity by NICE-OHMS over simple dither detection is even more impressive when the laser is not well stabilized to the cavity. This high detection sensitivity of the NICE-OHMS method has opened up many possible spectroscopic applications, especially for studies of weak, high-order vibration overtone transitions of various molecules of interest. For example, weak transitions of C_2HD [59], C_2H_2 [62,63], CO_2 [61], O_2 [26], CH_4 [64], CH_3I [65], and H_2O in the near infrared regions have already been investigated using the NICE-OHMS approach.

Comparing NICE-OHMS and DC signals gives us an appreciation for the noise-immune nature of the NICE-OHMS detection, as shown in Fig. 7. This figure shows signals collected using the two techniques under two different laser/cavity lock conditions. In one set of experiments, the laser and cavity were tightly locked, and in the second, the laser/cavity lock was deliberately set to be loose and even oscillating. We can now compare the recovered S/N ratios before and after the lock was sabotaged. The DC detection of the intracavity molecular absorption (upper row) is shown to be critically dependent upon the performance of the laser/cavity lock. (A fast laser/cavity frequency-lock servo was used for the graphs obtained in the left column while a slow and noisy servo was used for those in the right column.) However, increased laser frequency noise relative to the cavity yields little effect in FM detection (bottom row).

[21.7.2003–8:32pm] [1–84] [Page No. 26] FIRST PROOFS {Books}4101-Bederson/Pageproofs/3d/4101-Bederson-001.3d (Bederson) Paper: 4101-Bederson-001 Keyword

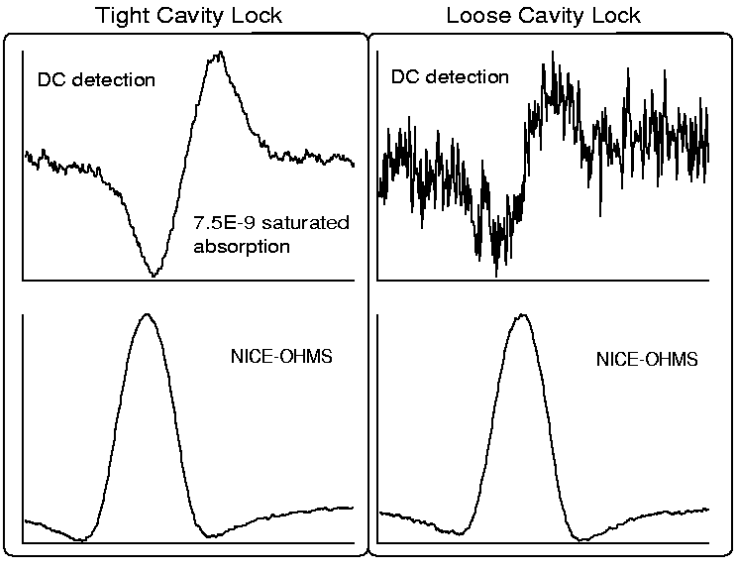

FIG. 7. Demonstration of the noise-immune property of the NICE-OHMS technique. The C_2HD ($\nu_2 + 3\nu_3$) P(5) resonance signal is recovered by both cavity-dither lock-in (DC) detection and the NICE-OHMS technique, under the conditions of a tight laser/cavity lock (left column) and a poor lock (right column).

There is an optimum value of the intracavity sample pressure for the maximum signal size. An increase of pressure raises the linear absorption, but at the same time reduces the level of saturation because of the pressure-broadening of the homogeneous transition width. For fixed cavity parameters, change of pressure also influences the input power coupling. A useful model of this behavior is based on an axially averaged field picture [66,67] in which the moving molecules interact with the average standing intracavity field. At line center, the counter-propagating waves interact with the same molecules, thus causing the absorption coefficient to be reduced from the off-resonance value of $\alpha_0/\sqrt{1+S}$ to $\alpha_0/\sqrt{1+2S}$. Here α_0 is the linear absorption coefficient at the center of the Doppler profile and S is the saturation parameter. The observed nonlinear signal is thus proportional to

$$\Delta\alpha = \frac{\alpha_0}{\sqrt{1+S}} - \frac{\alpha_0}{\sqrt{1+2S}}. \tag{14}$$

To perform detailed calculations on signal size, we use Eqs. (2) and (3) to determine the cavity transmission, along with the following useful

relations: $\Delta n = (\Delta\alpha\lambda)/(4\pi)$, $\alpha_0 = \alpha_p \cdot P$, $S = I/I_{\text{sat}}$, and $I_{\text{sat}} = I_0 \cdot (\Gamma_T + \Gamma_0 \cdot P)^2$. Here Δn is the refractive index change caused by the saturated molecular resonance; α_{p} is the molecular absorption coefficient per unit length and unit pressure; P is the gas pressure; I_{sat} is the required saturation intensity; Γ_{T} is the residual linewidth, at zero pressure and zero power attributable to transit time broadening; Γ_0 is the pressure broadening coefficient; and I_0 is a power-scaling constant that can be determined experimentally. The natural linewidth ($\approx$kHz) of a vibrational overtone transition is negligible in a saturation calculation because transit time broadening at room temperature is typically a few hundred kilohertz for a normal cavity mode waist size. Under the current settings of cavity finesse and C_2HD overtone transition strength, the optimal pressure is ~ 10 mTorr.

G. NICE-OHMS Application: Highly Stable Optical Frequency Standards and Molecular Dynamics of High-Vibration States

The NICE-OHMS technique can provide information about the line centers for weak molecular lines in the visible wavelength region at metrological precision. The narrow linewidths associated with saturated line shapes are especially useful, as the line centers are narrowly defined, which improves the long-term stability of a light source locked to such a transition. Moreover, the high S/N ratio improves short-term stability, permitting more effective comparisons between various frequency standards. For example, although the transition strength of the C_2HD overtone line is ~ 1 million times weaker than the I_2 electronic transition commonly used for laser frequency stabilization at 532 nm, the obtained S/N for C_2HD via NICE-OHMS is only slightly smaller than that of I_2. With a narrower linewidth, the resultant frequency stability of a C_2HD-based system becomes comparable to that of the I_2-stabilized system [68,69].

The NICE-OHMS spectrometer provides laser frequency discrimination information relative to both the cavity resonance and the molecular transition. It is thus an ideal system with which to achieve simultaneously good short- and long-term frequency stabilizations. We should note that although the requirement of the laser/cavity locking is much more relaxed for NICE-OHMS than for direct cavity transmission detection, the laser linewidth still needs to be narrowed so that a stable optical power is effectively coupled into the cavity. For metrology purposes, this laser/cavity locking loop serves as the short-term frequency stabilizer. Modern laser cavity stabilization loops can routinely track the laser frequency to the cavity resonance to within a few millihertz. The vibrational noise and long-term drift in the cavity can be suppressed by stabilizing the cavity to an

intracavity molecular resonance. The NICE-OHMS signal is intrinsically dispersive when the molecular resonance is probed by the carrier of the FM triplet. Used for locking, this could basically eliminate the influence of the local oscillator frequency drift on the recovered line center. In practice it is necessary also to dither the cavity length and make a second-harmonic signal recovery of the RF mixer output. This is partly to suppress the baseline-offset problem associated with the imperfect FM modulation at the *FSR* frequency. Another important issue concerns the final line shape under the conditions of FM with a residual AM part (RAM) [70,71]. The effect of RAM is to add an even-symmetric absorption-phase component to the originally pure dispersion line shape. Unfortunately, this line shape alteration caused by RAM cannot be corrected by the cavity-dither process. To achieve the best stabilization results, it is crucial that the FM has a zero (or at least a small constant) residual AM.

To demonstrate that NICE-OHMS is useful for laser frequency-stabilization, a Nd:YAG laser at 1.064 μm stabilized on an overtone transition of C_2HD is compared against a frequency-doubled Nd:YAG/I_2 reference system [68]. (The 532 nm-stabilized laser has a stability $\approx 5 \times 10^{-14}$ at 1 s, as determined from beating experiments with two I_2-stabilized systems.) Figure 8 shows the counted beat frequency versus time. The drift is ~ 5 Hz/h and a 60 Hz frequency noise at 1-s counter gate time, in agreement with the S/N available from the C_2HD resonance at 1.064 μm. One representation of frequency stability is the Allan variance [72], which is determined by comparing adjacent frequency measurements and then averaging over the whole data set. For a set of N frequency measurements, f_n, each with a sampling time τ, the corresponding Allan variance is defined as $\sigma_y^2(\tau) = 1/(2(N-1)) \sum_{n=1}^{N-1} (f_{n+1} - f_n)^2$. The Allan variance permits one to separate and isolate different noise processes based on their characteristic

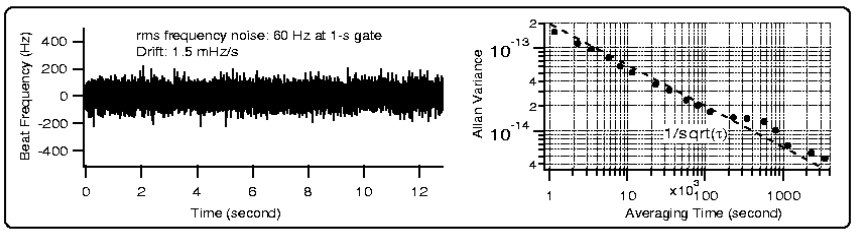

FIG. 8. Stability of beat between I_2-stabilized and C_2HD-stabilized Nd:YAG lasers. Allan deviation is determined from the beat record. The frequency noise of the beat is still limited by the C_2HD system, which is about three times worse than the I_2 system. However, the strength of the C_2HD transition is about one million times weaker than the I_2 transition.

time scales. Rather than the variance, it is customary to plot its square-root, called the Allan deviation. In the short-time domain, the Allan deviation typically displays a slope of, where τ is the averaging time. This is because the main contribution to the fast noise originates from white frequency noise, for example, shot noise. One sees from this argument that the level of this short-term deviation is controlled by the ratio between the frequency discrimination linewidth and its S/N. Figure 8 also shows the Allan deviation determined from the beat record of the two stabilized lasers. The frequency deviation is normalized to the optical carrier frequency, i.e., 282 THz (1.064 μm). The Allan deviation of $\sigma_y = 2 \times 10^{-13}/\sqrt{\tau}$ improves to 6×10^{-15} at a longer integration time (> 1000 s). This frequency stability, achieved by locking to an extremely weak reference transition, is a direct result of the spectrometer's high detection sensitivity. Notice that the C_2HD-stabilized system shows only three times more frequency noise than the I_2 system, which is notable because the I_2 transition strength is approximately a million times stronger. The short-term frequency stability of optical sources can be comparable to or better than the state-of-the-art microwave standards. However, the reproducibility and accuracy of cell-based optical frequency measurements are not yet comparable to microwave standards.

One approach to reducing some of the systematic shifts of the reference frequency is to slow down the motion of the target quantum absorber, thereby reducing the second order Doppler effect. Slower speeds also imply longer interaction times. Slower molecules give a narrower linewidth because the natural lifetime of vibrational transitions usually far exceeds (more than 300 times, for the acetylenes) the transit-controlled interaction time, limited by the laser field dimensions. While effective schemes for molecular cooling and trapping are emerging, optical selection of slow molecules based on interaction time has been actively pursued since the late 1980s [73–75]. The idea is this: the homogeneous linewidth originating from collisional broadening can be reduced by lowering the gas pressure until the mean-free-path of molecules becomes much larger than the transverse dimension of the optical field. This is referred to as the transit-time regime. To optically select slow molecules, a low optical power is necessary so that the low Rabi frequency leads to appreciable saturation only for the slowest molecules. The observed signal is thus dominated by interaction with the slowest molecules and consequently the effective interaction time is increased, limited finally by saturation and residual pressure broadening. Unfortunately, this avenue toward linewidth reduction is expensive in S/N, scaling approximately according to the fifth power of the instrumental resolution increase.

In the free-flight regime, molecules with the mean thermal velocity cross the laser beam without suffering any collision. In other words, if we define

[21.7.2003–8:32pm] [1–84] [Page No. 30] FIRST PROOFS {Books}4101-Bederson/Pageproofs/3d/4101-Bederson-001.3d (Bederson) Paper: 4101-Bederson-001 Keyword

the collision-broadened homogeneous linewidth (the half-width at half maximum) as Γ_p and the transit-time linewidth as Γ_T, then $\Gamma_p \ll \Gamma_T$, with $\Gamma_T = (\pi/4)\,\langle V_\perp \rangle / w_0$, where w_0 is the laser beam-waist radius and $\langle V_\perp \rangle$ is the mean transverse velocity. The situation changes for the slowly moving molecules. In fact, the slowest molecules are those with transit times longer than the inverse of the collisional linewidth Γ_p. And therefore these molecules are in a collisional regime and they have a constant and velocity-independent saturation parameter S, controlled primarily by the collisional broadening,

$$S = \frac{\mu^2 E^2}{\hbar^2 \Gamma_p^2}, \tag{15}$$

where μ is the transition dipole moment and E is the optical field amplitude. Faster molecules with transit time shorter than $1/\Gamma_p$ are in a free-flight regime, and their saturation parameter depends on their transverse velocity. Defining τ as the interaction time ($\approx 4w_0/V_\perp$) then S equals unity when$(\mu E/\hbar)\tau = \pi$. The optical power required to saturate molecules with transverse velocity $V_\perp$ is thus

$$\text{Power}_{(S=1)} = \left(\frac{c\varepsilon_0}{2} E^2\right) \pi w_0^2/2 = \frac{c\varepsilon_0}{2} \left(\frac{\pi\hbar}{\mu} \frac{V_\perp}{4w_0}\right)^2 \frac{\pi w_0^2}{2} = \frac{\pi^3}{64} \frac{\hbar^2 c\varepsilon_0}{\mu^2} V_\perp^2. \tag{16}$$

Interestingly, the saturation power is independent of the optical field mode size in the free-flight regime. However, the necessary saturation power does increase as the square of the transverse velocity, and it can be vastly different for slow and average thermal molecules because it has been assumed that $\Gamma_p \ll \Gamma_T$. In short, a sufficiently low gas pressure can be used to create a free-flight regime, and a low power laser beam then optically selects for the slow molecules. The selection is based on the saturation effect in the recovered resonance signal. The resulting signal linewidth becomes strongly inhomogeneous, with molecules from different transverse velocity groups contributing different intensities and widths. Slow molecules will dominate the contribution to the signal amplitude, and the width is essentially the homogeneous linewidth Γ_p. Faster moving molecules will see a reduced saturation and will mostly contribute to the wings of the resonance. The width is caused by transit effects and increases with velocity.

This concept has been demonstrated using NICE-OHMS. In the experiment, a < 2 mTorr sample gas was used, and the mean-free-path of molecules is ~ 30 times longer than the transverse optical field dimension. The cavity input power was reduced by almost two orders of magnitude

from normal operation. Although the intrinsic transition width associated with the $(\nu_2 + 3\nu_3)$ P(5) line of C_2HD is on the order of kHz, the observed linewidth (FWHM) is 705 kHz under normal experimental conditions similar to those of Fig. 6. This linewidth includes contributions from the power-saturation and pressure-broadenings of the 270 kHz transit time linewidth. Working with slow molecules Fig. 9 shows a resonance linewidth of ~ 20 kHz. This is thirteen times narrower than that set by the room temperature transit-time-limit and is mainly limited by the relatively high pressure (1.8 mTorr). The selected molecules have a temperature of ≈ 1.8 K. The S/N ratio is vastly reduced, as the optical power is much smaller than usual and the majority of molecules do not contribute to the observed saturation signal. In fact, compared with the number of molecules participating in normal saturation spectroscopy, the slow molecule selection process has selected only a fraction of 0.75%. At present the limited S/N associated with the low power has prevented us from taking full advantage of this narrow linewidth. With an improved system this approach will enable us to access the information of free molecules with minimized second order Doppler shift, thereby creating an optical frequency standard of potentially high accuracy.

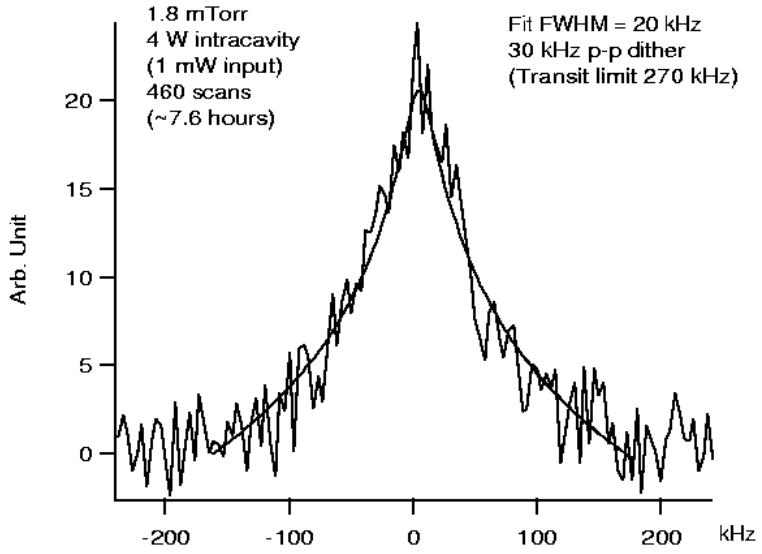

FIG. 9. With low power and low gas pressure, optical selection of slow molecules produces a linewidth thirteen times below the room-temperature transit-time-limit.

V. Weak Absorption Measured by Field Decay (Time-Domain)

This section discusses cavity-enhanced methods for measuring very weak absorptions in the time domain. In these measurements, two cavity modes, one probing the empty cavity and the other probing intracavity absorption, are present simultaneously but the intensities are temporally out of phase, with one mode decaying and the other rising, when viewed in cavity transmission. Heterodyne detection between the two modes reveals the dynamic time constants associated with the empty cavity and the intracavity gas absorption. Quick, differential measurement eliminates a great deal of technical noise. This is essentially an improved version of the cavity ring-down technique and it yields a 1×10^{-10} absorption sensitivity using microwatt-level laser powers.

A. Introduction to Cavity Ring-Down Spectroscopy and Overview of the Field

Inside a high-finesse cavity, light completes many round-trips, and this effectively increases the path length by $(2F/\pi)$. Cavity ring-down spectroscopy (CRDS) exploits this cavity-enhancement property by measuring the decay of the intracavity field during these many round-trips. Because the decay rate increases when an absorber is placed inside the cavity, this method can be used as a spectroscopic tool. For example, an unknown absorption coefficient is determined by comparing the known mirror losses to the cavity losses in the presence of the absorber. Ideally, the mirror losses should be of the same order of magnitude as the absorption level to be measured, because this makes the ''background'' comparable to the ''signal'' and increases the measurement sensitivity. Because CRDS measures the decay dynamics after the field has built up inside the cavity, it largely eliminates the technical noise of the incident radiation field.

However, as commonly implemented, CRDS has two shortcomings. The first is that CRDS, in its ordinary form, is a long time-interval measurement. Two decay-time measurements are made, one on the empty cavity decay and the other on cavity plus sample. The difference between the two measured decay rates contains the desired intracavity absorption information. However, the time between the two measurements allows slow drifts and other technical noise to contaminate the data. The second problem is that technical noise is the dominant noise source in the signal beyond the point where the field's shot noise equals the instrument's technical noise. To overcome this limitation, a heterodyne technique was developed [76] that

superimposes a large local oscillator field onto the decay field so that the resultant beat signal can always be shot-noise limited. However some form of modulation strategy is still needed to achieve a rapid differential measurement.

With a modulation technique to compare signal against background at short time intervals, one can accurately subtract background noise from the useful signal. In the context of CRDS, two decay constants are to be compared in quick succession, one associated with the empty cavity loss (off-resonance for the intracavity gas sample) and the other associated with the total intracavity loss. This concept can be realized if two different optical frequencies are coupled into two cavity modes, one mode centered on the molecular transition and the other far away from it. With the aid of a quick switching between the two frequency components and a subsequent heterodyne detection for their product, it is possible to reach the quantum-noise limited detection sensitivity to within a factor of 4 [60].

B. Concept of AC Ring-Down—Separating the Ring-Down Fields Associated with Cavity and Molecules

Figure 10 illustrates the basic scheme of the alternating-constant (AC) ring-down method. A continuous-wave (cw) laser beam is split by two acousto-optic modulators (AOMs) into two beams with a frequency offset such that both beams can resonate with respective cavity modes simultaneously. The frequency offset is large enough so that only one beam can be tuned onto the intracavity Doppler-limited molecular resonance at a time. The two beams are spatially combined and mode-coupled into the cavity. However, the two optical beams are switched by their respective AOMs, such that only one beam at a time is present at the cavity input. Despite the switching, a detector viewing in cavity reflection is able to maintain the laser/cavity lock using the FM technique [77]. Inside the cavity there is one decaying mode and one rising mode. That is, on the scale of one ring-down time constant, the cavity mode that is being coupled in will rise exponentially while the other mode, with its input switched off, will decay exponentially. The heterodyne beat waveform between the two modes is detected in transmission. Demodulation against the known carrier frequency then yields the heterodyne beat amplitude, which contains information on the dynamic variation of both modes. In the case of an empty cavity, the beat amplitude waveform remains unchanged at neighboring switching cycles. However, when a mode is tuned to a molecular resonance, the system exhibits two slightly different time constants. The beat waveform becomes asymmetric between the adjacent cycles, and the difference is related to the intracavity absorption. The period of a switching cycle can be chosen to

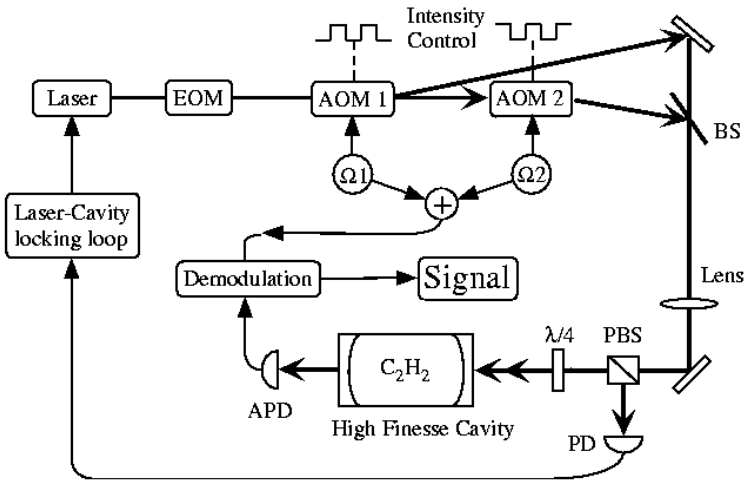

FIG. 10. Experimental set-up for switched heterodyne ring-down spectroscopy. The two AOMs provide the necessary frequency offset between the two cavity modes and are switched out-of-phase. Both beams are stabilized to their respective cavity resonance modes. The heterodyne beat between the two modes at the cavity transmission is demodulated against the known carrier frequency to produce the decay signal. PD: photodiode; APD: avalanche photodiode; PBS: polarized beam splitter.

roughly match the field decay time ($1/e$) of the empty cavity. This technique thus offers a quick comparison of on-resonance and off-resonance information and substantially suppresses technical noise. Because each ring-down waveform is measured during a switching period that is on the order of the $1/e$ field decay time, shot noise dominates throughout the signal acquisition.

To expand the foregoing discussion, consider the following theoretical model for this technique. Suppose the round-trip loss of the empty cavity is L_{cav}, the round-trip absorption of the intracavity medium is $2\alpha d$, and the round-trip time of flight within the cavity is $t_{\text{round-trip}}$. For a cavity mode that is far detuned from the sample resonance, the characteristic time constant associated with the mode dynamics is given by

$$\tau_{\text{cav}} = \frac{2t_{\text{round-trip}}}{L_{\text{cav}}}. \tag{17}$$

We note that this is the $1/e$ decay time of the *field*, a relevant quantity because the heterodyne signal is proportional to the product of the two

fields. For the mode that is tuned to the absorption, the decay time constant becomes

$$\tau_{\text{abs}} = \frac{2t_{\text{round-trip}}}{L_{\text{cav}} + 2\alpha d}. \tag{18}$$

Following the intensity-switching scheme of Fig. 10, let us assume that during the interval $[0, \Delta t/2]$, mode 1 (E_1) of the empty cavity is switched on, while mode 2 (E_2), which sees the additional intracavity absorption, is switched off. The two field amplitudes evolve as

$$\begin{aligned} E_1 &= c_1[1 + \exp(-\Delta t/t\tau_{\text{cav}}) - \exp(-t/\tau_{\text{cav}})], \\ E_2 &= c_2 \exp(-t/\tau_{\text{abs}}) \end{aligned} \tag{19}$$

Here c_1 and c_2 are amplitude coefficients for E_1 and E_2, respectively. In the next half cycle, $[\Delta t/2, \Delta t]$, we reverse the two fields such that mode 1 is switched off and mode 2 on. The product of the two field amplitudes is what we detect in the demodulated signal of the cavity transmitted heterodyne beat. If we compare the signal of the two neighboring half-cycles, we obtain the absorption-dependent signal in the following form:

$$\begin{aligned} (E_1E_2)_{[0,\Delta t/2]} - (E_1E_2)_{[\Delta t/2,\Delta t]} = c_1c_2\big[&\big(1 + \mathrm{e}^{-(\Delta t/2\tau_{\text{cav}})}\big)\mathrm{e}^{-(t/\tau_{\text{abs}})} \\ &- \big(1 + \mathrm{e}^{-(\Delta t/2\tau_{\text{abs}})}\big)\mathrm{e}^{-(t/\tau_{\text{cav}})}\big]. \end{aligned} \tag{20}$$

To determine the fundamental limit of sensitivity obtainable by this method, suppose the two modes have the same amplitude coefficients, $c_1 = c_2 = \sqrt{P_0}$, in transmission, and the light is converted to a photocurrent according to $i = \eta \times P$, where η is as before the detector responsivity. The demodulated beat current is $\eta \times 2E_1E_2/\sqrt{2}$. For simplicity of presentation, we take the small absorption limit, $\tau_{\text{cav}} \approx \tau_{\text{abs}}$, and assume $\Delta t/\tau_{\text{cav}} \geq 10$. The difference signal of Eq. (20) becomes

$$\begin{aligned} i_{\text{signal}} \approx \eta\frac{2}{\sqrt{2}}P_0\big[\mathrm{e}^{-(t/\tau_{\text{abs}})} - \mathrm{e}^{-(t/\tau_{\text{cav}})}\big] &= -\eta\sqrt{2}P_0\mathrm{e}^{-(t/\tau_{\text{cav}})}\big[1 - \mathrm{e}^{-t((1/\tau_{\text{abs}})-(1/\tau_{\text{cav}}))}\big] \\ &= -\eta\sqrt{2}P_0\left(\frac{1}{\tau_{\text{abs}}} - \frac{1}{\tau_{\text{cav}}}\right) \times t \times \mathrm{e}^{-(t/\tau_{\text{cav}})}. \end{aligned} \tag{21}$$

Because the beat amplitude reaches a maximum when $E_1 = E_2$, we have $\exp(-t/\tau_{\text{cav}}) \approx 1/2$, and $t = \tau_{\text{cav}} \ln 2$. Using Eqs. (17) and (18), we obtain

$$i_{\text{signal}} = -\eta\sqrt{2}P_0\tau_{\text{cav}}\frac{\ln 2}{2}\frac{2\alpha d}{2t_{\text{round-trip}}} = -\eta P_0\frac{\ln 2}{\sqrt{2}}\frac{2\alpha d}{L_{\text{cav}}}. \tag{22}$$

The shot noise produced by the photocurrent, $i_{DC} = \eta \cdot 2\left(\left(\sqrt{P_0}\right)/2\right)^2 = \eta P_0/2$, is $i_{noise} = \sqrt{2eB \times \eta P_0/2}$. The resultant S/N is thus,

$$\left|\frac{i_{signal}}{i_{noise}}\right|_{\substack{shot \\ noise}} = \sqrt{\frac{\eta P_0}{eB}} \frac{\ln 2}{\sqrt{2}} \frac{2\alpha d}{L_{cav}}. \tag{23}$$

To find the noise-equivalent sensitivity of single pass integrated absorption, we set $S/N = 1$, and obtain

$$(\alpha d)_{min} = \frac{1}{\ln 2} \sqrt{\frac{2eB}{\eta P_0}} \frac{L_{cav}}{2} = \frac{2}{\ln 2} \sqrt{\frac{2eB}{\eta P_0}} \frac{\pi}{2F}. \tag{24}$$

Compared to Eq. (8), we see that except for a numerical factor of ~ 3, the shot noise limited AC ring-down spectroscopy provides a detection sensitivity enhanced by the familiar factor of $(2F/\pi)$ over the fundamental limit of direct absorption measurement.

To relate the model to experimental observations, Fig. 11 visualizes switching results obtained from Eqs. (19) and (20). The switching period, Δt, is chosen to be $4\tau_{cav}$, and the time axes have been normalized to τ_{cav}. In the case of an empty cavity, shown in the right column, the switched waveforms of mode 1 and mode 2 are totally symmetric, resulting in an equivalent signal of the beat amplitude during adjacent half-cycles; thus the difference gives a zero baseline. When mode 1 and mode 2 see different intracavity loss, as shown in the left column of the figure, there is a clear asymmetry in the heterodyne beat amplitudes between the adjacent half-cycles. The differences, as plotted in the bottom curve, show the level of additional absorption. In this case, the sample absorption is 10% of the empty cavity loss.

C. Experimental Results of AC Ring-Down Spectroscopy

The concept discussed in the preceding section has been demonstrated in the measurement of rovibrational transitions of acetylene. The experiment used a Yb:YAG laser. The transition involved was the $3\nu_3$ R(29) overtone of C_2H_2, located at 1031.6528 nm, with an absorption coefficient of 4×10^{-6} $(\text{Torr.cm})^{-1}$. In the 46.9 cm long cavity with a finesse of 90,000, a few milliTorr (1 Torr = 133 Pa) of gas was typically used, giving 1×10^{-6} level of absorption. The beam switching frequency was 1.4 kHz, corresponding to $\Delta t = 714\,\mu s$. The cavity transmission was received by an avalanche photodiode (APD), and the beat signal was sent to an RF spectrum

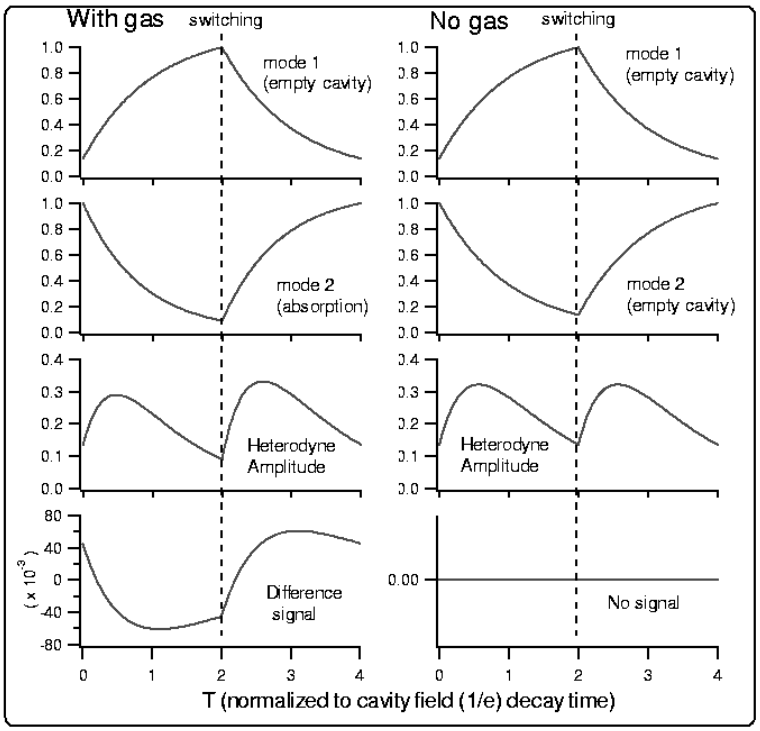

FIG. 11. Comparison of the demodulated ring-down curve between the empty cavity (right column) and the cavity with additional absorption (left column). The switching period $\Delta t = 4\tau_{cav}$, and the time axes are normalized to τ_{cav}. Shown from top to bottom are the switching dynamics of mode 1, mode 2, their product (beat), and the difference signal between the neighboring half cycles.

analyzer for demodulation. The frequency reference of the RF spectrum analyzer was connected to the RF signals used to drive the AOMs. In the linear amplitude display mode, the video output of the spectrum analyzer in zero-span-mode provides a phase-insensitive demodulation for the heterodyne beat. To measure the empty cavity finesse, both mode 1 and mode 2 were tuned out of the molecular resonance. The experimental results were in excellent agreement with the model presented above.

Mode 2 is then tuned to the center of the acetylene resonance, and the ring-down waveform becomes clearly asymmetric in the neighboring half cycles. Figure 12 shows a set of experimental data where intracavity gas pressure was varied to generate four different intracavity absorption levels (expressed in terms of single-pass in the graph). The respective ring-down

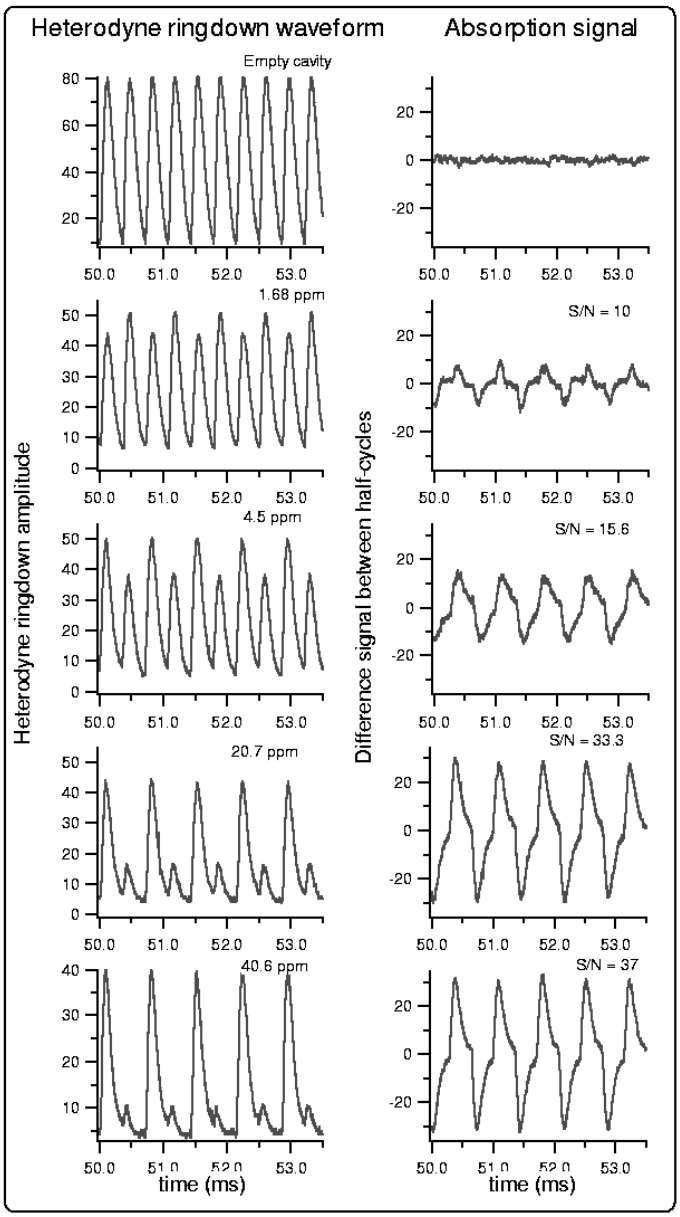

FIG. 12. Demodulated heterodyne beat amplitudes between the two switched cavity modes (left column) in the presence of intracavity absorption (labeled in the graph). Shown in the right column is the absorption signal obtained by differencing the beat amplitudes in the adjacent half cycles.

beat waveforms are shown in the left column of the figure. The absorption data (shown in the right column) were produced in the following way. First, a copy of the original data was shifted by a half switching cycle along the time axis. The differences between the original data and the shifted data gave the absorption signals. With a single pass absorption of 1.7×10^{-6}, the absorption sensitivity normalized to 1 s averaging time was 1.6×10^{-10}. In steady state (no switching), each mode has 3 μW (P_0) in the cavity transmission. Given an η for the APD of 0.3 A/W, the shot-noise limited sensitivity is $\sim 1.2 \times 10^{-11}$ at 1 s averaging. However, because the APD has an excess noise factor of ~ 3 the expected minimum absorption sensitivity was $\approx 4 \times 10^{-11}$, which is within a factor of 4 of the experimental results.

Further improvement of the system includes the use of faster switching cycles and the replacement of the APD with a sensitive P-I-N diode in a resonant matching circuit. At present the switching frequency is limited by the locking loop between the laser and the cavity. After all, the sideband locking system also uses the heterodyne principle, in this case the beat is between the field of the direct reflection off the cavity input mirror and the field leaked out from the cavity storage. If the mode is switched too fast, the cavity field does not have sufficient time to establish itself as the frequency/phase reference for the incident instantaneous laser field to compare against. An alternative is to stabilize the laser on the cavity with a third mode, completely away from the molecular resonance and independent of the other two modes. The third mode can be left on continuously to maintain lock while the switching can go on as before between the first two modes. The heterodyne detection RF system can conveniently filter out the contribution from the third mode. The only penalty in this arrangement is a somewhat increased level of shot noise, resulting from the added contribution of the third mode to the photocurrent. A hybrid of the on-resonance/off-resonance switch with transmission heterodyne detection against the third mode is another clear avenue for high-sensitivity detection.

VI. From Optical Frequency Metrology to Ultrafast Technology

Optical cavities have played a central role in laser stabilization and related precision optical frequency metrology over the past three decades [78]. To stabilize a laser, one needs to employ some kind of resonance information to derive a frequency/phase-dependent discrimination signal. The resonance can be of material origin, such as modes of an optical cavity, or of natural origin, such as atomic or molecular transitions. The saturation of an atomic

transition limits the attainable S/N for the servo error signal, which in turn limits the useful bandwidth of the stabilization loop. In contrast, an optical cavity can provide a high contrast and basically unlimited S/N for resonance information. Suitably narrow resonance linewidths can be easily accommodated with modern technologies of low loss mirror coatings. Careful design and control of the material properties can bring the stability of an optical cavity to a satisfactory level. For the most demanding applications in ultrahigh-resolution laser spectroscopy [79] and high-precision optical frequency metrology, an optical cavity has become an indispensable tool to narrow the linewidth of a laser so that it can be effectively used to interrogate optical transitions of extraordinary Q. When the desired quantity of a stabilized laser is its long-term stability or reproducibility, the use of a natural resonance then becomes necessary, often in combination with the use of a pre-stabilization cavity. Discussions presented in Section IV.G provide an example of this strategy. With the recent emergence of a remarkable synergy between cw laser-based precision optical frequency metrology and mode-locked ultrafast lasers [80], precision control of the frequency spectrum of a mode-locked laser, and consequently of the time-domain evolution of its carrier-envelope phase, has been actively pursued with a great success [81]. A passive optical cavity has now been used to directly stabilize a mode-locked femtosecond laser [82].

To accommodate this diverse set of applications, it is important to develop an improved understanding of the cavity and associated mirror properties. This knowledge is essential for achieving enhanced detection sensitivity, for obtaining optimum system design, and for reducing systematic errors. For example, in cavity QED, one needs to know the mode structure of the intracavity field in order to quantitatively predict the atom-cavity coupling; for frequency metrology, accurate determination of phase shifts of the resonant fields can provide precision frequency markers; for ultrafast laser applications, *a priori* information on spectral phase shift of cavity mirrors determines the intracavity dispersion compensation schemes; and in quantitative spectroscopy, knowledge of the mirror loss sets the accuracy scale of absorption measurement. On the technology development side, the knowledge gained from careful mirror characterization could provide guidelines for the optic coating community to develop in situ measurement and control capabilities of the coating process.

The progress in preparation and understanding of mirrors of exceedingly low reflection losses has indeed been spectacular, with feasible cavity finesse now exceeding 1 million. The art of ''superpolishing'' substrates to Angstrom-level surface roughness has been developed, augmented by the technique of depositing 40–50 alternating layers of high and low index dielectric materials, leading to mirrors with losses guaranteed to be below

5 parts in a million. Losses of about 1 ppm have been documented over selected submillimeter-squared areas [83]. The resulting sharpness of the associated cavity fringes is breathtaking to contemplate; one fringe full width is represented by a distance below $10^{-2}\,\text{Å} = 10^{-12}\,\text{m}$. When we now feed this interferometer with a milliWatt of technically quiet coherent light, in a 1-s averaging time – if all goes well and we have only shot noise as the limitation – these fringes can be effectively subdivided into about 10 million parts. The resulting distance resolution is $10^{-19}\,\text{m}$! Sensitivity to these incredibly small distances changes has attracted wide attention in many potential applications, including the possibility of building interferometric antennas for gravitational-wave radiation [27,28].

In the following two sub-sections (VI.A and VI.B) we will discuss the application of the cavity-based optical frequency metrology techniques to various precision measurement tasks, such as characterizing cavity birefringence to a level of $\Delta n/n \sim 10^{-17}$ at 1-s averaging time for potential search of vacuum birefringence [84], or establishing a cavity-based optical frequency reference grid with sub-Hertz precision [85]. In VI.C and VI.D we will establish a connection between the recently developed femtosecond-laser-based optical frequency comb technology and high-finesse optical cavities [82] and explore an interesting application of passive amplification of ultrashort pulses based on cavity-assisted control of pulse repetition frequency and its carrier-envelope phase [86].

A. Mirror Birefringence – A Case Study of Precision Measurement of Cavity Fringes

We will present an example of measurement of optical phase anisotropy across the mirror surface as a useful illustration of the powerful potential of cavity-based precision measurement. Basically by incorporating mirrors of interest as part of an optical cavity, one can expect an immediate precision-enhancement factor similar to the cavity finesse. Shot noise limited determination of the cavity resonance frequency with orthogonal polarizations can potentially resolve birefringence effects another factor 1 million smaller, limited by one's ability to split the cavity linewidth. Such measurement capability will open up interesting measurements regarding intrinsic mirror properties and their modification by light beams: the Cotton–Mouton effect in various gases [87], the influence of parity-nonconserving effects in chiral molecules, and an interesting test of QED based on magnetically induced birefringence of the vacuum, the so-called "light-by-light" scattering Feynman diagram [30,31,88,89]. With the intracavity light beam of a high-finesse cavity threaded through a string

of strong dipole magnets, the shot-noise limited measurement sensitivity of the cavity resonance would allow detection (and measurement!) of the predicted Δn (birefringence) due to QED vacuum polarization (1.4×10^{-22}). Furthermore, such an experiment would allow a search for light scalar and pseudoscalar particles (such as the axion), which can couple by a two-photon vertex. The limit for the axion – two photon coupling constant measured by this technique should be comparable to the bound set from astrophysical arguments.

We begin with a discussion of the operationally determined interferometric properties of high-grade mirrors; all such "gyro-quality" mirrors are observed to have a different reflection phase-shift (or effective plane of reflection) depending upon the state of polarization of the incident light. Perhaps during polishing some microscopic stress-fields were written into the substrate and not fully erased by the randomizing process of the slow spindle rotation. Perhaps during the coating process the flying molecules were incident at some inclined angle to the surface, leading to some small level of preferred-direction effects in the coating's otherwise glassy, isotropic and nearly structureless coated layers. In any event, it is a fact of experience that all mirrors tested show some level of birefringent behavior that can be as small as 0.1 μrad differential phase shift per bounce. Indeed, it is extremely difficult to robustly mount fused silica mirrors without inducing stress-related birefringence. A cavity formed with birefringent mirrors will accumulate the differential phase shift incurred per mirror bounce and magnify it by a factor of $2F/\pi$ at the cavity transmission. This mirror-related cavity birefringence presents an adversity to many high precision measurements using a high finesse cavity. For example, in the measurement of parity nonconservation in Cs atoms, a small systematic error is introduced when the two counter-propagating waves inside the cavity have slightly different polarizations, which results from the existence of cavity birefringence [90]. In the experiments of optical cavity QED, cavity birefringence prevents the full realization of strong coupling between a closed (cycling) atomic transition and the cavity mode [11]. However, one could also take advantage of this intrinsic birefringence to boost the useful signal level. With an appropriate polarimetric setup, this DC bias can be gainfully employed to convert a quadratic signal of interest to a linear one, with a scaling factor equal to the magnitude of cavity birefringence [91]. Accurately measuring the mirror birefringence could also lead to useful information on surface science. As to scale, a reasonable contemporary "gyro-quality" mirror may show $\sim 10^{-6}$ waves of phase difference at normal incidence for light polarized in two perpendicular linear polarizations. Exceptional mirrors may be three- or even ten-fold less. Note that the high S/N enabled by

a cavity configuration (splitting of linewidth) offers us access to another factor of $\sim 10^7$ in terms of sensitivity enhancement.

How can we measure these subtle optical phase shifts precisely? Ideally we will be able to measure them accurately enough so that two measurements taken with some time separation can be found to agree at the level of precision demanded by our applications. But first, operationally, how can we measure the effect accurately? What are the possible tools? It is instantly clear from the numbers quoted above that it is only with frequency-based metrology that we can hope to have the accuracy necessary to deal with an effect that can range from ~ 1 wave (one cavity fringe) to $\sim 10^{-13}$ waves $(10^{-6} \times 10^{-7})$ as the dynamic range. The ability of the two polarizations to coexist between the cavity mirrors and then be separated externally with a polarizing prism is very useful since it enables measurement of the birefringent effects differentially between the two polarization modes. If we have a minor amount of residual mirror axial motion (very small relative to the laser wavelength), there will be a tremendous reduction of its consequences because of the "common-mode" nature of this excursion as viewed by the spatially coincident but orthogonally polarized beams. This is exactly the difference between this approach and the gravitational wave experiments such as LIGO that must use the Michelson geometry: In that case the two distant mirrors exist at different spatial locations and the common-mode concept is not present. Only complex and expensive vibration isolation will work to produce the necessary inertial-frame mirrors. By contrast, for our high-finesse birefringence interferometer, the two beams will be spatially overlaid and sample the same mirror surfaces. We need isolation only as good as the fringe-width, while gravitational-wave mirrors need isolation as good as the minimum detectable signal size, a vastly smaller quantity.

In many cases in precision measurement physics it turns out that an equivalent signal/noise performance can be realized in several different ways. For example, in the proposed QED birefringence experiment, two polarization states of light are resonantly interacting with mirrors with small polarization phase shifts. Theoretically one finds that good performance and sensitivity can be obtained by measuring the differences in the apparent transmission when tuned near the high-slope regions around the half-height of the resonance line shape. A simpler method would be to illuminate the cavity with light polarized at $+45^\circ$ to the birefringence axes, and analyze the transmitted light with a crossed polarizer [92,93]. Another technique is to add some external ellipticity modulation to the beam in order to linearize the signal again via cross-product [94]. Because of the cavity resonance effect, a very small birefringence will detune the two cavity polarization modes by a significant part of a linewidth. A compensating phase-plate in

the exit beam can delay the faster component so that the dark fringe condition can be re-established in the polarizer-transmitted light. The birefringence is then the measured phase divided by the cavity finesse F. One sees an inconvenience for this method: What happens if our birefringent phase shift is larger than π/F. Now we cannot excite both modes of the cavity simultaneously, so a lower finesse – broader cavity resonance – must be used.

However, it is clear we prefer to use a very high finesse – this directly increases the sensitivity. We want to use a frequency-based scheme to provide the large dynamic range. For laser-cavity locking, one also prefers to use some appropriate modulation method so that the desired anti-symmetric resonance curve is produced by synchronous detection at the central tuning condition. A particularly attractive modulation/detection scheme dubbed the Pound-Drever-Hall technique [77] produces this ''discriminator'' line shape using laser light reflected from the cavity. It is desirable to use a modulation frequency well above the cavity resonance width so that the modulation sidebands are non-resonant, and are therefore essentially reflected from the cavity input mirror. Upon being steered to the detector, these two optical frequencies form the ''local oscillator'' for heterodyne detection of the resonant electric field at the carrier frequency. For the birefringence measurement, there actually are two optical carriers, of crossed polarizations, which are presented to the cavity. They are near or at resonance, leading to strong resonant power buildup inside and to a resulting phase shift of the reflected light that is related to the detuning. Some of these two internal fields leak out, returning to the detector along with the sidebands that were directly reflected as noted before. In this way one can generate the two desired polarization-separated discriminator signals. These detector voltages could be digitized and analyzed for the subtle detuning difference between the two polarization modes, as brought about by the mirror birefringence. For small signals, this would work well. But we need a seven-decade dynamic range to cover the range between the shot noise level and the full signal of one fringe width, and another six or so decades to deal with larger fractional signals where the equivalent birefringence is approaching one wavelength. To deal with such an extreme dynamic range, clearly a possible better choice is to lock two tunable coherent optical sources onto these cavity resonances, one in each polarization, and heterodyne their outputs to recover our signal as a frequency to be counted by a contemporary frequency counter, capable of offering, for example, 12 digits resolution and accuracy in 1 second. Another feasible approach would be to use digitally synthesized frequency sources that can offer a sine-wave output up to tens of megahertz and can be programmed in steps

as small as 1 μHz. Thus this frequency synthesis approach also offers the $>10^{12}$ dynamic range.

Consider the following reasonable laboratory case of a 1 m-long cavity with $F=10^5$, working at a wavelength near 0.5 μm. The fringe order numbers are $\sim 2\times 10^6$, and a change by unity results in the corresponding frequency change of one *FSR*, which is 150 MHz. This *FSR* is the optical frequency difference we would have if the birefringence were 1/2 wavelength (one fringe). The fringe width is $FSR/F=1.5$ kHz. For ~1 mW detected power, the shot noise-determined S/N is $\sim 6\times 10^4$ in a typical 100 kHz control bandwidth, leading to frequency excursions of $\Delta=25$ mHz rms. The equivalent noise spectral density is $\sqrt{S_\nu}=\Delta/\sqrt{B}=80\,\mu\text{Hz}/\sqrt{\text{Hz}}$. Since the modulations at the fast Fourier frequencies accumulate little optical phase, one can expect that the Lorentzian linewidth of the stabilized laser under these ideal conditions would be $\delta\nu_L=\pi\cdot\left(\sqrt{S_\nu}\right)^2=\pi\cdot S_\nu=0.02\,\mu$Hz [95]. In principle we can lock the laser this accurately to the cavity fringes. The shot noise-limited equivalent birefringence for a 1 s measurement would be $\sqrt{2}\sqrt{S_\nu}/\sqrt{2\pi\tau}=45\,\mu$Hz. (The $\sqrt{2}$ comes from subtracting two somewhat noisy values to obtain the birefringence.) This 45 μHz sensitivity is to be compared to the 150 MHz that corresponds to the *FSR* (i.e., a phase change of π), giving an ideal sensitivity of 3×10^{-13} of a fringe in 1 s, or equivalently 1×10^{-13} radians. The cavity resonance linewidth can be split by a fraction of $45\,\mu\text{Hz}/1.5\,\text{kHz}=3\times 10^{-8}$. Of course, the ultimate resolution limit of the minimum-detectable birefringence changes can be as small as $\sqrt{2}\times 20$ nHz ≈ 28 nHz, provided that the experimental integration time can be extended until the discussion of the coherent laser linewidth becomes meaningful and can be gainfully employed for the measurement process. Of course, given the linewidth of 20 nHz, this integration process may not seem practical. In terms of a differential index of refraction sensitivity, if the entire cavity were filled with some gas with magnetically induced birefringence (the Cotton–Mouton effect) for example, this rather straightforward approach would bring us in a 1 s averaging time a birefringent index of refraction sensitivity of 5×10^{-23}. Here we have used the relation $\Delta n/n=\Delta\text{f}/\text{f}$. This shows the powerful potential of a cavity-based frequency measurement approach.

B. Mirror Dispersions, Cavity Mode Spacing, and Cavity-Based Frequency References

In addition to discussions presented in the previous section, precise measurement of reflective mirror phase shifts is instrumental for accurate determination of wavelengths [96,97]. This has not only played an important

role in length metrology, but has also served as an attractive route for the determination of optical frequencies in the visible region since the speed of light is now a defined quantity. Of course the second scenario has changed dramatically since the recent introduction of femtosecond laser comb for direct absolute optical frequency measurement. There has also been extensive research of using the cavity resonant modes to serve as a bridge between RF/microwave frequencies (represented by *FSR*) and the optical frequencies in the visible [85,98,99]. For this approach to work effectively, it is important that the cavity mode spacing (*FSR*) is examined and characterized at a high precision. Considering the inevitable dispersion associated with mirror coatings (especially for the low loss dielectric coatings), the cavity *FSR* is expected to vary with wavelength.

DeVoe *et al*. reported the first detailed and precise measurement of the wavelength-dependent variation of cavity *FSR* near the center wavelength of a mirror coating [85]. That work indicates that the cavity *FSR* will generally vary quadratically around the coating center wavelength and the variation can be determined with sub-hertz precision. High cavity finesse and precision splitting of cavity fringes facilitated by FM-sideband-based laser-cavity locking helped to achieve this level of measurement precision. Empirical calibration of the cavity modes allows the cavity to be used effectively for difference frequency measurement in the optical domain without systematic errors associated with theoretical modeling based on Maxwell's equations. However, this difference frequency measurement is incoherent as all information about the relative optical phase is lost. Furthermore, the attempt to perform absolute optical frequency measurement is still hampered by the need to determine the geometry-related diffraction phase shift and the inevitable drift of cavity properties.

The DeVoe work first introduced the two-tone EOM approach for cavity-related frequency measurement, and was thus the inspiration for the NICE-OHMS technique presented earlier. Indeed, NICE-OHMS also provides an attractive approach for measurement of cavity *FSR*. The basic principle has been illustrated in Section IV; here we will concentrate on some operational details. For NICE-OHMS to take full advantage of noise cancellation, it is important that we maintain a perfect match between the cavity *FSR* and the FM sideband frequency. However, since the laser itself is locked on the cavity, the information about the match between the sideband frequency and *FSR* cannot be obtained by simply detecting and demodulating at the sideband frequency in the cavity reflected light, which always yields a null signal. We choose to use an additional FM dither modulation on the sideband frequency itself, along with synchronous detection of this component in the cavity-reflected or transmitted light. To maintain a clean separation between the modulation and control processes, the RF sideband

[21.7.2003–8:32pm] [1–84] [Page No. 47] FIRST PROOFS {Books}4101-Bederson/Pageproofs/3d/4101-Bederson-001.3d (Bederson) Paper: 4101-Bederson-001 Keyword

frequency is synthesized from two signal sources, a stable frequency synthesizer and a tunable frequency voltage-controlled crystal oscillator (VCXO). The sum frequency is band-pass filtered and amplified before it is fed to the corresponding electro-optic modulator. This configuration allows us to separate the modulation process, where an FM dither signal is applied to the frequency synthesizer, from the servo process where the frequency of the VCXO is controlled from the cavity error signal. In doing so we are able to obtain a better modulation quality and also avoid any change of modulation parameters when the VCXO is tuned. This additional dither frequency is low, typically in the range of 10–300 kHz. Phase-sensitive detection is at the dither frequency and allows locking for the maximum transmission of the sideband. This leads to tracking between the sideband frequency and cavity *FSR*. Figure 13 shows the counted (gate time 1 s) frequency record of the VCXO under the locked condition, with the same cavity used for NICEOHMS detection of the C_2HD resonance at 1.064 μm (*FSR* ~ 320 MHz and a finesse of 96,000). After removal of the cavity-associated frequency drift of 5 mHz/s, we have rms noise in the frequency readout about of 40 mHz at 1-s averaging time. We have not achieved shot-noise limited performance in this case with the technical noise arising from the residual amplitude modulation (RAM) associated with the FM sideband generation. The RAM also degrades the long-term stability of this VCXO-*FSR* tracking system.

If the desired precision in *FSR* measurement is only moderate, then a short-length cavity offers an efficient alternative for characterizing *FSR* vs. wavelength [14]. As will be discussed in Section VII, the strong coupling

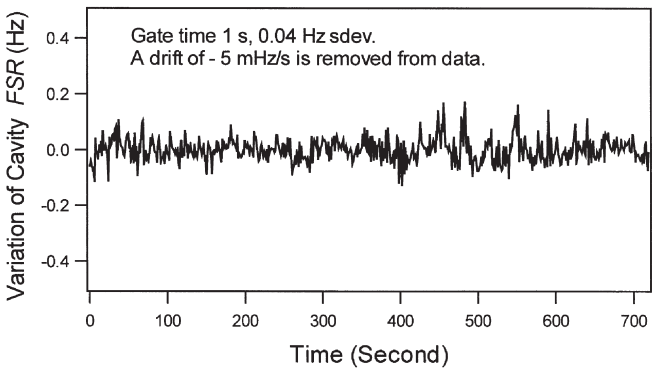

FIG. 13. Measurement of the cavity FSR via the NICE-OHMS technique: matching the FM sideband frequency to the cavity FSR. Counter gate time 1 s. The average value of the counted frequency (FSR) is 319.694953 MHz.

condition for optical cavity QED experiments is achieved by using a small cavity length, of the order of 10 μm for the shortest length reported to date. A 10 μm cavity length translates to a *FSR* of ~15 THz, or a wavelength difference of a few tens of nanometers for neighboring cavity modes. Therefore a straightforward 6-digit measurement of the wavelengths of the cavity modes (by a commercial wavelength meter) acquires a precision of the order of 5×10^{-5} for accurate determination of the equivalent optical length of the cavity, from which details of the index of refraction and layer thickness of materials in the mirror stack can be adequately inferred.

The cavity finesse and overall cavity transmission can be measured directly to determine the mirror losses, A, and transmission, T. This information can be combined with the *FSR* measurement in two useful ways: Firstly, the *FSR* measurement is sensitive to the difference in refractive index ($n_H - n_L$) of the two alternating materials making up the multilayer mirror stack [85], whereas the transmission T depends on the ratio n_H/n_L. As a result, a precise measurement of both the *FSR* and T can be used to determine the values of n_H and n_L independently. Moreover, by mapping out the wavelength dependence of the *FSR*, the thickness of layers in the mirror stack can be determined. Figure 14 shows

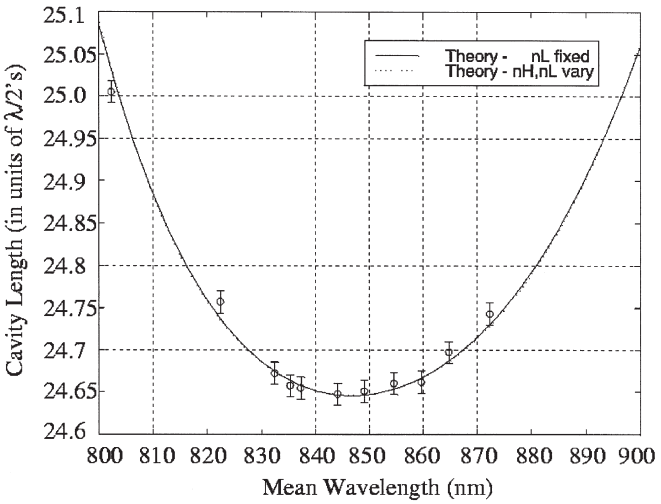

FIG. 14. The effective cavity length measured from the cavity mode splitting frequency (FSR) has a quadratic variation around the designed wavelength center of the coating. Fitting a model to these data points gives a measure of mirror transmission (from fitting of the difference $n_H - n_L$) and center wavelength (from fitting layer thickness). The measurement was made on a 10 μm long cavity with a finesse of ~500,000.

the variation of the cavity *FSR* with respect to wavelength. The measurement is carried out with high ($\sim$half a million) finesse mirrors forming a 10 μm scale cavity used for cavity QED experiments presented later in Section VII. Secondly, if one of the refractive indices is well known, then the *FSR* measurement determines the other one, and an independent value for the mirror transmission T can then be calculated from n_H and n_L and compared to the experimentally measured result. Indeed, it is often useful to make complementary and mutually confirming measurements of the cavity properties by the two approaches, i.e., measurements of the direct cavity loss and the dispersion of the cavity modes. It is worth noting that the mirror phase shift (*FSR* measurement) is only sensitive to the transmission (index contrast) and center wavelength (layer thickness). Therefore, if absorption/scatter losses are added to the model (by introducing an imaginary component to the refractive index) the cavity resonance wavelengths do not change.

Clearly, the wavelength-dependent phase shift due to the mirror coating, i.e., the mirror dispersion, makes it impossible to use the *FSR* of an empty cavity as a constant frequency marker. However, one can introduce an active (or passive) modulation element inside the cavity that actively "mode-locks" different cavity modes together to produce a regularly spaced optical frequency comb. One of the most effective approaches to optical difference frequency measurement across a few-terahertz gap is EOM-based optical frequency comb generation, in which an RF electro-optic modulator (EOM) is placed inside a low-loss optical cavity [100,101]. The cavity *FSR* matches with the RF sideband frequency. The optical cavity enhances modulation efficiency by resonating with the seeding optical carrier and all subsequently generated sidebands, leading to a spectral comb of frequency-calibrated lines spanning a few THz. The schematic of such an optical frequency comb generation process is shown in Fig. 15. The single frequency cw laser is locked on one of the resonance modes of the EOM cavity, with the *FSR* of the loaded cavity being an integer multiple of the EOM modulation frequency. The cavity output produces a comb spectrum with an intensity profile of $\exp\{-|k|\pi/\beta F\}$, where k is the order of generated sideband from the original carrier, β is the EOM frequency modulation index, and F is the loaded cavity finesse [100]. The uniformity of the comb frequency spacing was carefully verified [102]. These optical frequency comb generators (OFCG) have produced spectra extending a few tens of THz [103], nearly 10% of the optical carrier frequency. Some unique OFCG configurations have been developed at JILA. For example, by using an auxiliary cavity as a resonant output-coupling element, one can select a single comb line in the cavity output [104]. Another scheme uses a single crystal ($LiNbO_3$) to perform

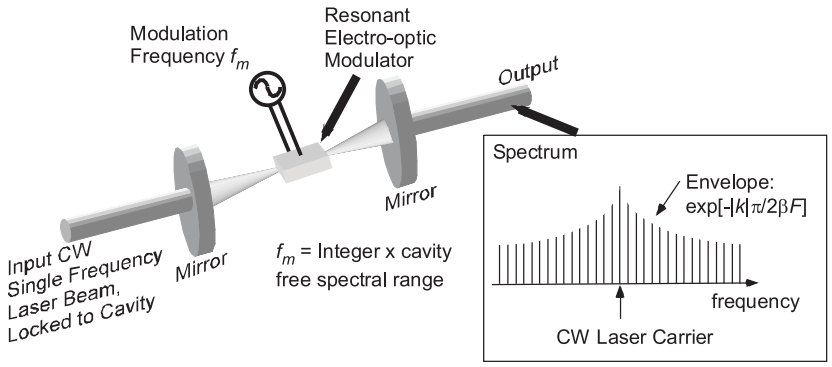

FIG. 15. Schematic of optical frequency comb generator (OFCG) based on an intracavity electro-optic modulator. OFCG converts a single optical frequency (cw) at the cavity input to a comb spectrum (pulse) at the cavity output. A high finesse (typically a few hundreds) of the loaded cavity and a high FM modulation index (β) are instrumental to a broad bandwidth of the generated comb (typically a few THz).

both functions as an EO modulator and as an Optical Parametric Oscillator, leading to an effective intracavity gain within desired frequency ranges to enhance the sideband generation efficiency [105].

OFCGs had an immediate impact on the field of optical frequency measurement. Kourogi and co-workers produced an optical frequency map (accurate to 10^{-9}) in the telecommunication band near 1.5 μm, using an OFCG that produced a 2-THz wide comb in that wavelength region, connecting various molecular overtone transition bands of C_2H_2 and HCN [33]. The absolute frequency of the Cs D_2 transition at 852 nm was measured against the fourth harmonic of the HeNe/CH_4 standard, with an OFCG bridging the remaining frequency gap of 1.78 THz [106]. At JILA, we used an OFCG to measure the absolute optical frequency of the iodine stabilized Nd:YAG frequency near 532 nm [69]. The results obtained using OFCGs made the advantages of larger bandwidth very clear. However the bandwidth achievable by a simple EOM-based OFCG is limited by cavity dispersion and modulation efficiency. To achieve even larger bandwidth, mode-locked lasers became a natural choice, thus triggering a true revolution in optical frequency measurement [80,107]. We note in passing that the OFCGs described above actually generate a train of short pulses from a cw laser input. This is simply due to interference among modes with a fixed phase relationship. Indeed the first OFCG was built to generate short optical pulses [108] rather than for optical frequency synthesis or metrology. Later work provided even shorter pulses from an OFCG [109].

C. Femtosecond Laser Optical Frequency Comb and its Interaction with a Cavity

A laser that can sustain simultaneous oscillation on multiple longitudinal modes can emit short pulses; it just requires a mechanism to lock the phases of all the modes, which occurs automatically in an OFCG due to the action of the EOM. Lasers that include such a mechanism are referred to as "mode-locked" (ML). While the term "mode-locking" comes from this frequency domain description, the actual processes that cause mode-locking are typically described in the time domain. The inclusion of gain [105,110] and dispersion compensation [111] in OFCGs brings them even closer to ML lasers. Indeed the use of ML lasers as optical comb generators has been developed in parallel with OFCG, starting with the realization that a regularly spaced train of pulses could excite narrow resonances because of the correspondence with a comb in the frequency domain [112–115]. Attention was quickly focused on ML lasers as the source of a train of short pulses [116–119]. In addition, the mode-locked lasers tend to be "self adjusting" in the sense that they do not require the active matching between cavity length and modulator frequency that an OFCG does. The recent explosion of measurements based on ML lasers [107,120–122] has been largely due to development of the Kerr-lens-mode-locked (KLM) Ti:sapphire laser [123–125] and its ability to generate pulses so short that the spectral width approaches an optical octave. Many recent results have obtained a spectral width exceeding an octave by spectral broadening external to the laser cavity [126].

To understand the connection between the ultra-stable world of optical frequency metrology and the ultra-fast world of ML lasers, we begin by comparing the unique characters of each field. The ultra-stable field is typified by high-resolution spectroscopy and high-precision measurements based on cw lasers that can be best described by their near delta-function frequency spectra. In sharp contrast, the field of ultra-fast phenomena encompasses the study of sub-picosecond events utilizing laser pulses that approach the limit of time domain delta-functions. In fact, at this point in time state-of-the-art laser sources from these two fields share nearly the same delta-function "figure of merit" with frequency and temporal widths on the order of a few parts in 10^{15} Hz and seconds, respectively. The connection between the ultra-stable and the ultra-fast arises from the fact that femtosecond (fs) laser oscillators produce pulses in a periodic train via mode-locking, with a corresponding rigorous periodicity in the spectral domain. In fact, the frequency domain spectrum consists of a comb of discrete modes separated by the repetition frequency $f_{\text{rep}} = 1/\tau_{\text{r.t}}$, where $\tau_{\text{r.t.}}$ is the cavity round trip time. The extent of the time domain pulse train

provides the frequency resolution of individual comb components, while the total extent of the frequency domain mode comb is approximately limited to the inverse of the pulse duration. The generation of ultrashort pulses requires that the group velocity (v_g) dispersion inside the laser cavity be minimized across the pulse's frequency spectrum [127]. This criterion is not directly related to the frequency comb spacing, since the individual mode frequencies correspond to eigenmodes of the phase-velocity (v_p) of the light. In general, we have $v_g \neq v_p$ due to laser cavity dispersion. This fact results in a pulse envelope function that is not fixed with respect to the underlying optical oscillation frequencies – there is a phase slip between the "carrier" phase and the envelope peak for each of the successive pulses emitted by the laser [120,128].

The concept of carrier-envelope phase is based on the decomposition of the pulses into an envelope function, $\hat{E}(t)$, that is superimposed on a continuous carrier wave with frequency ω_c, so that the electric field of the pulse is written $E(t) = \hat{E}(t)e^{i\omega_c t}$. The carrier-envelope phase, ϕ_{ce}, is the phase shift between the peak of the envelope and the closest peak of the carrier wave, as illustrated in Fig. 16(a). In any dispersive material, the difference between group and phase velocities will cause ϕ_{ce} to evolve. And the pulse-to-pulse carrier-envelope phase slip is denoted as $\Delta\phi$ as shown in Fig. 16(a). In the frequency domain, $\Delta\phi$ yields an offset of the mode comb from exact harmonics of the f_{rep} by the amount $f_{ceo} = \Delta\phi\ f_{rep}/2\pi$ Hence each optical comb frequency is effectively given by $f_n = nf_{rep} + f_{ceo}$, as shown in Fig. 16(b). Here n represents an integer ($\sim$1 million depending up the ratio of the optical frequency and f_{rep}) harmonic number of the optical comb line. One sees that the frequency-domain control of both f_{rep} and f_{ceo} makes it possible to establish a ML-laser based optical comb at a high precision for absolute optical frequency measurement and distribution. Precision control of the time-domain carrier-envelope phase, which has been a highly desirable and yet elusive goal in ultrafast science since the advent of few-cycle pulses, also becomes a reality [129,130]. Control of $\Delta\phi$ requires maintaining a stable ratio between f_{ceo} and f_{rep}. It is straightforward to measure f_{ceo} when the bandwidth of the frequency comb spans an optical octave, which can be facilitated by spectral broadening outside a ML-laser cavity. Basically we measure the heterodyne beat between comb lines on the high frequency extreme of the spectrum and the second harmonic of the corresponding comb lines at the low frequency end of the spectrum. The resulting beat frequency is $|f_{2n} - 2f_n| = \left|(f_{ceo} + 2nf_{rep}) - 2(f_{ceo} + nf_{rep})\right| = f_{ceo}$.

An optical cavity can also be used to control the two degrees of freedom associated with a ML-laser comb [82,131]. Appropriate servo error signals can be obtained if one compares the f_{rep} of the comb against the cavity *FSR*, while the average frequency of a selected collection of comb lines

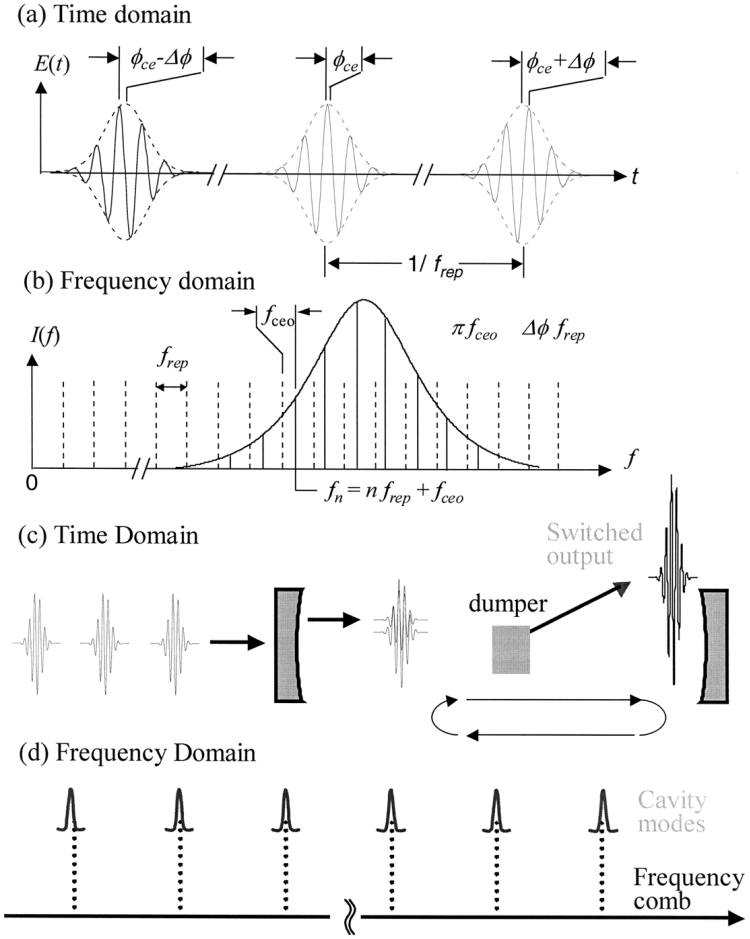

FIG. 16. Time-frequency correspondence between $\Delta\phi$ and f_{ceo}. (a) In the time domain, the relative phase between the carrier (solid) and the envelope (dotted) evolves from pulse to pulse by the amount $\Delta\phi$. ϕ_{ce} is an unknown overall constant phase. (b) In the frequency domain, the elements of the frequency comb of a mode-locked pulse train are spaced by f_{rep}. The entire comb (solid) is offset from integer multiples (dotted) of f_{rep} by an offset frequency $f_{ceo} = \Delta\phi f_{rep}/2\pi$. Without active stabilization, f_{ceo} is a dynamic quantity, which is sensitive to perturbation of the laser. Hence $\Delta\phi$ changes in a nondeterministic manner from pulse to pulse in an unstabilized laser. (c) Principle of coherent pulse amplification scheme with the aid of an optical cavity with the time domain picture showing matching of the pulse repetition period with the cavity round trip time. The intracavity pulse is switched out when sufficient energy is built up in the cavity. Intracavity dispersion compensation is not shown. (d) Frequency domain illustration showing the matching of the pulse comb structure with corresponding cavity modes. This ensures the efficient coupling of pulse energy into the cavity.

is compared against the center frequencies of the corresponding cavity modes. Just as for the CW laser case, an optical cavity can provide large S/N ratios for the respective servo error signals that would permit superb short-term stability of the passive reference cavity to be transferred to the ML laser. Another interesting application is to use a passive optical cavity as a means to temporarily store and coherently enhance the pulsed electric field [86]. By simultaneously controlling the repetition and carrier frequencies, the phase coherent superposition of a collection of successive pulses from a mode-locked laser can be realized inside an optical cavity. Coherent delay and constructive interference of sequential pulses will continue until a cavity dump is enabled to switch out the ''amplified'' pulse. This approach will lead to an effective amplification process through decimation of the original pulse rate while preserving the overall coherence from the oscillator. This will be the subject of the next section.

D. Gainless Amplifier for Ultrafast Pulses Based on Control of Carrier-Envelope Phase

With the recent realization of phase control of femtosecond lasers, its potentially powerful applications in extreme nonlinear optics and novel coherent processes are being actively explored [132]. Ordinarily, the peak power offered by pulses emitted from a simple oscillator is not sufficient to drive the high-order nonlinear processes of interest. Naturally, researchers are interested in the development of phase-controlled pulse amplification [133,134]. However, the use of conventional amplifiers can introduce a great deal of phase noise owing to effects such as beam pointing variation, pump power fluctuation, and amplifier medium instability. A unique approach for pulse amplification without the use of an active gain medium is the coherent addition of neighboring pulses inside an optical cavity. The technique relies on coherent superposition of successive components from a pulse train to increase the amplitude of a single pulse while reducing the repetition frequency. This requires not only a suitable delay mechanism to line up successive pulses, but also the ability to control the phase evolution of the electric field underlying the pulse. These requirements are similar to those in work already demonstrated in coherent pulse synthesis from separate femtosecond lasers. In that work, precise control of both timing synchronization and carrier phase locking was achieved to successfully synthesize a single pulse from two independent pulses. An amplification scheme based on coherent addition would maintain the carrier-envelope phase coherence of the original oscillator.

[21.7.2003–8:32pm] [1–84] [Page No. 55] FIRST PROOFS {Books}4101-Bederson/Pageproofs/3d/4101-Bederson-001.3d (Bederson) Paper: 4101-Bederson-001 Keyword

The operation principle of the proposed "amplifier" design is illustrated in Fig. 16, with time domain action depicted in part (c) and the frequency domain correspondence in part (d). To ensure efficient coupling into the cavity and subsequent power buildup, the repetition rate and carrier-envelope phase of the input pulses must match that of the pulse circulating inside the passive cavity. The equivalent frequency domain requirement is that all frequency components making up the pulse train are tuned into resonance with corresponding cavity modes as depicted in Fig. 16(d). The cavity decay time is directly proportional to the overall cavity finesse and is predetermined to match with the desired pulse amplification factor. For example, suppose a laser pulse train has a 100 MHz repetition rate and we wish to convert it to an output pulse train with a 1 MHz repetition rate with 100 times amplification in the peak power. We would then design the cavity finesse to be $\sim$314 such that the linewidth is 0.32 MHz and the field decay time is roughly 1 μs. This allows the electric fields of roughly 100 pulses to add coherently inside the cavity before being switched out.

Resonant enhancement cavities are commonly used with cw lasers to improve efficiencies in nonlinear optical interactions or to increase sensitivity in spectroscopic applications [135]. Based on these cw techniques, similar intracavity experiments using ML lasers have been demonstrated [136–139]. These approaches, however, address only one parameter (repetition rate or laser average frequency), while both are required for coherent pulse manipulation. Hence coherent superposition of successive short pulses for significant amplification would not be feasible. In order to efficiently couple sub-100 femtosecond (fs) pulses into an optical cavity with a finesse sufficiently high to build up pulse energy by 100 to greater than 1000 times, two key criteria must be met: (i) the carrier *and* repetition frequency of the fs laser must be simultaneously stabilized to those of the cavity, and (ii) the cavity itself must be designed such that dispersion does not severely distort the intracavity pulse.

As discussed in previous sections, inevitable dispersion inside an optical cavity arising from intracavity elements and mirror-reflection phase shifts leads to a nonuniform cavity mode spacing throughout relevant spectral regions. This fact will place a practical limit on the spectral bandwidth (and therefore pulse duration) one can employ in this scheme since the modes of the fs pulse train are rigorously equally spaced. In addition, relevant laser comb components coupled into the cavity cannot be simultaneously locked to the center of corresponding cavity modes, in contrast to the ideal case shown in Fig. 16(d), leading to a frequency dependent phase shift imposed on the intracavity spectrum and therefore distorting the pulse temporal profile. If higher cavity finesse is desired for greater pulse enhancement, the cavity linewidth will become narrower and the increased mismatch between

[21.7.2003–8:32pm] [1–84] [Page No. 56] FIRST PROOFS {Books}4101-Bederson/Pageproofs/3d/4101-Bederson-001.3d (Bederson) Paper: 4101-Bederson-001 Keyword

the cavity modes and the fs comb will lead to a further reduction in the useful bandwidth of the cavity. These facts can also be easily understood from time domain considerations where pulses bouncing back and forth in the cavity are broadened and distorted due to dispersive phase shifts. As a result, the overlap of the incoming pulse envelopes with the stored pulse is reduced and their constructive interference is compromised.

Let us assume a four-mirror linear cavity with a pair of fused silica prisms for dispersion compensation and an intracavity fused silica Brewster-angled Bragg deflector for switching out the pulse. Two of the mirrors are used to create an intracavity focus to decrease the switching time of the Bragg deflector. It should be noted that in order to reduce intracavity peak powers to avoid substantial nonlinear effects, the input pulse may be chirped and later recompressed as is commonly practiced in traditional optical amplifiers. This operation would have no effect on the results shown here. The input mirror should have a transmission coefficient matched to the remaining part of the total cavity loss (impedance matching). The maximum finesse, and hence maximum pulse magnification, will then be limited by scattering losses in the fused silica, residual losses at the Brewster angled surfaces, and reflection loss at the remaining cavity mirrors. We expect a cavity finesse of greater than 1000 will be experimentally feasible.

The round trip phase shift inside the cavity can be expressed in a power series expansion: $\Phi_{RT}(\omega) = \Phi_0 + \Phi_1(\omega - \omega_0) + \Phi_2(\omega - \omega_0)^2/2! + \Phi_3(\omega - \omega_0)^3/3! + \cdots$, where ω_0 is the center angular frequency of the mirror coating. The frequency independent phase shift Φ_0 describes the carrier-envelope phase shift per round trip of the intracavity pulse while the group delay Φ_1 determines the cavity free-spectral range (FSR) at ω_0. These terms are not important to the evaluations as the pulse train incident on the cavity will be matched to these values when properly stabilized. The group-delay dispersion will be set to zero at ω_0 with prism compensation. The phase shifts due to reflection from the dielectric mirrors depend strongly on the coating design. For the calculations we have chosen to use standard quarter-wave stack mirrors for which dispersion characteristics are well known, although better performance may be achieved using mirrors custom designed for dispersion compensation. A total path length of 0.9 cm through the fused silica components was assumed with a 30 cm separation between the prisms. The dispersion coefficients used for the given cavity parameters are $\Phi_2 = 0$, $\Phi_3 = 400\,\text{fs}^3$, and $\Phi_4 = -1060\,\text{fs}^4$.

A time dependent calculation visualizes the evolving intracavity pulse one round-trip at a time. The calculation is performed in a straightforward manner by repeatedly solving for the transmitted and reflected fields at the input mirror after propagating the pulse once through the cavity. Figure 17 illustrates the evolution of a 50 fs pulse inside a cavity with a finesse of

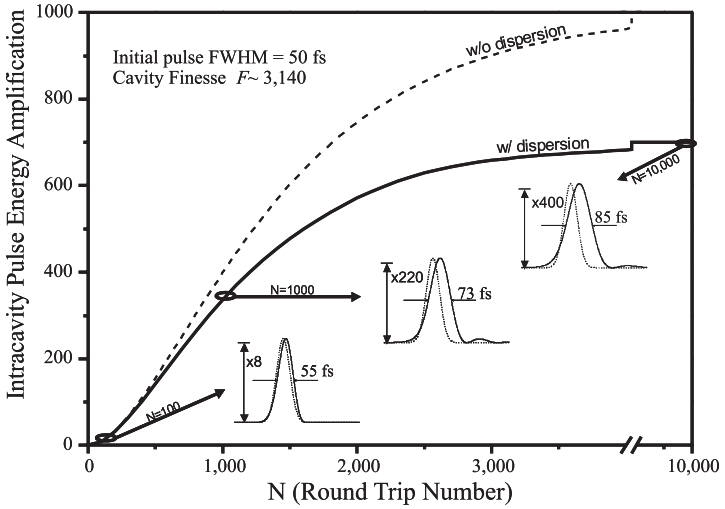

FIG. 17. Time dependent calculation of the intracavity pulse propagation shows the coherent evolution of a 50 fs pulse inside a cavity of finesse 3140. Dashed line indicates the ideal case of a dispersion free cavity perfectly matched with the incident pulse train, while the solid line shows the effect of cavity dispersion in limiting the amount of energy coupled into the cavity. Three representative pulses at different stages of "amplification" are also shown.

3140 under the conditions of zero cavity dispersion (dashed curve) and finite dispersion (solid curve). Three representative pulses at different stages of "amplification" are also shown. Although the 50 fs pulse is stretched by the dispersive cavity, it is not severely distorted due to its coupling with the incident pulse train. If the incident pulses become too short, the cavity finesse becomes too high, or the laser repetition frequency deviates significantly from the cavity *FSR* at ω_0, the intra-cavity pulse may quickly "pull apart" into several pulses, and the meaning of a single pulse width will be lost.

The results shown here demonstrate the feasibility of a pulse amplification scheme based on coherent storage and constructive interference of pulsed electric fields inside a passive optical cavity. Such a technique will preserve the carrier-envelope phase coherence characteristics of the original pulses from the oscillator while enabling pulse energies to be increased by 2 or 3 orders of magnitude. This indicates that sub-100 fs pulses with microjoule energies can be obtained given the nanojoule level of pulse energy available from current ultrafast lasers. Future cavity designs based on custom dispersion compensating mirrors may extend the usefulness of this technique to the sub-20 fs regime. Initial experimental exploration with a picosecond

laser has already produced an amplification factor of greater than 50 without any noticeable pulse distortion, using a loaded cavity finesse of ~ 200.

VII. Quantum Dynamics

The last two decades have witnessed the emergence of a qualitatively new set of phenomena in the physics of optical cavities: light-matter interactions that derive their character explicitly from the quantized nature of individual atoms and light fields. Such interactions are manifest in the current generation of cavity QED experiments thanks to a steady progression of developments in both atomic and optical physics. Technical improvements have allowed optical cavities with ever higher finesse and smaller mode volumes; as we shall see, these are the requirements for coherent dynamics to dominate the interaction of single quanta in the cavity setting. On the other hand, techniques in atomic physics and laser cooling have provided the means to deliver into these small cavity mode volumes single atoms with appropriately chosen internal states and nonlinear response functions. Today, these capabilities combine to allow experimental exploration of quantum state estimation and control, including progress toward quantum logic and quantum communication using optical cavities. The signal enhancement effects that make optical cavities so suitable for classical spectroscopy find their analogs in the quantum regime, making cavity QED a powerful tool for probing the physics of open quantum systems.

A. Connection and Difference Between Classical and Quantum Regimes

In a classical description of spectroscopy in an optical cavity, an atomic sample acts as a dispersive medium for the coherent light field circulating in the cavity mode volume. Classical behavior gives way to quantum when single quanta, whether of the atomic sample or of the light field itself, begin to induce nonlinear response in the system. Some critical parameters delineating this transition have already been briefly introduced. We expand that intuitive discussion here and complement it with a more quantitative development in the following sections.

Consider an atomic sample placed inside the cavity mode. The sample scatters the optical field, producing a wavelength-dependent refractive index in the cavity mode volume. The atomic sample affects the resonance properties of the optical cavity if the atom-field interaction strength and the

number of atoms are sufficient to noticeably alter the free-space dispersion relation for the light. Thus, if a single atom placed within the mode volume is to act as a nonlinear medium, it must have a large effective cross-section for scattering intracavity light. First, the atom should have a near-resonant dipole interaction with the optical field mode supported by the cavity. Second, scattering should be enhanced by ensuring that optical wavefronts have every opportunity to interact with the atom in the process of being transmitted through the cavity. This second requirement is accomplished by constructing cavities with high finesse and tightly confined modes, so that light traverses the distance between the mirrors many times before exiting the cavity and furthermore has a high chance of interacting with the atomic cross-section on each pass. Tight mode confinement has the additional benefit that the light is thoroughly diffractively mixed and thus the interaction is truly with a single cavity mode that is well-defined throughout the interaction process. Quantitatively, the importance of a single atom for the response of the intracavity field is described by the single-atom cooperativity parameter $C_1 = g_0^2/2\gamma_\perp\kappa$, or by its inverse, the critical atom number, $N_0 = 2\gamma_\perp\kappa/g_0^2$ [51]. Here g_0, $\gamma_\perp$, and κ are as introduced in Section III.D. By re-expressing the single-atom cooperativity in terms of familiar properties of the cavity and the atomic transition, one finds it scales simply as $C_1 \sim 2F\lambda\ \Pi w_0^2$; the ratio λ^2/w_0^2 can be interpreted as the ratio of atomic absorption cross-section to cross-sectional area of the cavity mode, and $2F/\pi$ is the cavity enhancement factor we have already seen in the classical context. Note that C_1 does not scale explicitly with the length of a Fabry-Perot cavity.

On the other side of the coin, consider the circumstances necessary to make the quantized nature of the light field relevant to observations of the cavity system. In the classical regime the cavity mode volume is occupied by a large-amplitude coherent field. To fully probe the atomic response function, the electric field associated with the light must be strong enough to saturate the atomic dipole. How, then, is a single photon to accomplish this saturation? Simply put, the photon must be confined to a small volume so its electric field strength within that volume becomes large. A field of Rabi frequency Ω saturates an atomic transition when $\Omega \sim \gamma$. Since the Rabi frequency is proportional to the electric field and thus to the square root of photon number, the m-photon Rabi frequency is just $\sqrt{m}g_0$. Therefore we can define a saturation photon number $m_0 = \gamma_\perp^2/2g_0^2$ [51] representing the number of intracavity photons required to saturate the atom. As promised, this quantity is inversely proportional to the cavity mode volume through the factor $1/g_0^2$; it is, however, completely independent of the cavity finesse.

We now turn to a more formal treatment of the atom-cavity system. As is often the case, the conceptually and computationally simplest starting point

[21.7.2003–8:32pm] [1–84] [Page No. 60] FIRST PROOFS {Books}4101-Bederson/Pageproofs/3d/4101-Bederson-001.3d (Bederson) Paper: 4101-Bederson-001 Keyword

is the purely quantum limit, where the atom and cavity evolve via their coherent coupling in the absence of dissipation. This system simply obeys the Schrodinger equation with the Jaynes-Cummings Hamiltonian [48],

$$H_{JC} = \hbar\omega\hat{a}^{+}\hat{a} + \hbar\omega\hat{\sigma}^{+}\hat{\sigma} + \hbar g_0(\hat{a}\hat{\sigma}^{+} + \hat{a}^{+}\hat{\sigma}). \tag{25}$$

Here we consider a two-level atom and ω is the common resonance frequency of both atom and cavity. Diagonalizing this Hamiltonian gives rise to the well-known Jaynes-Cummings ladder of eigenstates for the coupled atom-cavity system, as illustrated in Fig. 18. The coupled eigenstates are characterized by the equal sharing of excitation between the atomic dipole and cavity field, so that the n-excitation bare states $|g, n\rangle$ and $|e, n-1\rangle$ of energy $n\hbar\omega$ are replaced by

$$|\pm_n\rangle = \frac{1}{\sqrt{2}}\big(|g, n\rangle \pm |e, n-1\rangle\big), \tag{26}$$

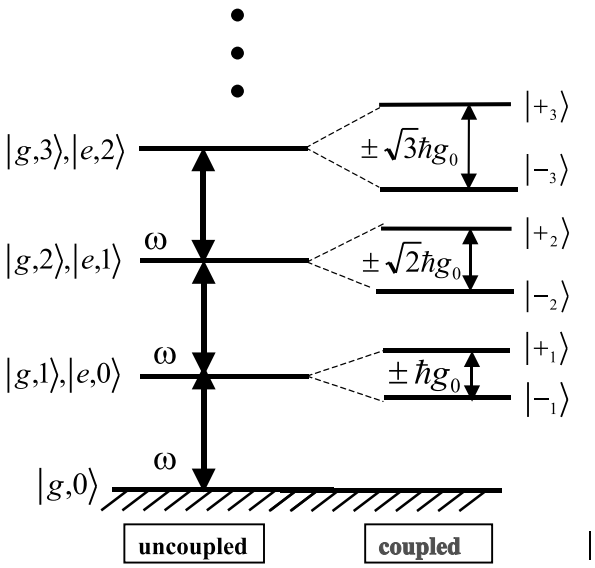

FIG. 18. Jaynes-Cummings ladder of eigenstates for the coupled atom-cavity system. Bare eigenstates of the atom and cavity field are shown on the left, labeled by atomic internal state and number of photons in the cavity mode, under the condition $\omega_c = \omega_a = \omega$. When the atomic dipole is coupled to the cavity field with single-photon Rabi frequency $2g_0$, the energy eigenstates form the ladder shown on the right. The Jaynes-Cummings ladder has pairs of strong- and weak-field-seeking states with each pair split by an energy that rises as the square root of the number of excitations.

with corresponding energy eigenvalues

$$E_{\pm_n} = n\hbar\omega \pm \sqrt{n}\hbar g_0. \tag{27}$$

To quantitatively predict actual atom-cavity dynamics, a treatment that moves beyond this idealized picture to include dissipation and driving terms will be necessary. Two qualitative features, however, are worth noting immediately from the Jaynes–Cummings ladder itself.

First, in the most fully quantum regime, the atom and cavity field are best described in a symmetric treatment where they combine to create a single entity sharing excitation equally. Most notably, for $n \geq 1$ excitation, there exist strong-field-seeking states $|-_n\rangle$ that can be thought of as atom-cavity states bound together by the sharing of a quantum of excitation. If we permit a detuning Δ_{ac} between the atom and cavity resonance frequencies, the sharing of excitation in these "bound states" becomes asymmetric but the qualitative properties of the ladder remain unchanged.

Second, while a ladder of strong-field- and weak-field-seeking states recalls the dressed states of atomic interaction with a coherent light field (e.g., in free space) [140], the Jaynes-Cummings ladder reflects atomic coupling to a small number of quantized excitations in the cavity mode rather than to a strong classical field in free space. The anharmonic nature of the level splittings with increasing n is a feature arising explicitly from the quantized nature of the cavity field. Thus, to observe effects of field quantization on the spectrum of atom-cavity response, we can expect that experiments must probe the saturation behavior of the system and not simply rely on spectroscopy in the weak-driving limit of $n < 1$ system excitations. One caveat to this observation, however, is that nonclassical aspects of the system *dynamics* can in fact be observed for weak driving; for example, photon statistics of the cavity output field in time are of interest even for experiments in the weak-excitation limit.

In the presence of dissipation and driving, and allowing for detuning between the probe field and the atom and cavity resonant frequencies, the Jaynes-Cummings Hamiltonian becomes part of a master equation for the joint atom-cavity density operator ρ. We consider a driving (and probing) field E of frequency ω_p, a cavity resonant at $\omega_c = \omega_p + \Delta_{cp}$, and an atomic resonance frequency $\omega_a = \omega_p + \Delta_{ap}$. In the electric dipole and rotating-wave approximations, the evolution is described by

$$\dot{\rho} = -\frac{i}{\hbar}\left[\hat{H}_0, \rho\right] + \gamma_\perp(2\hat{\sigma}\rho\hat{\sigma}^+ - \hat{\sigma}^+\hat{\sigma}\rho - \rho\hat{\sigma}^+\hat{\sigma}) + \kappa(2\hat{a}\rho\hat{a}^+ - \hat{a}^+\hat{a}\rho - \rho\hat{a}^+\hat{a}),$$
$$\hat{H}_0 = \hbar\Delta_{cp}\hat{a}^+\hat{a} + \hbar\Delta_{ap}\hat{\sigma}^+\hat{\sigma} + \hbar g(\vec{r})\left[\hat{a}\hat{\sigma}^+ + \hat{a}^+\hat{\sigma}\right] + E(\hat{a} + \hat{a}^+). \tag{28}$$

Here $g(\vec{r})$ is the coupling strength which takes into account the atomic position $\vec{r}$ within the cavity mode. For a Fabry-Perot cavity supporting a standing wave mode with Gaussian transverse profile, $g(\vec{r}) = g_0\psi(\vec{r}) = g_0\cos(2\pi x)\exp[-(y^2+z^2)/w_0^2]$. In the fully quantum treatment, the atomic position $\vec{r}$ is itself an operator; in experiments to date a quasiclassical treatment suffices, so the atom may be considered a wavepacket with $\vec{r}$ a classical center-of-mass position variable.

This master equation provides a valid description of the atom-cavity system in any range of parameters $(g_0, \kappa, \gamma_\perp)$. It can in general be solved only numerically, but certain limits, either of inherent rates or of driving strengths, permit analytical treatments of limited application. In the sections below, we discuss behavior exhibited by theory and experiment in several parameter regimes from semiclassical to very strongly coupled.

B. Cavity Bistability and Intracavity Nonlinear Optics

Certain parameter regimes are well described by an approximation in which the joint operator moments in Eq. (26) can be factored. This corresponds to a semiclassical treatment in which the field is described by its coherent amplitude $\langle\hat{a}\rangle = \alpha$. Such a replacement is valid in the limit of large critical parameters $(N_0, m_0) \gg 1$, in which case a collection of atoms acts as a classical nonlinear intracavity medium. Within this approximation, Eq. (26) yields an analytic expression for the driving field $E = \kappa\sqrt{m_0}y$ as a function of the intracavity field $\langle\hat{a}\rangle \leftrightarrow \sqrt{m_0}x$. This relation is the well-known optical bistability state equation [52]:

$$y = x\left[1 + \frac{2C}{1+\delta^2+x^2} + i\left(\phi - \frac{2C\delta}{1+\delta^2+x^2}\right)\right]. \tag{29}$$

Here we have employed the standard notation for the bistability equation, related to our previous discussions by detunings $\delta = \Delta_{ap}/\gamma_\perp$ and $\phi = \Delta_{cp}/\kappa$, and N-atom cooperativity parameter $C = NC_1$. The system saturation behavior described by this relation is shown in the dotted curve of Fig. 19. The correspondence between the semiclassical amplitude x and the actual operator expectation value $\langle\hat{a}\rangle$ is only approximate; in general the intracavity state is not an exact coherent state, but the bistability equation gives an input–output relation between the driving power $\sim y^2$ and a transmitted photocurrent $\sim x^2$ which is valid in the limit discussed above.

Optical bistability effects in general have a long history in measurements within the context of laser physics. Specific cavity QED experiments measuring optical bistability in two-level systems date from the early 1980s

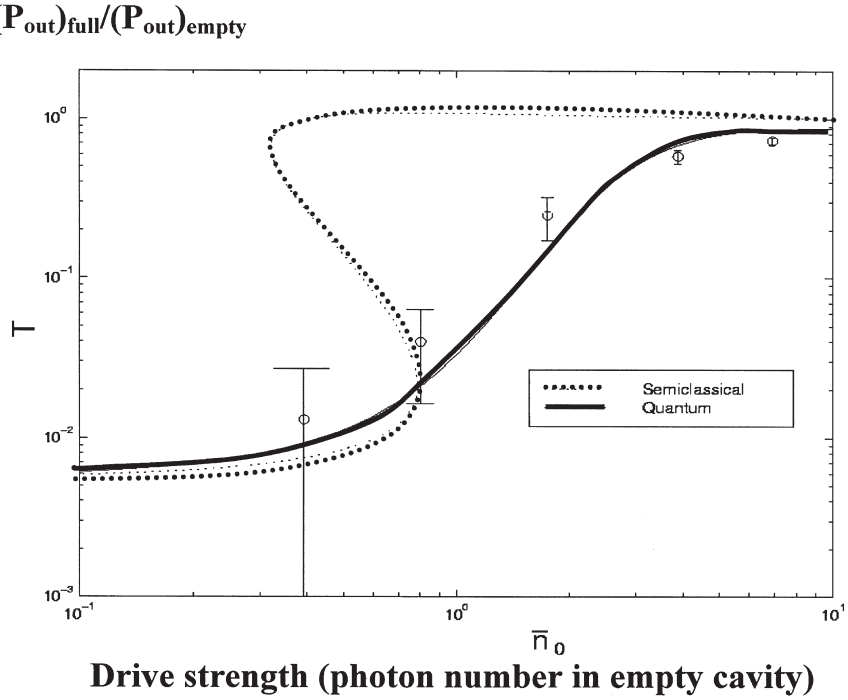

FIG. 19. Saturation curves for the atom-cavity system of [158], based on semiclassical and quantum theory. Here $\omega_c = \omega_a = \omega_p$. The probe strength is varied over a range corresponding to 0.1 to 10 photons in the empty cavity. The system saturation is investigated by recording at each drive strength the ratio of cavity output power for the coupled system as compared with the empty cavity. The dotted curve shows the prediction of the optical bistability state equation (semiclassical theory), while the solid curve shows the solution of the master equation (fully quantum in the field). The semiclassical prediction clearly deviates from the quantum solution and from the data in this strongly coupled system [158].

([141,142]) and are realizable in relatively low-finesse cavities interacting with a sample of atoms crossing the cavity mode in a thermal atomic beam. However, the bistability state equation is also valid when $(N_0, m_0) < 1$ in the special case of very weak driving, $n \gg 1$ excitations in the system. In this case, only the first ($n = 1$) excited states of the system must be considered, and the resulting relationship of joint operator moments makes factoring formally valid. This fact comes as no surprise in the light of our earlier discussion of the Jaynes-Cummings ladder; the structure of the spectrum reflects the quantized field only for higher drive strengths that sample the anharmonicity of the system eigenvalues. Optical bistability also describes

the steady-state behavior of an atom-cavity system where inherent strong coupling is washed out by the simultaneous interaction of many atoms with the cavity mode.

Even in the regime of the optical bistability equation, nonclassical dynamics of the atom-cavity system are accessible. Experiments measuring the photon statistics of the cavity output field have demonstrated nonclassical correlation functions of the output light [143], with similar work pushing from this limit to the inherently strong-coupling regime [144–146].

Another instance of intracavity nonlinear optics is the use of optical cavities to study atomic samples exhibiting electromagnetically induced transparency (EIT). In an EIT system, three or more atomic levels are used to create a configuration in which a powerful ''coupling'' beam on one transition prepares the atomic sample and thus strongly influences the index of refraction for a weak probe beam on a second transition [147,148]. In EIT one can obtain various interesting effects, such as: large Kerr nonlinearity, very sharp features in the index as a function of probe frequency, slow or stopped light, and nonlinear behavior at low light intensities. Placing the EIT medium inside an optical cavity, where the ''probe'' beam is a resonant mode of the cavity, enhances these EIT effects so that they can be more easily measured by means of resonant cavity transmission [149]. For example, if EIT is present while scanning the cavity length across the probe resonance, the Kerr nonlinearity induces asymmetry in the cavity line shape; this asymmetry can be used as a sensitive measurement of the intensity-dependent index of refraction [150]. Other observations in this setting include cavity linewidth narrowing related to the slow-light effect [151] as well as several realizations of all-optical switching where the probe transmission is gated by the coupling beam amplitude or detuning [39]. While these observations take place in a weakly coupled regime, other cavity QED effects have also been pointed out for EIT in combination with strong coupling [152].

C. Interacting Single Quanta: The 1-D Atom

By increasing cavity finesse and decreasing mode volume, we move from a semiclassical regime to a regime of small critical parameters $(N_0, m_0) < 1$. Here single atoms and photons induce nonlinear effects in the system response. However, this condition is still consistent with overall dissipative dynamics if the cavity decay rate is fast relative to the coherent coupling g_0. This regime, known as the ''bad cavity'' limit, is realized for $\kappa > g_0^2/\kappa > \gamma_\perp$. In this limit single quanta within the cavity mode interact strongly with one another, but coherence and information leak rapidly from the system into

the output channel defined by cavity decay. Thus the atom-cavity coupling is essentially perturbative, and the atom and cavity each retain their distinct identities but with decay rates modified by the interaction. For instance, an atomic excitation, rather than decaying via spontaneous emission at rate $\gamma_\perp$, is much more likely to be exchanged into the cavity field and subsequently decay via the cavity; this preferential decay via the cavity mode at rate g_0^2/κ gives an effectively "1-D atom."

Experiments in this parameter regime include the quantum phase gate [153] and the use of squeezed light in cavity QED [154]. Both of these effects involve the production of nonclassical effects on the light field due to nonlinearities mediated by a "1-D atom" effect [53]. Thus single photons can interact with one another by means of their common coupling to an intracavity atom. These effects are seen with single strongly coupled atoms; since these experiments delivered atoms to the cavity via thermal beams of atoms transiting a cavity mode, a background of weakly coupled or "spectator" atoms acted to dilute the inherent single-atom effect.

D. Cavity QED: Single Atom Detection, Trapping, and Quantum Aspect of Detection

By further increasing mirror finesse, we decrease κ relative to g_0 and arrive at the regime of strong coupling for the atom-cavity system. In this regime, where $g_0 \gg (\kappa, \gamma_\perp)$, single quanta are significant and, furthermore, their coherent interaction dominates other rates in the system. It is in this limit that observations most closely reflect the ideal structure of the Jaynes-Cummings ladder. Exchange of excitation at rate g_0 is no longer perturbative, and the system crosses over to a set of joint atom-cavity eigenstates with widths set by decay rates κ and $\gamma_\perp$. The coupled atom-cavity transmission spectrum reflects this eigenvalue structure via the vacuum Rabi splitting [155], in which the empty-cavity Lorentzian line profile is transformed into a double-peaked transmission function as shown in Fig. 20 and first directly observed in [156]. The positions and widths of the vacuum Rabi sidebands depend on the strength of the driving field E as well as the parameters $(g(\vec{r}), \kappa, \gamma_\perp)$, and are found via steady-state numerical solution of the master equation.

To fully realize the quantum mechanical phenomena inherent in Eq. (26) for strong coupling, yet another rate must be made small relative to the coherent coupling. This is the rate for decoherence as information exits the system via movement of the individual atoms contributing to the effective atom number N. If excitation is distributed among an ensemble of atoms, each poorly coupled or coupled for a short time as it flies across the cavity

[21.7.2003–8:32pm] [1–84] [Page No. 66] FIRST PROOFS {Books}4101-Bederson/Pageproofs/3d/4101-Bederson-001.3d (Bederson) Paper: 4101-Bederson-001 Keyword

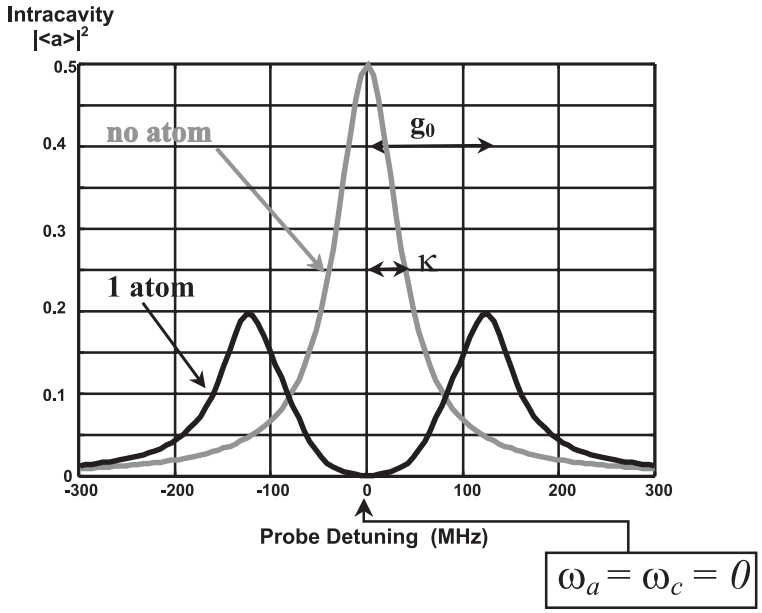

FIG. 20. Vacuum Rabi splitting for the atom-cavity system of [158]. Intracavity $|\langle a\rangle|^2$, proportional to transmission as measured by balanced heterodyne detection, is shown as a function of probe detuning for a fixed probe intensity incident on the cavity. The gray trace shows the Lorentzian line profile of the empty cavity, while the black trace shows the system's spectrum when an atom is strongly coupled to the field, creating a Jaynes-Cummings structure as in Figure 18.

mode, the true structure of the single-atom Jaynes-Cummings ladder cannot be observed. Thus experiments designed to probe the strong coupling regime must be carried out with cold atoms, in a situation where atom number $N \sim 1$ is realized through an actual single atom strongly coupled for a time T satisfying $1/T \ll g_0$. Experiments of this type to date have involved a cloud of atoms trapped in a magneto-optical trap (MOT), cooled via standard sub-Doppler techniques, and then dropped or launched so that single atoms arrive in the cavity mode volume with small velocities and interact one-at-a-time with the cavity field. Such an experiment is shown schematically in Fig. 21; single atoms fall through the cavity mode and are detected via real-time changes in the transmission of a continuously monitored cavity probe beam [11,157–160]. More recently, single atoms have also been caught within the cavity by means of the quantized field [36,37] or trapped there using a separate far-off-resonance trap (FORT) [38,161]. Other efforts in progress include the use of cavities with magnetic traps for atoms [13],

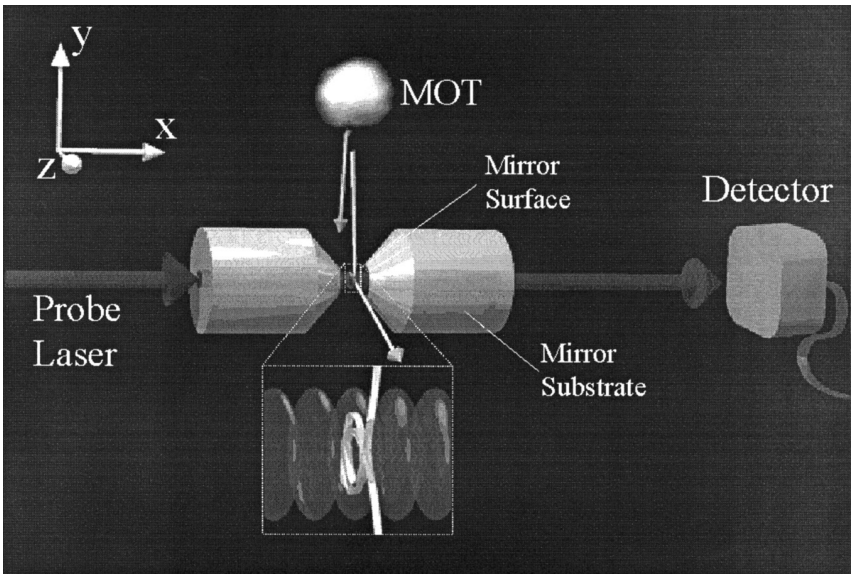

FIG. 21. Experimental schematic for use of cold atoms in cavity QED [36]. A cloud of atoms is collected in a magneto-optical trap (MOT) directly above the cavity mirrors, cooled to a few microkelvin, and released to fall over the cavity. Geometry cuts off the flux of atoms to the actual cavity mode volume so that single atoms arrive one-at-a-time to traverse the cavity field. As an atom moves through the mode volume, a probe beam is continuously applied and its transmission through the cavity monitored in real time.

trapped and cooled ions [162,163], and FORTs chaining atoms through the cavity in the transverse direction [164,165].

Cavity QED with cold atoms in the strong coupling regime has enabled observation of the vacuum Rabi splitting for single atoms in an optical cavity, and of the quantum saturation of the atom-cavity response. In the work of Ref. [158], for example, measurements of cavity transmission vs. input driving field strength clearly deviate from the prediction of the optical bistability equation and are instead consistent with numerical solutions of the quantum master equation itself (Fig. 19, solid line and experimental data points). This work was carried out with laser-cooled Cesium atoms dropped through an optical cavity of length $d = 10.1\,\mu\text{m}$ and mirror finesse $F = 180{,}000$, leading to $(g_0, \kappa, \gamma_\perp) = 2\pi(120, 40, 2.6)$ MHz and critical parameters $(N_0, m_0) = (0.014, 2 \times 10^{-4})$. This and subsequent experiments [36–38,166] thus operate in a regime of critical atom number and saturation photon number orders of magnitude below unity. In this case driving fields which populate the cavity mode with coherent amplitudes at or even below

one photon are sufficient to induce nonlinear response in the system. Likewise, effective atom numbers well below one interact strongly with the cavity field and alter the cavity transmission spectrum. Therefore the presence of a single atom, even when poorly coupled or just entering the cavity mode volume, can be detected with high S/N via the transmission of a probe beam through the cavity.

A striking demonstration of strong coupling in optical cavity QED comes in recent experiments which actually bind an atom in the cavity by creating the "bound state" $|-\rangle$ of the Jaynes-Cummings ladder [36,37]. Figure 22(a)

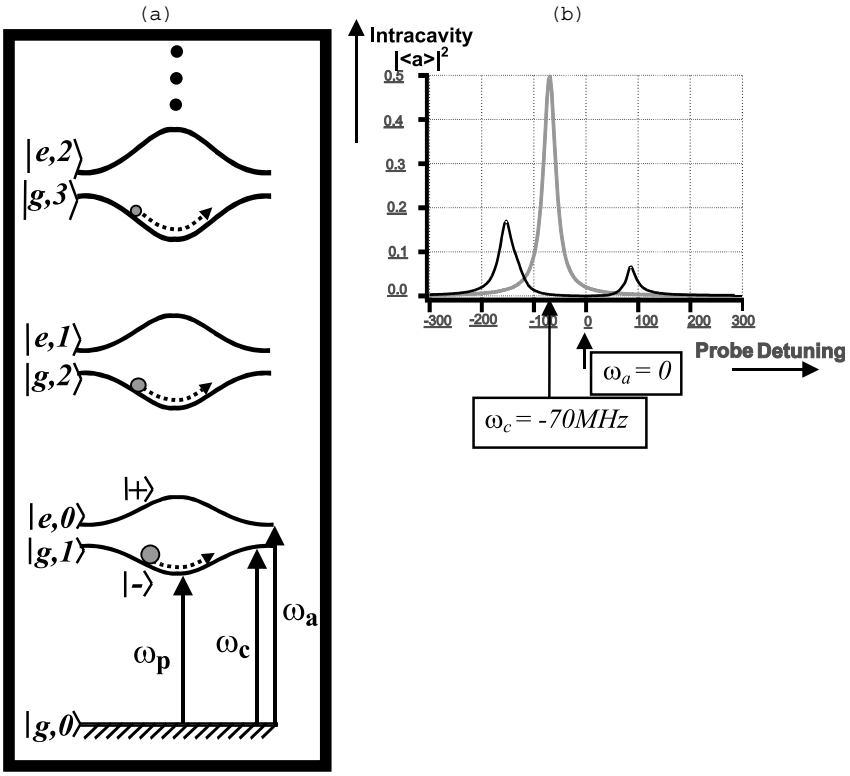

FIG. 22. Jaynes-Cummings ladder and vacuum Rabi splitting to enable trapping of single atoms with the quantized field. (a) This ladder reflects the continuous evolution of energy eigenvalues as an atom moves from outside the cavity (no coupling) to the center and back out again. A driving field at $\omega_p < \omega_c < \omega_a$ populates strong-field-seeking states, leading to an attractive effective potential for the atom in the cavity. (b) Vacuum Rabi spectrum corresponding to (a) for the atom-cavity system of [36]. Note the asymmetry in the spectrum arising from the atom-cavity detuning in this case. A probe beam tuned to the lower Rabi sideband will see a rise in transmission when an atom is coupled to the cavity mode.

shows the ladder of atom-cavity energy eigenvalues with emphasis on the continuous evolution from bare to joint eigenstates as an atom moves from regions of low coupling to regions where the cavity field is strong. Concentrating on the ground and first excited states of the manifold, we will see that this eigenvalue structure enables both sensing and trapping of an atom by means of the cavity field.

If the cavity is probed at its bare resonance frequency $\omega_p \approx \omega_c$, this probe will be moved out of resonance as the atom-cavity coupling increases, causing a drop in transmitted light as an atom moves into the cavity. If, on the other hand, the probe is tuned below the cavity resonance $\omega_p < \omega_c$ and instead near the lower dressed state, it will move into resonance as an atom becomes more strongly coupled. In this case the cavity transmission is originally low and increases as an atom moves toward regions of strong coupling. To see these effects quantitatively, we find steady-state solutions of the master equation to obtain the vacuum Rabi spectrum in Fig. 22(b). As seen already in the data of [158], resonant probe transmission can be reduced by factors of 10^2–10^3, providing enormous S/N for detection of an intracavity atom. For a probe on the lower vacuum Rabi sideband, the transmission increase is less drastic, but probing at this frequency is nevertheless often preferable because of its effect on the atomic motion.

Thus far we have discussed strong coupling between the cavity field and atomic dipole, or internal state. We can define a further condition of strong coupling for the *external* atomic degrees of freedom, which occurs when the coherent coupling dominates the atomic kinetic energy as well. Under these circumstances the position-dependent energy eigenvalues cause an important mechanical effect on an atom interacting with the cavity mode. For instance, an attractive effective potential is felt by an atom when a probe field tuned to the lower vacuum Rabi sideband is used to populate the strong-field-seeking state $|-\rangle$. When this potential is large relative to the atomic kinetic energy, experimental observations range from atom-cavity scattering effects to largely conservative binding of an atom by a single-photon cavity field [36,37,158,167].

In the work of Refs. [36,167], the sensing and trapping aspects of strong coupling are exploited to realize atom–photon binding within an optical cavity. A deep ($\sim$2.5 mK) potential associated with the single-quantum interaction arises from the use of a short cavity with very small mode volume ($d = 10.9\,\mu\text{m}$, $w_0 = 14.1\,\mu\text{m}$). This cavity, with mirror finesse $F = 480{,}000$ and $(g_0, \kappa, \gamma_\perp)/2\pi = (110, 14.2, 2.6)$ MHz, gives critical photon and atom numbers $m_0 = 2.7 \times 10^{-4}$, $N_0 = 6 \times 10^{-3}$. The coherent interaction energy exceeds other relevant energies in the problem, in particular the atomic kinetic energy $E_k \sim k_B(0.5\,\text{mK})$ acquired in the 3-mm fall from the MOT to the cavity mode. Thus an atom can be caught within the cavity if

the system can be driven from its ground state to the trapping state when the atom is at a maximum of the cavity field [168–171].

To implement this triggering strategy, atoms are dropped through the cavity mode while cavity transmission is monitored with a weak probe beam of frequency $\omega_p < \omega_c < \omega_a$ and 0.05 intracavity photons. Such a weak probe tuned near the lower vacuum Rabi sideband allows high S/N for observation of an atom entering the cavity mode, but does not significantly populate the excited states of the atom-cavity system. Once the probe transmission rises above a predetermined threshold, indicating that an atom is in a region of strong coupling to the cavity mode, the probe power is increased to a level of about 0.3 intracavity photons to create a confining potential around the atom.

The resulting cavity transmission for an atom trapped in this way is shown in Fig. 23. It exhibits oscillations between the increased probe level of 0.3 intracavity photons and values as high as $|\langle\hat{a}\rangle|^2\tilde{1}$ due to the atom's motion within the cavity field. Regular oscillations in transmission arise from atomic motion toward and away from the cavity axis, with the level falling back to 0.3 photons when the atom eventually heats out of the trap and escapes from the cavity. Using this protocol, mean atom dwell times in

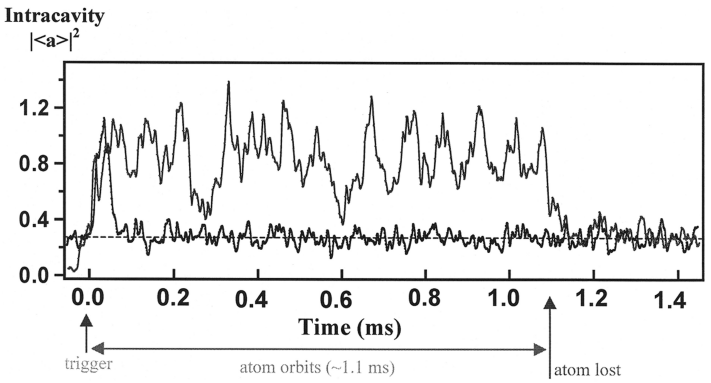

FIG. 23. Single atoms trapped in orbit with single photons using cavity QED [36]. The main trace shows probe light transmission through the cavity as a single atom is trapped there. The probe field, tuned to the lower vacuum Rabi sideband, is initially set to a weak "sensing" level that does not significantly populate excited states of the system. A rise in probe transmission signals an atom falling through the center of the cavity mode, triggering a switch to a stronger "driving" light level. The light now drives the system to strong-field-seeking states and the atom orbits within the cavity, leading to regular oscillations in cavity transmission as shown. The overlaid trace shows an atom transit signal for constant driving field (no triggered trapping) for comparison. For this data, $\omega_p = \omega_a - 2\pi$ (125 MHz) and $\omega_c = \omega_a - 4\pi$ (47 MHz). The transmission signal, detected via balanced heterodyne, is proportional to intracavity $|\langle a\rangle|^2$ and is shown in those units.

the cavity of 340 μs are observed, with some rare events lasting up to several milliseconds. For comparison, the overlaid trace shows a typical transmission signal for an atom falling through the cavity mode with constant input field; this no-triggering case shows a ~75 μs free-fall time for an atom to traverse the cavity mode. Triggered-trapping lifetimes are limited by heating associated with the many decays and re-excitations the atom-cavity system experiences during a single atomic dwell time. It is important to note that, while atoms are trapped via their dipole interaction with a red-detuned light field in a manner reminiscent of the more familiar free-space situation, the dynamics associated with the atom-cavity system are quantitatively and qualitatively different from that case [167]. In particular, a free-space potential of equal intensity would exhibit much greater diffusive heating and thus would largely fail to trap the atoms seen in this experiment; furthermore, the single-atom sensing which enables the trapping strategy is only available through the use of the cavity QED system.

The most interesting feature of the measurement record for a trapped atom is undoubtedly the oscillation in transmission. The period and amplitude of these oscillations agrees quantitatively with atomic orbital motion in the Gaussian mode transverse to the cavity axis. For the parameters of [36] trapped atoms are tightly confined close to a single antinode of the field and detectable signatures from axial motion are not observed [36,167], leading to bounds on the size of any small-amplitude axial excursion. Thus transmission provides a direct, real-time record of an atom's radial distance from the cavity axis; this record can also be used along with the known effective potential to reconstruct two-dimensional trajectories. Such reconstructions, as tested by applying the method to simulated atomic trajectories, represent an atomic position measurement which is about a factor of 5 above the standard quantum limit (SQL) [36,172].

Current experimental efforts focus on use of this real-time position information to feed back to actively control atomic positions within the cavity mode [173]. Progress in this direction aims to use cavity QED to investigate fundamental questions of quantum measurement and optimal state estimation and control. The ability to trap an atom with a single photon field is a dramatic illustration of single-quantum physics in optical cavities; however, it is the sensing power and S/N for real-time observation of the system that make the optical cavity unique.

E. Broader Application of Real-Time Sensing Capabilities: Quantum State Preparation and Detection

Optical cavity QED in the strong coupling regime provides, as we have seen, a nearly-closed environment for interactions between single quanta.

Furthermore, it retains the chief merit of optical cavity spectroscopy in the classical regime: enhanced S/N for observation of intracavity dynamics through the well-defined output channel of cavity decay. While in the language of open quantum systems the cavity decay at rate κ introduces decoherence into the system, the decay is a single output mode that can be directed toward some use that actually keeps information within the system of interest. In the context of optimal state estimation and control, this may mean measuring the transmitted field and using that information to control the system via active feedback. Alternatively, for quantum logic and communication, it may mean measuring the output field to obtain the result of a computation or sending it efficiently to a distant cavity where it will coherently interact with a second atom.

One measure of the capability for observation is the so-called "optical information" rate for monitoring intracavity dynamics through measurement of transmitted light. For a simple estimate of optical information, we consider the case of a resonant probe, $\omega_p = \omega_c = \omega_a$, whose transmission drops as an atom enters the cavity mode. The presence of an atom is thus signaled by a rate dI/dt of "missing" photons at the cavity output. This rate is given by $dI/dt = \kappa(|\langle\hat{a}\rangle|^2_{\text{empty}} - |\langle\hat{a}\rangle|^2_{\text{full}}) \approx \kappa|\langle\hat{a}\rangle|^2_{\text{empty}}$ provided that $|\langle\hat{a}\rangle|^2_{\text{full}}$ is very small. This is the case for strong coupling conditions but driving strength still small enough to prevent complete saturation of the atomic response. Thus dI/dt is maximized for $|\langle\hat{a}\rangle|^2_{\text{full}} \approx m_0$ and $|\langle\hat{a}\rangle|^2_{\text{empty}} \approx C_1^2|\langle\hat{a}\rangle|^2_{\text{full}} \approx g_0^2/\kappa^2$. This rough argument yields an optical information rate $dI/dt = g_0^2/\kappa$; the same quantity appears in a formal treatment of the resonant-probing case as well as in calculations of probing on the lower vacuum Rabi sideband and in analytic expressions for various schemes to monitor both atomic position and atom-cavity internal states in a strong-driving limit [174].

The quantity $dI/dt = g_0^2/\kappa$ corresponds to information about some aspect of the atom-cavity state accessible at a rate of over 10^9 per second for the current generation of strong-coupling Fabry-Perot cavities with alkali atoms. This must be compared with a rate for monitoring the same atom via light scattering in free space, where fluorescence rates do not exceed $\sim 10^7$ per second and it is nearly impossible to imagine effective collection of the light emitted over 4π solid angle. The orders-of-magnitude increase in detection capability represents one of the main strengths of cavity QED in quantum state control.

The cavity-enabled sensing ability can be brought to bear in diverse ways. In a current experiment [38,161], an atom entering the cavity mode is detected via a cavity QED probe field and then trapped by a separate light field in a different longitudinal mode of the cavity. This far-off-resonant trap (FORT) takes advantage of the cavity buildup power to obtain

[21.7.2003–8:32pm] [1–84] [Page No. 73] FIRST PROOFS {Books}4101-Bederson/Pageproofs/3d/4101-Bederson-001.3d (Bederson) Paper: 4101-Bederson-001 Keyword

intensities large enough to trap the atom even in the face of mechanical effects caused by the probe field. Furthermore, the sensing power provided by that probe field allows trapping of one and only one atom in the FORT, offering opportunities for schemes in quantum information science that rely on deterministic interaction of a single atom with the field.

Many such schemes fall under the general heading of quantum state synthesis, using the single-atom medium to prepare single photons and other nonclassical states of the light field. Existing methods of single-photon generation encounter difficulty in providing true determinism of the output field, either in timing or in spatial output channel. The output channel difficulty is naturally solved in cavity QED, and efficient single-atom trapping is bringing true on-demand state generation within the realm of possibility. Proposals encompass not only single photon generation but also numerous other state preparations, such as the photon turnstile and the single atom laser [175], as well as schemes for entanglement generation made possible by the high detection efficiency.

Another direction which relies on real-time sensing in cavity QED is quantum state estimation and quantum feedback. Real-time active feedback methods infer the system state and steer it toward some target value; as cavity-assisted state measurement approaches its fundamental quantum limit, a servo will be limited by measurement back-action effects. Performance of such a control loop will depend on minimal-disturbance measurements for the variable of interest, and the dynamics will exhibit the evolution-and-collapse patterns characteristic of quantum trajectory theory [176,177]. Experiments on real-time feedback to atomic position explore this issue from one direction, but the concept applies equally to other aspects of the overall atom-cavity state. For instance, ongoing experiments [178] also apply real-time sensing and feedback toward the goal of designing novel states of the cavity output field itself.

F. Quantum Logic and Communication Protocols

Cavity QED in the strong coupling regime offers the possibility for efficient measurement and control of single quanta, as we have seen, and for rapid and controlled coherent interactions between these single quanta. In the language of quantum information theory, cavity QED is one of several viable platforms for quantum logic and quantum communication. Ongoing technical progress brings the field closer to achieving atomic position control that is fine enough and stable enough to perform a series of atom-field logic gates at high fidelity; position control is required for this purpose because it means a precise knowledge of the coherent coupling rate $g(\vec{r})$. This

ability in turn will allow for on-demand atom-cavity interactions to prepare and coherently couple novel quantum states of the atom and field.

For purposes of quantum information science, optical cavity QED has the advantage of offering clock rates that are fast in absolute terms, with current experiments in the range $g_0/2\pi \approx 100$–200 MHz. Its chief strength, however, may lie in the marriage of atomic internal states, easily accessible for preparation and robust enough for storage, with states of the light field which can be easily and rapidly transported across large distances. In other words, optical cavity QED provides an attractive setting for the implementation of diverse protocols in quantum communication, quantum teleportation and entanglement distribution, and thus eventually extended quantum networking.

Quantum communication schemes in optical cavity QED generally involve information (e.g., coherence or entanglement) written onto the internal state of an atomic sample. The cavity QED interaction transfers that coherence onto the state of the cavity field, which then exits the cavity via the decay κ in a well-defined mode and can be sent to the receiving station. Here the light may be injected into a second cavity and thus its state can be written onto a "target" atom. Numerous detailed proposals have been developed, with attention to realistic conditions for reversibility and to technical challenges such as atomic localization for high gate fidelity [179]. A closely related variant is the use of similar protocols for teleportation of atomic (motional) states via light fields [180].

For these schemes as well as for quantum state synthesis protocols, our previous schematic is typically altered in two important ways. First, to store information and particularly coherence in the atom, some internal structure beyond the two-level atom is helpful. A useful internal state configuration is the lambda system, which consists of two ground states interacting with a single electronic excited state. The transitions may be distinguished by frequency (e.g., due to hyperfine splitting between the ground states) or by polarization, so that the cavity mode interacts selectively with one ground state and not the second. In such a scheme classical light pulses on the second leg of the lambda system can also be used to "gate" a cavity QED interaction and control the dynamics in detail.

The second technical modification is the use of "one-sided" cavities to replace the symmetric ones we have discussed so far. This change is driven by the desire for a truly unique, coherent output mode for the cavity. We envision a cavity with single-mirror transmissions (T_1, T_2) and losses (A_1, A_2). The current generation of cavities have $(T_1 = T_2) > (A_1 = A_2)$, allowing cavity decay to send light out both cavity mirrors equally. A better situation for quantum communication and nonclassical light generation would instead be $T_1 \gg (T_2, A_1, A_2)$. To achieve this situation while remaining

[21.7.2003–8:32pm] [1–84] [Page No. 75] FIRST PROOFS {Books}4101-Bederson/Pageproofs/3d/4101-Bederson-001.3d (Bederson) Paper: 4101-Bederson-001 Keyword

in the strong coupling regime, mirrors with very low transmission and losses are necessary, since one typically desires even T_1 about 10 ppm or smaller.

G. Future Outlook for Cavity QED

The rich interplay between optical cavity technology and fundamental questions of cavity QED promises to continue for some time. One area of emerging research is cavity-assisted cooling of atoms or molecules, with a number of theoretical schemes just beginning to be realized in experiment [181–184]. Some cooling mechanisms rely explicitly on active feedback or on strong coupling, but others can be thought of as free-space cooling mechanisms adapted to operate in an optical cavity. Since cooling rates and temperatures depend on decay rates in the system, the introduction of new rates through cavity QED and the modification of bare atomic decay rates can offer substantial gains under some circumstances. As colder atoms interact in cavity QED, we also approach a situation where the quantization of atomic external degrees of freedom is important, leading to the regime of the ''well-dressed'' atom and novel effects associated with quantized center-of-mass motion [170,185–189]. As the sensing and cooling effects in cavity QED are better understood, another prospect is the identification of ways in which they can be exploited in dispersive settings rather than in the special case of a single near-resonant transition. Such developments would open up these techniques of trapping, cooling, and real-time microscopy for application to more general atomic and molecular systems.

Cavities for these future developments may come in some unfamiliar guises. Fabry-Perot technology is inherently limited in the mode volume and thus coupling strengths it can offer; in particular, conventional high-reflection coating stacks become ''soft'' boundaries for very short cavities as a larger and larger fraction of the cavity mode actually resides in the coating layers themselves [14]. Numerous other cavity designs are being developed as options. Fairly extensive work, both theoretical and experimental, has been devoted to whispering gallery modes of microspheres [190]; one of the main challenges here is coupling light in and out of the mode without excessive degradation in Q. Another emerging field is the design of optical cavities using photonic bandgap structures in solids, where cavity properties can be selected by tuning the lattice and defect structures [191–193].

VIII. Concluding Remarks on Cavity Enhancement

Dramatic progress has been achieved in optical detection sensitivity by joining laser spectroscopy with resonator physics. The methods discussed in

[21.7.2003–8:32pm] [1–84] [Page No. 76] FIRST PROOFS {Books}4101-Bederson/Pageproofs/3d/4101-Bederson-001.3d (Bederson) Paper: 4101-Bederson-001 Keyword

this article emphasize the importance of separating the atomic signal from the cavity's stored field, and the advantage of detecting signals where only fundamental physical processes introduce noise. We note the importance of determining the cavity's response simultaneously for the on-resonance and off-resonance cases, so that these quantities can be compared from the measured signal to reveal the atomic/molecular absorption of interest. We have discussed how the FM method of NICE-OHMS can be used to implement this signal isolation and subtraction in real time. A repetitive transient heterodyne detection scheme, with lowered technical requirements on the laser system, that meets these design principles has also been discussed. One exciting application of the spectroscopic method discussed in the article is high-resolution, vibration overtone spectroscopy. Coupling this method with large, intracavity beam modes and slow moving molecules [194–196], we expect hyperfine structures and recoil splittings will be measured in overtone transitions in the near future. The precision with which these transitions can be measured will be facilitated with the recently developed femtosecond-comb-referenced laser sources [197,198]. Detailed and precise studies of systematic variations in the overtone spectra can now be carried out in a vast extension of spectral coverage. Extension of these cavity-based sensitive laser spectroscopic approaches is destined to have a strong impact to certain active research areas in condensed matter physics where detailed information of system dynamics and structures are being vigorously pursued.

Besides this significant application of optical cavities for ultrasensitive spectroscopy, the technologies of high finesse and large bandwidth mirror coating will continue to play major and fascinating roles in optical frequency metrology and precision tests. The art of producing ultra-narrow and stable cavity interference fringes and the capability of accurately splitting these fringes to a fraction of parts per million will be critical to a vast array of laser-based modern precision experiments, some of which are mentioned in Section I.D. The emerging synergy between ultrafast lasers and optical cavities will not only present a wonderful opportunity for the extension of sensitive laser spectroscopy to wide spectral coverage, but also offer the prospect of enhanced nonlinear interactions when ultrafast pulses are optimally introduced to interact with an intracavity medium. The continued pursuit of coherent-evolution-dominated open quantum systems will also push the technological envelope of optical cavities and the related science. We hope that our brief account of optical cavities and the related subsequent discussions have helped to thread together a seemingly disparate set of actively pursued research topics ranging from ultrasensitive to ultrafast, and from ultraprecision to ultraquantum.

[21.7.2003–8:32pm] [1–84] [Page No. 77] FIRST PROOFS {Books}4101-Bederson/Pageproofs/3d/4101-Bederson-001.3d (Bederson) Paper: 4101-Bederson-001 Keyword

IX. Acknowledgements

We wish to express our most sincere appreciations to our colleagues J. L. Hall, H. J. Kimble, R. J. Jones, L.-S. Ma, C. J. Hood, and D. Vernooy for their decisive contributions to the work reported here. We also thank H. J. Kimble, K. Birnbaum, T. Northup, R. J. Jones, and M. Notcutt for careful readings of portions of this manuscript. We acknowledge financial support from the National Institute of Standards and Technology, the National Science Foundation, the Army Research Office, the Office of Naval Research, NASA, and the National Research Council. J. Ye is also a staff member at the Quantum Physics Division of the National Institute of Standards and Technology at Boulder. He can be reached by email: Ye@jila.colorado.edu.

X. References

1. Hansch, T.W., Schawlow, A.L., and Toschek, P. (1972). *IEEE J. Quantum Electron.* **QE-8**, 802.
2. Kimble, H.J. (1980). *IEEE J. Quantum Electron.* **16**, 455.
3. Harris, T.D. (1983). In: D.S. Kliger (Ed.), "Ultrasensitive Laser Spectroscopy." p. 343, Academic Press, New York.
4. Kastler, A. (1962). *Appl. Optics* **1**, 17.
5. Cerez, P., Brillet, A., Manpichot, C.N., and Felder, R. (1980). *IEEE Trans. Instrum. Meas.* **29**, 352.
6. Ma, L.S., and Hall, J.L. (1990). *IEEE J. Quantum Electron.* **26**, 2006.
7. Delabachelerie, M., Nakagawa, K., and Ohtsu, M. (1994). *Opt. Lett.* **19**, 840.
8. Anderson, D.Z., Frisch, J.C., and Masser, C.S. (1984). *Appl. Optics* **23**, 1238.
9. Okeefe, A., and Deacon, D.A.G. (1988). *Rev. Sci. Instrum.* **59**, 2544.
10. Hall, J.L., and Borde, C.J. (1976). *Appl. Phys. Lett.* **29**, 788.
11. Mabuchi, H., Ye, J., and Kimble, H.J. (1999). *Appl. Phys. B-Lasers Opt.* **68**, 1095.
12. Hinds, E.A. (1990). *Adv. At. Mol. Opt. Phys.* **28**, 237.
13. Mabuchi, H., and Doherty, A.C. (2002). *Science* **298**, 1372.
14. Hood, C.J., Kimble, H.J., and Ye, J. (2001). *Phys. Rev. A* **64**, 033804.
15. An, K.W., Yang, C.H., Dasari, E.E., and Feld, M.S. (1995). *Opt. Lett.* **20**, 1068.
16. Sappey, A.D., Hill, E.S., Settersten, T., and Linne, M.A. (1998). *Opt. Lett.* **23**, 954.
17. Steinfeld, J.I. (1999). *Chin. J. Chem.* **17**, 204.
18. Paul, B., Scherer, J.J., Okeefe, A., and Saykally, R.J. (1997). *Laser Focus World* **33**, 71.
19. Romanini, D., and Lehmann, K.K. (1993). *Journal of Chemical Physics* **99**, 6287.
20. Scherer, J.J., Voelkel, D., and Rakestraw, D.J. (1997). *Appl. Phys. B-Lasers Opt.* **64**, 699.
21. Spaanjaars, J.J.L., terMeulen, J.J., and Meijer, G. (1997). *Journal of Chemical Physics* **107**, 2242.
22. Park, J., Chakraborty, D., Bhusari, D.M., and Lin, M.C. (1999). *J. Phys. Chem. A* **103**, 4002.
23. Pushkarsky, M.B., Zalyubovsky, S.J., and Miller, T.A. (2000). *Journal of Chemical Physics* **112**, 10695.

24. Modugno, G., Inguscio, M., and Tino, G.M. (1998). *Phys. Rev. Lett.* **81**, 4790.
25. Mazzotti, D., Cancio, P., Giusfredi, G., Inguscio, M., and De Natale, P. (2001). *Phys. Rev. Lett.* **86**, 1919.
26. Gianfrani, L., Fox, R.W., and Hollberg, L. (1999). *J. Opt. Soc. Am. B-Opt. Phys.* **16**, 2247.
27. Abramovici, A., Althouse, W.E., Drever, R.W.P., Gursel, Y., Kawamura, S., Raab, F.J., Shoemaker, D., Sievers, L., Spero, R.E., Thorne, K.S., Vogt, R.E., Weiss, R., Whitcomb, S.E., and Zucker, M.E. (1992). *Science* **256**, 325.
28. Fritschel, P., Gonzalez, G., Lantz, B., Saha, P., and Zucker, M. (1998). *Phys. Rev. Lett.* **80**, 3181.
29. Cohadon, P.F., Heidmann, A., and Pinard, M. (1999). *Phys. Rev. Lett.* **83**, 3174.
30. Semertzidis, Y., Cameron, R., Cantatore, G., Melissinos, A.C., Rogers, J., Halama, H., Prodell, A., Nezrick, F., Rizzo, C., and Zavattini, E. (1990). *Phys. Rev. Lett.* **64**, 2988.
31. Cameron, R., Cantatore, G., Melissinos, A.C., Ruoso, G., Semertzidis, Y., Halama, H.J., Lazarus, D.M., Prodell, A.G., Nezrick, F., Rizzo, C., and Zavattini, E. (1993). *Phys. Rev. D* **47**, 3707.
32. Delabachelerie, M., Nakagawa, K., Awaji, Y., and Ohtsu, M. (1995). *Opt. Lett.* **20**, 572.
33. Nakagawa, K., deLabachelerie, M., Awaji, Y., and Kourogi, M. (1996). *J. Opt. Soc. Am. B-Opt. Phys.* **13**, 2708.
34. Ye, J., Ma, L.S., and Hall, J.L. (1997). *IEEE Trans. Instrum. Meas.* **46**, 178.
35. Vuletic, V., and Chu, S. (2000). *Phys. Rev. Lett.* **84**, 3787.
36. Hood, C.J., Lynn, T.W., Doherty, A.C., Parkins, A.S., and Kimble, H.J. (2000). *Science* **287**, 1447.
37. Pinkse, P.W.H., Fischer, T., Maunz, P., and Rempe, G. (2000). *Nature* **404**, 365.
38. Ye, J., Vernooy, D.W., and Kimble, H.J. (1999). *Phys. Rev. Lett.* **83**, 4987.
39. Wang, H., Goorskey, D., and Xiao, M. (2002). *Phys. Rev. A* **65**, 051802.
40. Bose, S., Jacobs, K., and Knight, P.L. (1999). *Phys. Rev. A* **59**, 3204.
41. Braginsky, V.B., Khalili, F.Y., and Volikov, P.S. (2001). *Phys. Lett. A* **287**, 31.
42. Braginsky, V.B., and Vyatchanin, S.P. (2002). *Phys. Lett. A* **293**, 228.
43. Pipino, A.C.R. (1999). *Phys. Rev. Lett.* **83**, 3093.
44. Dohlman, A.W., Black, H.R., and Royall, J.A. (1993). *Am. Rev. Respir. Dis.* **148**, 955.
45. Olopade, C.O., Zakkar, M., Swedler, W.I., and Rubinstein, I. (1997). *Chest* **111**, 862.
46. Siegman, A.E. (1986). "Lasers." University Science Books, Mill Valley, CA.
47. Wieman, C.E., and Hansch, T.W. (1976). *Phys. Rev. Lett.* **36**, 1170.
48. Jaynes, E.T., and Cummings, F.W. (1963). *Proc. IEEE* **51**, 89.
49. Haroche, S. (1992). In: J. Dalibard, J.-M. Raimond, and J. Zinn-Justin (Eds.), "Fundamental Systems in Quantum Optics, Les Houches Session LIII." North-Holland, Amsterdam.
50. Kimble, H.J. (1994). In: P. Berman (Ed.), "Cavity Quantum Electrodynamics." Academic Press, San Diego.
51. Kimble, H.J. (1998). *Phys. Scr.* **T76**, 127.
52. Lugiato, L.A. (1984). *Progress in Optics* **21**, 69.
53. Turchette, Q.A., Thompson, R.J., and Kimble, H.J. (1995). *Appl. Phys. B-Lasers Opt.* **60**, S1.
54. Wahlquist, H. (1961). *J. Chem. Phys.* **35**, 1708.
55. Smith, R.L. (1971). *J. Opt. Soc. Am.* **61**, 1015.
56. Bjorklund, G.C. (1980). *Opt. Lett.* **5**, 15.
57. Hall, J.L., Hollberg, L., Baer, T., and Robinson, H.G. (1981). *Appl. Phys. Lett.* **39**, 680.
58. Bjorklund, G.C., Levenson, M.D., Lenth, W., and Ortiz, C. (1983). *Applied Physics B-Photophysics and Laser Chemistry* **32**, 145.
59. Ye, J., Ma, L.S., and Hall, J.L. (1996). *Opt. Lett.* **21**, 1000.

[21.7.2003–8:32pm] [1–84] [Page No. 79] FIRST PROOFS {Books}4101-Bederson/Pageproofs/3d/4101-Bederson-001.3d (Bederson) Paper: 4101-Bederson-001 Keyword

60. Ye, J., and Hall, J.L. (2000). *Phys. Rev. A* **61**, 061802.
61. Ye, J., Ma, L.S., and Hall, J.L. (1998). *J. Opt. Soc. Am. B-Opt. Phys.* **15**, 6.
62. Ma, L.S., Ye, J., Dube, P., and Hall, J.L. (1999). *J. Opt. Soc. Am. B-Opt. Phys.* **16**, 2255.
63. Ye, J., Ma, L.S., and Hall, J.L. (2000). *J. Opt. Soc. Am. B-Opt. Phys.* **17**, 927.
64. Ishibashi, C., and Sasada, H. (1999). *Jpn. J. Appl. Phys. Part 1 - Regul. Pap. Short Notes Rev. Pap.* **38**, 920.
65. Ishibashi, C., and Sasada, H. (2000). *J. Mol. Spectrosc.* **200**, 147.
66. Letokhev, V.S., and Chebotayev, V.P. (1977). "Nonlinear Laser Spectroscopy." Springer-Verlag, Berlin.
67. Stenholm, S. (1983). "Foundation of Laser Spectroscopy." Wiley, New York.
68. Ye, J., Robertsson, L., Picard, S., Ma, L.S., and Hall, J.L. (1999). *IEEE Trans. Instrum. Meas.* **48**, 544.
69. Hall, J.L., Ma, L.S., Taubman, M., Tiemann, B., Hong, F.L., Pfister, O., and Ye, J. (1999). *IEEE Trans. Instrum. Meas.* **48**, 583.
70. Werle, P. (1995). *Appl. Phys. B-Lasers Opt.* **60**, 499.
71. Wong, N.C., and Hall, J.L. (1985). *J. Opt. Soc. Am. B-Opt. Phys.* **2**, 1527.
72. Allan, D.W. (1987). *IEEE Trans. Ultrason. Ferroelectr. Freq. Control* **34**, 647.
73. Borde, C.J., Hall, J.L., Kunasz, C.V., and Hummer, D.G. (1976). *Phys. Rev. A* **14**, 236.
74. Bagayev, S.N., Chebotayev, V.P., Dmitriyev, A.K., Om, A.E., Nekrasov, Y.V., and Skvortsov, B.N. (1991). *Applied Physics B-Photophysics and Laser Chemistry* **52**, 63.
75. Chardonnet, C., Guernet, F., Charton, G., and Borde, C.J. (1994). *Appl. Phys. B-Lasers Opt.* **59**, 333.
76. Levenson, M.D., Paldus, B.A., Spence, T.G., Harb, C.C., Harris, J.S., and Zare, R.N. (1998). *Chem. Phys. Lett.* **290**, 335.
77. Drever, R.W.P., Hall, J.L., Kowalski, F.V., Hough, J., Ford, G.M., Munley, A.J., and Ward, H. (1983). *Applied Physics B-Photophysics and Laser Chemistry* **31**, 97.
78. Salomon, C., Hils, D., and Hall, J.L. (1988). *J. Opt. Soc. Am. B-Opt. Phys.* **5**, 1576.
79. Rafac, R.J., Young, B.C., Beall, J.A., Itano, W.M., Wineland, D.J., and Bergquist, J.C. (2000). *Phys. Rev. Lett.* **85**, 2462.
80. Udem, T., Reichert, J., Holzwarth, R., and Hänsch, T.W. (1999). *Phys. Rev. Lett.* **82**, 3568.
81. Cundiff, S.T., and Ye, J. (2003). *Rev. Modern Phys.*, in press.
82. Jones, R.J., and Diels, J.C. (2001). *Phys. Rev. Lett.* **86**, 3288.
83. Rempe, G., Thompson, R.J., Kimble, H.J., and Lalezari, R. (1992). *Opt. Lett.* **17**, 363.
84. Hall, J.L., Ye, J., and Ma, L.S. (2000). *Phys. Rev. A* **62**, 013815.
85. Devoe, R.G., Fabre, C., Jungmann, K., Hoffnagle, J., and Brewer, R.G. (1988). *Phys. Rev. A* **37**, 1802.
86. Jones, R.J., and Ye, J. (2002). *Opt. Lett.* **27**, 1848.
87. Cotton, A., Mouton, H., and Hebd, C.R. (1905). *Seances Acad. Sci.* **141**, 317.
88. Adler, S.L. (1971). *Ann. Phys.* **67**, 599.
89. Raffelt, G., and Stodolsky, L. (1988). *Phys. Rev. D* **37**, 1237.
90. Wood, C.S., Bennett, S.C., Cho, D., Masterson, B.P., Roberts, J.L., Tanner, C.E., and Wieman, C.E. (1997). *Science* **275**, 1759.
91. Chauvat, D., Le Floch, A., Vallet, M., and Bretenaker, F. (1998). *Appl. Phys. Lett.* **73**, 1032.
92. Moriwaki, S., Sakaida, H., Yuzawa, T., and Mio, N. (1997). *Appl. Phys. B-Lasers Opt.* **65**, 347.
93. Brandi, F., DellaValle, F., DeRiva, A.M., Micossi, P., Perrone, F., Rizzo, C., Ruoso, G., and Zavattini, G. (1997). *Appl. Phys. B-Lasers Opt.* **65**, 351.
94. Bakalov, D., Brandi, F., Cantatore, G., Carugno, G., Carusotto, S., Della, F., Valle De, A.M., Riva, Gastaldi, U., Iacopini, E., Micossi, P., Milotti, E., Onofrio, R., Pengo, R.,

[21.7.2003–8:32pm] [1–84] [Page No. 80] FIRST PROOFS {Books}4101-Bederson/Pageproofs/3d/4101-Bederson-001.3d (Bederson) Paper: 4101-Bederson-001 Keyword

Perrone, F., Petrucci, G., Polacco, E., Rizzo, C., Ruoso, G., Zavattini, E., and Zavattini, G. (1998). *Quantum Semiclass. Opt.* **10**, 239.
95. Zhu, M., and Hall, J.L. (1993). *J. Opt. Soc. Am. B-Opt. Phys.* **10**, 802.
96. Lichten, W. (1985). *J. Opt. Soc. Am. A-Opt. Image Sci. Vis.* **2**, 1869.
97. Lichten, W. (1986). *J. Opt. Soc. Am. A-Opt. Image Sci. Vis.* **3**, 909.
98. Devoe, R.G., and Brewer, R.G. (1984). *Phys. Rev. A* **30**, 2827.
99. Devoe, R.G., and Brewer, R.G. (1984). *J. Opt. Soc. Am. A-Opt. Image Sci. Vis.* **1**, 1307.
100. Kourogi, M., Nakagawa, K., and Ohtsu, M. (1993). *IEEE J. Quantum Electron.* **29**, 2693.
101. Brothers, L.R., Lee, D., and Wong, N.C. (1994). *Opt. Lett.* **19**, 245.
102. Imai, K., Zhao, Y., Kourogi, M., Widiyatmoko, B., and Ohtsu, M. (1999). *Opt. Lett.* **24**, 214.
103. Imai, K., Kourogi, M., and Ohtsu, M. (1998). *IEEE J. Quantum Electron.* **34**, 54.
104. Ye, J., Ma, L.S., Day, T., and Hall, J.L. (1997). *Opt. Lett.* **22**, 301.
105. Diddams, S.A., Ma, L.S., Ye, J., and Hall, J.L. (1999). *Opt. Lett.* **24**, 1747.
106. Udem, T., Reichert, J., Hänsch, T.W. and Kourogi, M. (2000). *Phys. Rev. A* **62**, 1801.
107. Udem, T., Reichert, J., Holzwarth, R., and Hänsch, T.W. (1999). *Opt. Lett.* **24**, 881.
108. Kobayashi, T., Sueta, T., Cho, Y., and Matsuo, Y. (1972). *Appl. Phys. Lett.* **21**, 341.
109. Macfarlane, G.M., Bell, A.S., Riis, E., and Ferguson, A.I. (1996). *Opt. Lett.* **21**, 534.
110. Ho, K.P., and Kahn, J.M. (1993). *IEEE Photonics Technol. Lett.* **5**, 721.
111. Brothers, L.R., and Wong, N.C. (1997). *Opt. Lett.* **22**, 1015.
112. Hänsch, T.W. (1976). In A. Mooradain, T. Jaeger, and P. Stokseth, (Eds.), "Tunable Lasers and Applications." Springer-Verlag, Berlin.
113. Baklanov, Y.V., and Chebotayev, V.P. (1977). *Applied Physics* **12**, 97.
114. Teets, R., Eckstein, J., and Hänsch, T.W. (1977). *Phys. Rev. Lett.* **38**, 760.
115. Salour, M.M. (1978). *Rev. Mod. Phys.* **50**, 667.
116. Eckstein, J.N., Ferguson, A.I., and Hänsch, T.W. (1978). *Phys. Rev. Lett.* **40**, 847.
117. Ferguson, A.I., and Taylor, R.A. (1983). *Proceedings of the Society of Photo-Optical Instrumentation Engineers* **369**, 366.
118. Bramwell, S.R., Ferguson, A.I., and Kane, D.M. (1987). *Opt. Lett.* **12**, 666.
119. Wineland, D.J., Bergquist, J.C., Itano, W.M., Diedrich, F., and Weimer, C.S. (1989). In: G.F. Bassani, M. Inguscio, and T.W. Hänsch (Eds.), "The Hydrogen Atom." p. 123, Springer-Verlag, Berlin.
120. Reichert, J., Holzwarth, R., Udem, T., and Hänsch, T.W. (1999). *Opt. Commun.* **172**, 59.
121. Diddams, S.A., Jones, D.J., Ye, J., Cundiff, T., Hall, J.L., Ranka, J.K., Windeler, R.S., Holzwarth, R., Udem, T., and Hansch, T.W. (2000). *Phys. Rev. Lett.* **84**, 5102.
122. Ye, J., Yoon, T.H., Hall, J.L., Madej, A.A., Bernard, J.E., Siemsen, K.J., Marmet, L., Chartier, J.-M., and Chariter, A. (2000). *Phys. Rev. Lett.* **85**, 3797.
123. Negus, D.K., Spinelli, L., Goldblatt, N., and Feugnet, G. (1991). In: "Advanced Solid-State Lasers." Vol. 10, OSA.
124. Spence, D.E., Kean, P.N., and Sibbett, W. (1991). *Opt. Lett.* **16**, 42.
125. Asaki, M.T., Huang, C.P., Garvey, D., Zhou, J.P., Kapteyn, H.C., and Murnane, M.M. (1993). *Opt. Lett.* **18**, 977.
126. Ranka, J.K., Windeler, R.S., and Stentz, A.J. (2000). *Opt. Lett.* **25**, 25.
127. Diels, J.-C., and Rudolph, W. (1996). "Ultrashort Laser Pulse Phenomena: Fundamentals, Techniques, and Applications on a Femtosecond Timescale." Academic Press, San Diego.
128. Telle, H.R., Steinmeyer, G., Dunlop, A.E., Stenger, J., Sutter, D.H., and Keller, U. (1999). *Appl. Phys. B* **69**, 327.
129. Jones, D.J., Diddams, S.A., Ranka, J.K., Stentz, A., Windeler, R.S., Hall, J.L., and Cundiff, S.T. (2000). *Science* **288**, 635.

130. Apolonski, A., Poppe, A., Tempea, G., Spielmann, C., Udem, T., Holzwarth, R., T.W. Hänsch, and Krausz, F. (2000). *Phys. Rev. Lett.* **85**, 740.
131. Jones, R.J., Diels, J.C., Jasapara, J., and Rudolph, W. (2000). *Opt. Commun.* **175**, 409.
132. Brabec, T., and Krausz, F. (2000). *Rev. Mod. Phys.* **72**, 545.
133. Baltuska, A., Fuji, T., and Kobayashi, T. (2002). *Phys. Rev. Lett.* **88**, 133901.
134. Baltuska, A., Udem, T., Uiberacker, M., Hentschel, M., Goulielmakis, E., Gohle, C., Holzwarth, R., Yakoviev, V.S., Scrinzi, A., Hansch, T.W., and Krausz, F. (2003). *Nature* **421**, 611.
135. Heupel, T., Weitz, M., and Hansch, T.W. (1997). *Opt. Lett.* **22**, 1719.
136. Malcolm, G.P.A., Ebrahimzadeh, M., and Ferguson, A.I. (1992). *IEEE J. Quantum Electron.* **28**, 1172.
137. Crosson, E.R., Haar, P., Marcus, G.A., Schwettman, H.A., Paldus, B.A., Spence, T.G., and Zare, R.N. (1999). *Rev. Sci. Instrum.* **70**, 4.
138. Yanovsky, V.P., and Wise, F.W. (1994). *Opt. Lett.* **19**, 1952.
139. McConnell, G., Ferguson, A.I., and Langford, N. (2001). *J. Phys. D-Appl. Phys.* **34**, 2408.
140. Cohen-Tannoudji, C., Dupont-Roc, J., and Grynberg, G. (1992). ''Atom-Photon Interactions.'' Wiley, New York.
141. Grant, D.E., and Kimble, H.J. (1982). *Opt. Lett.* **7**, 353.
142. Weyer, K.G., Wiedenmann, H., Rateike, M., Gillivray, W.R.M., Meystre, P., and Walther, H. (1981). *Opt. Commun.* **37**, 426.
143. Rempe, G., Thompson, R.J., Brecha, R.J., Lee, W.D., and Kimble, H.J. (1991). *Phys. Rev. Lett.* **67**, 1727.
144. Mielke, S.L., Foster, G.T., and Orozco, L.A. (1998). *Phys. Rev. Lett.* **80**, 3948.
145. Foster, G.T., Orozco, L.A., Castro-Beltran, H.M. and Carmichael, H.J. (2000). *Phys. Rev. Lett.* **85**, 3149.
146. Foster, G.T., Mielke, S.L., and Orozco, L.A. (2000). *Phys. Rev. A* **61**, 053821.
147. Arimondo, E. (1996). *Progress in Optics*, **35**(35), 257.
148. Harris, S.E. (1997). *Phys. Today* **50**, 36.
149. Lukin, M.D., Fleischhauer, M., Scully, M.O., and Velichansky, V.L. (1998). *Opt. Lett.* **23**, 295.
150. Wang, H., Goorskey, D., and Xiao, M. (2001). *Phys. Rev. Lett.* **87**, 073601.
151. Wang, H., Goorskey, D.J., Burkett, W.H., and Xiao, M. (2000). *Opt. Lett.* **25**, 1732.
152. Rebic, S., Parkins, A.S., and Tan, S.M. (2002). *Phys. Rev. A* **65**, 063804.
153. Turchette, Q.A., Hood, C.J., Lange, W., Mabuchi, H., and Kimble, H.J. (1995). *Phys. Rev. Lett.* **75**, 4710.
154. Turchette, Q.A., Georgiades, N.P., Hood, C.J., Kimble, H.J., and Parkins, A.S. (1998). *Phys. Rev. A* **58**, 4056.
155. Sanchez-Mondragon, J.J., Narozhny, N.B., and Eberly, J.H. (1984). *J. Opt. Soc. Am. B-Opt. Phys.* **1**, 518.
156. Thompson, R.J., Rempe, G., and Kimble, H.J. (1992). *Phys. Rev. Lett.* **68**, 1132.
157. Mabuchi, H., Turchette, Q.A., Chapman, M.S., and Kimble, H.J. (1996). *Opt. Lett.* **21**, 1393.
158. Hood, C.J., Chapman, M.S., Lynn, T.W., and Kimble, H.J. (1998). *Phys. Rev. Lett.* **80**, 4157.
159. Munstermann, P., Fischer, T., Maunz, P., Pinkse, P.W.H., and Rempe, G. (1999). *Phys. Rev. Lett.* **82**, 3791.
160. Shimizu, Y., Shiokawa, N., Yamamoto, N., Kozuma, M., Kuga, T., Deng, L., and Hagley, E.W. (2002). *Phys. Rev. Lett.* **89**, 233001.
161. McKeever, J., Buck, J.R., Boozer, A.D., Kuzmich, A., Naegerl, H.-C., Stamper-Kurn, D.M., and Kimble, H.J. (2003). *Phys. Rev. Lett.*, in press.

[21.7.2003–8:32pm] [1–84] [Page No. 82] FIRST PROOFS {Books}4101-Bederson/Pageproofs/3d/4101-Bederson-001.3d (Bederson) Paper: 4101-Bederson-001 Keyword

162. Mundt, A.B., Kreuter, A., Becher, C., Leibfried, D., Eschner, J., Schmidt-Kaler, F., and Blatt, R. (2002). *Phys. Rev. Lett.* **89**, 103001.
163. Walther, H. (2002). private communications.
164. Kuhr, S., Alt, W., Schrader, D., Muller, M., Gomer, V., and Meschede, D. (2001). *Science* **293**, 278.
165. Chapman, M. (2002). private communications.
166. Hood, C.J., Lynn, T.W., Doherty, A.C., Vernooy, D.W., Ye, J., and Kimble, H.J. (2001). *Laser Phys.* **11**, 1190.
167. Doherty, A.C., Lynn, T.W., Hood, C.J., and Kimble, H.J. (2001). *Phys. Rev. A* **63**, 013401.
168. Haroche, S., Brune, M., and Raimond, J.M. (1991). *Europhys. Lett.* **14**, 19.
169. Englert, B.G., Schwinger, J., Barut, A.O., and Scully, M.O. (1991). *Europhys. Lett.* **14**, 25.
170. Scully, M.O., Meyer, G.M., and Walther, H. (1996). *Phys. Rev. Lett.* **76**, 4144.
171. Doherty, A.C., Parkins, A.S., Tan, S.M., and Walls, D.F. (1997). *Phys. Rev. A* **56**, 833.
172. Mabuchi, H. (1998). *Phys. Rev. A* **58**, 123.
173. Fischer, T., Maunz, P., Pinkse, P.W.H., Puppe, T., and Rempe, G. (2002). *Phys. Rev. Lett.* **88**, 163002.
174. Soklakov, A., and Schack, R. (2002). quant-ph/0210024.
175. Feld, M.S., and An, K.W. (1998). *Sci. Am.* **279**, 56.
176. Mabuchi, H., and Wiseman, H.M. (1998). *Phys. Rev. Lett.* **81**, 4620.
177. Warszawski, P., Wiseman, H.M., and Mabuchi, H. (2002). *Phys. Rev. A* **65**, 023802.
178. Smith, W.P., Reiner, J.E., Orozco, L.A., Kuhr, S., and Wiseman, H.M. (2002). *Phys. Rev. Lett.* **89**, 133601.
179. Briegel, H.J., Cirac, J.I., Dur, W., van, S.J., Enk, Kimble, H.J., Mabuchi, H., and Zoller, P. (1999). *Quantum Computing and Quantum Communications* **1509**, 373.
180. Parkins, A.S., and Kimble, H.J. (1999). *J. Opt. B-Quantum Semicl. Opt.* **1**, 496.
181. Domokos, P., Horak, P., and Ritsch, H. (2001). *J. Phys. B-At. Mol. Opt. Phys.* **34**, 187.
182. Gangl, M., and Ritsch, H. (2001). *Phys. Rev. A* **64**, 063414.
183. van Enk, S.J., McKeever, J., Kimble, H.J., and Ye, J. (2001). *Phys. Rev. A* **64**, 013407.
184. Chan, H.W., Black, A.T., and Vuletic, V. (2003). quant-ph/0208100.
185. Meystre, P., Schumacher, E., and Stenholm, S. (1989). *Opt. Commun.* **73**, 443.
186. Ren, W., and Carmichael, H.J. (1995). *Phys. Rev. A* **51**, 752.
187. Herkommer, A.M., Carmichael, H.J., and Schleich, W.P. (1996). *Quantum Semiclass. Opt.* **8**, 189.
188. Doherty, A.C., Parkins, A.S., Tan, S.M., and Walls, D.F. (1998). *Phys. Rev. A* **57**, 4804.
189. Vernooy, D.W., and Kimble, H.J. (1997). *Phys. Rev. A* **56**, 4287.
190. Vernooy, D.W., Furusawa, A., Georgiades, N.P., Ilchenko, V.S., and Kimble, H.J. (1998). *Phys. Rev. A* **57**, R2293.
191. Yamamoto, Y., and Slusher, R.E. (1993). *Phys. Today* **46**, 66.
192. Chang, R.K., and Campillo, A.J. (1996). (World Scientific, Singapore.
193. Khitrova, G., Gibbs, H.M., Jahnke, F., Kira, M., and Koch, S.W. (1999). *Rev. Mod. Phys.* **71**, 1591.
194. Bethlem, H.L., Berden, G., Crompvoets, F.M.H., Jongma, R.T., van Roij, A.J.A., and Meijer, G. (2000). *Nature* **406**, 491.
195. Gupta, M., and Herschbach, D. (1999). *J. Phys. Chem. A* **103**, 10670.
196. Doyle, J.M., and Friedrich, B. (1999). *Nature* **401**, 749.
197. Jost, J.D., Hall, J.L., and Ye, J. (2002). *Optics Express* **10**, 515.
198. Foreman, S., Jones, D.J., and Ye, J. (2003). *Opt. Lett.* **28**, 370.

[21.7.2003–8:32pm] [1–84] [Page No. 83] FIRST PROOFS {Books}4101-Bederson/Pageproofs/3d/4101-Bederson-001.3d (Bederson) Paper: 4101-Bederson-001 Keyword